UNIVERSIDAD DE CHILE
FACULTAD DE CIENCIAS FÍSICAS Y MATEMÁTICAS
DEPARTAMENTO DE FÍSICA

EDGE AND TOPOLOGICAL STATES: USING ELECTRICAL CIRCUITS AS QUANTUM SIMULATOR.

TESIS PARA OPTAR AL GRADO DE MAGÍSTER EN CIENCIAS, MENCIÓN FÍSICA.

LUCAS MAURICIO GONZÁLEZ MUÑOZ

PROFESOR GUÍA:
LUIS FOÀ TORRES

MIEMBROS DE LA COMISIÓN:
ÁLVARO NÚÑEZ VÁZQUEZ
ERIC SUÁREZ MORELL

Este trabajo ha sido parcialmente financiado por:
ANID FondeCyT Regular No.1211038 y 1170917.

SANTIAGO DE CHILE
2024

RESUMEN DE LA TESIS PARA OPTAR AL GRADO DE
MAGÍSTER EN CIENCIAS, MENCION FÍSICA
POR: LUCAS MAURICIO GONZÁLEZ MUÑOZ
FECHA: 2024
PROF. GUÍA: LUIS FOÀ TORRES

ESTADOS TOPOLÓGICOS Y DE BORDE: USANDO CIRCUITOS ELÉCTRICOS COMO SIMULADOR CUÁNTICO.

Español

En la búsqueda para mejorar nuestra comprensión sobre sistemas cuánticos, que frecuentemente se ve obstaculizada por la dificultad para acceder directamente a sus propiedades, la imaginación humana ha dado lugar a diferentes "simuladores". Uno de los más recientemente popularizados, se basa en el uso de circuitos eléctricos [1]. En la configuración adecuada, estos circuitos permiten simular modelos de enlace fuerte, ampliamente utilizados en el contexto del estudio de materiales incluyendo los llamados aislantes topológicos, en este contexto, estos circuitos se denominan circuitos topoléctricos. Estos circuitos peculiares abren un abanico de posibilidades para hacer lo que podría resultar imposible en materia condensada, como observar la evolución temporal de un estado en una red, y también otras cosas que si bien son factibles serían de muy alto costo, como por ejemplo acceder de manera directa a la estructura de bandas de un sistema mediante mediciones.

En el Capítulo Uno, proporcionamos contexto sobre los aislantes topológicos, exponiendo los modelos clave y algo de contexto histórico. Este capítulo concluye con una introducción al tema principal de este trabajo: los circuitos topoeléctricos.

El Capítulo Dos introduce la teoría asociada al Laplaciano a tierra, dando la base necesaria para nuestros cálculos y revisa las herramientas disponibles la exploración a lo largo de este estudio.

El Capítulo Tres presenta nuestros resultados, demostrando las capacidades de los circuitos eléctricos para replicar fenómenos topológicos usando el modelo Su-Schrieffer-Heeger (El modelo mas simple para un aislante topológico en una dimensión) y el modelo de Haldane. También revisamos otros modelos tipo enlace fuerte que presentan estados de borde interesantes pero no topológicos como el modelo de Haldane modificado, que da origen a estados antiquirales (Colomes et al., 2018)[2], y la observación de Skin effect dinámico en sistemas no-Hermiticos (Li et al., 2022)[3]. Estos últimos dos resultados son originales de este trabajo. Basados en las mediciones hechas en estos circuits demostramos como es posible acceder a la estructura de bandas, a los elementos de matriz del Hamiltoniano y además la observación de la dinámica de excitaciones.

Finalmente, en el Capítulo Cuatro presentamos las principales conclusiones y perspectivas de este trabajo.

ABSTRACT OF THE THESIS FOR THE DEGREE
OF MASTER OF SCIENCE, MENTION IN PHYSICS
BY: LUCAS MAURICIO GONZÁLEZ MUÑOZ
DATE: 2024
SUPERVISORS: LUIS FOÀ TORRES

EDGE AND TOPOLOGICAL STATES: USING ELECTRICAL CIRCUITS AS QUANTUM SIMULATOR.

English

In the pursuit of improving our understanding of quantum systems, which is often hindered by the difficulty of accessing their properties directly, human imagination has given rise to different "simulators." One of the most recently popularized is based on the use of electrical circuits [1]. In the appropriate configuration, these circuits allow simulating tight-binding models, widely used in the context of the study of materials including the so-called topological insulators, in this context, these circuits are referred to as topolectrical circuits. These peculiar circuits open up a range of possibilities to do what could be impossible in condensed matter such as observing the temporal evolution of a state in a network, and also other things that, while feasible, would be very expensive such as directly accessing the band structure of a system through measurements.

In Chapter One, we provide the context of topological insulators, exposing key models and some historical context. This chapter concludes with an introduction to the main topic of this work: topoelectrical circuits.

Chapter Two introduces grounded Laplacian theory, providing the theoretical foundation necessary for our calculations and the tools available for exploration throughout this study.

The third chapter presents our results from this work, demonstrating the capabilities of electrical circuitry to replicate topological phenomena using the Su-Schrieffer-Heeger model (the simplest model of a topological insulator in one dimension) and the Haldane model. We also present tight-binding systems that present interesting but non-topological edge-states like the modified Haldane model, which gives rise to antichiral states (Colomes et al., 2018)[2], and the observation of dynamic skin effects in non-Hermitian systems (Li et al., 2022)[4]. These last two results are original to this work. Based on measurements in these circuits, we demonstrate how it is possible to access the band structure, the matrix elements of the Hamiltonian itself, and also observe the dynamics of excitations.

Lastly, in chapter 4 we present the main conclusions and perspectives of this work.

A la paciencia, al tiempo y a mi padre,
que su apoyo y confianza son el pilar de mi trabajo...

Agradecimientos

Han sido unos largos años en los cuales he tenido siempre la suerte de rodearme de amigos y buenos colegas. Es por esto que agradezco a todo el que me haya acompañado durante este tiempo, desde risas compartidas, trabajando conmigo o incluso si se tomó el tiempo de asistir a una de mis clases.

Le agradezco a mi profesor guía Luis Foà por la paciencia que siempre me ha tenido, por mostrarme su forma de enfrentar la vida y sus certeros comentarios. Gracias por confiar en mí cuando yo no lo hice y permitirme trabajar contigo.

Más o menos la mitad del tiempo que estuve en el programa lo pasé en casa, la pandemia me permitió pasar mucho más tiempo con toda mi familia, por lo que les quiero agradecer por todo su apoyo en estos años. Mamá, papá, Brunito, Polo, Canela, Gatoton y Conchi, los amo con todo mi corazón.

Agradezcoo a mis amigos por estar conmigo. Primero a Aldo y Rodrigo por estos años soportándome hablar de física y todas esas cosas ñoñas que tanto nos gustan, ojalá sean muchos más. Le agradezco a Ro, mi hermana del alma, quien junto a sus amigos de universidad me acogieron como uno más de los suyos a pesar de ser el bicho raro del grupo. Agradezco también a mis amigos de la U: Barbi y Juanjo por esos años de plan común deambulando por la universidad. Pola, Mau, Robert, Pauli, Peri, Raza, Byron, Nico y Mati, mis amigos de licenciatura con quienes pasé tantas horas matraqueando, descubriendo juntos esta ciencia que tanto nos acercó y de sacarme de mi zona de confort a diario. Por último, a mis amigos del máster: Gaga, Clau, Rojo, Chesta, Guille, Feña, Colipi, Phalo, Nico, Aguayo, Yayo, Nacho y Geruto, quienes me acompañaron cuando estuve más sólo e hicieron de la sala de tesistas un lugar no tan frío y silencioso como alguna vez quedó.

Además quiero agradecerle a todos los profesores que me permitieron ser su ayudante o auxiliar. En particular, al profesor Francisco Brieva, quien por tantos semestres confió en mí para ser su auxiliar. Gracias por todas esas conversaciones extensas en su oficina, por desafiarme cada semana con sus problemas locos y por preocuparse tanto por mí en sus últimos años en la universidad. Atesoro todos los consejos que me dio y todo el trabajo que hicimos juntos. Siempre lo admiraré por su energía al hacer clases y por la dedicación a sus alumnos, aun cuando pasamos por su sala de clases hace ya tantos años.

Agradezco también al Departamento de Física de la universidad Andrés Bello por confiar en mí durante tanto tiempo al darme la oportunidad de hacer docencia en sus aulas. Sin esta experiencia no sería quien soy ahora.

Quiero terminar aclarando que esta tesis es fruto del tiempo y la paciencia. Si bien mucha gente aportó al desarrollo de estas ideas, es cierto también que el tiempo terminó por consolidarlas, junto a la paciencia de seguir adelante. Dicen que los físicos le tememos al tiempo, pero yo creo que hay que confiar en él.

Table of Content

Chapter 1

Introduction

In recent decades, the study of new electronic states at the boundary or edge of a system (typically crystals) has gained enormous interest [5–9]. In particular, the use of topological arguments has proven to be an effective tool in explaining phenomena that previously lacked explanation [10].

One of the early milestones in the physics of topological effects is the integer quantum Hall effect (QHE) [11]. This phenomenon occurs in a two-dimensional confined electron gas under the effect of a strong perpendicular magnetic field, displaying quantized Hall conductivity in integer multiples of e^2/h. The remarkable precision of the Hall conductivity plateaus initially puzzled the scientific community.

Seeking to obtain such states, now in the absence of a magnetic field, Duncan Haldane proposed a model in 1988 to achieve the quantum Hall effect without Landau levels [10]. Haldane suggests a 2D honeycomb lattice and proposes a complex interaction term to second neighbors to replace the role of an external field. While locally, this term is similar to a magnetic field, globally, Haldane arranges its phases so that the total magnetic flux is zero, breaking time-reversal symmetry and consequently opening an energy gap in the band structure. This addition produces two counter-propagating edge states that connect the valence band with the conduction band. This phenomenon initially called the anomalous quantum Hall effect, is characterized by the system's topological invariant (again, the Chern number). This model introduces the concept of a lattice with topological properties, but its experimental realization seemed impossible due to the arbitrariness of the new term that breaks time-reversal symmetry. It was not until 2014 that it was adequately verified using ultra-cold fermions [12].

In 2005, Kane and Mele [13] explored a way to obtain Haldane-type states through a physical interaction. This interaction should primarily preserve time-reversal symmetry, as is the case in most materials. Surprisingly, Kane and Mele found that spin-orbit interaction, present to varying degrees in all materials, could play that role. Today, we know that the Kane and Mele model (for a honeycomb lattice with spin-orbit interaction) consists of two conjugate copies of the Haldane model, one for each spin component, preserving time-reversal symmetry. This system is called the quantum spin Hall insulator and exhibits helical spin-polarized edge states. After a short search and thanks to other theoretical works, this effect is experimentally achieved in 2007 [14]. It was the beginning of the era of so-called topological insulators. With this milestone, the research extends this physics to other materials and systems. Topological phenomena that have achieved experimental realization go beyond the quantum Hall regime, including topological insulators in 1 [15] and 3 [16] dimensions, Weyl

semimetals [17], Floquet insulators [18], and even non-Hermitian systems with gains and losses [19, 20], to name a few.

In the literature, systems with exotic edge states have yet to find experimental realization. An example of this, and interest in this thesis project, is the modified Haldane model proposed by Colomés and Franz [2]. This two-dimensional model shows a surprising property: co-propagating edge states (i.e., states localized on each edge propagate in the same direction, in contrast to what happens in the QHE where states propagate in opposite directions for the same spin, schematized in Fig.1.1). Specifically, Colomés and Franz use a honeycomb lattice (like graphene), including second neighbor couplings of the Haldane type but with a different arrange of phases. Another interesting result is that these unusual edge states coexist with bulk states that compensate for the edge states so that the transmission probabilities remain reciprocal.

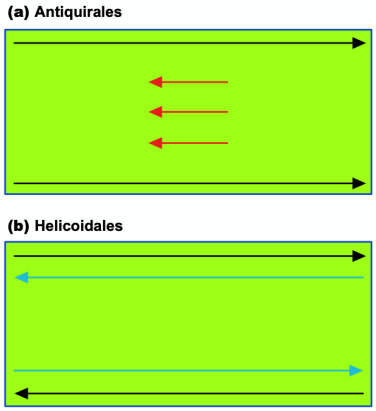

Figure 1.1: **a)** Scheme of the states in the Colomés and Franz model [2], showing copropagating states on its edges (black arrows) coexisting with bulk states in the opposite direction (red arrows). **b)** Scheme of typical states of a topological insulator: counterpropagating and spin-polarized. In cyan for *down* spin and black for *up* spin

How these systems are studied is quite diverse, ranging from experiments with ultra-cold fermions [12], through mechanical meta-materials [19], to optical dynamics in photonic networks [21, 22]. In this spirit, proposing a system analogous to topological networks but from a new perspective arises the topic of this thesis: through an electrical circuit.

1.1. Models, Materials and Topological insulators.

This section will review in detail some systems that are of particular interest to this thesis. As we embark on this journey of exploration, let us commence by solidifying our understanding starting with a historical remark, then proceed with the simplicity of a one-dimensional model and gradually progressing towards the intricate landscapes of two dimensional topological insulators.

1.1.1. Quantum Hall effect

In 1980, Klaus von Klitzing [11] was studying electronic transport in two dimension electronic gases (2DEG) at low temperatures $T \approx 1$K and a high intensity perpendicular magnetic

fields of around $B \approx 10$T. While measuring electronic transport, von Klitzing observed a remarkable phenomenon. The system exhibited a non-zero quantized Hall resistance, manifesting as plateaus in the conductance as a function of the applied magnetic field (Figure 1.2). Additionally, the longitudinal resistance remained near zero. The conductance was remarkably quantized in fundamental constants: e the electron charge, h the Planck constant, and an integer ν.

$$\sigma_H = \nu \frac{e^2}{h}; \tag{1.1}$$

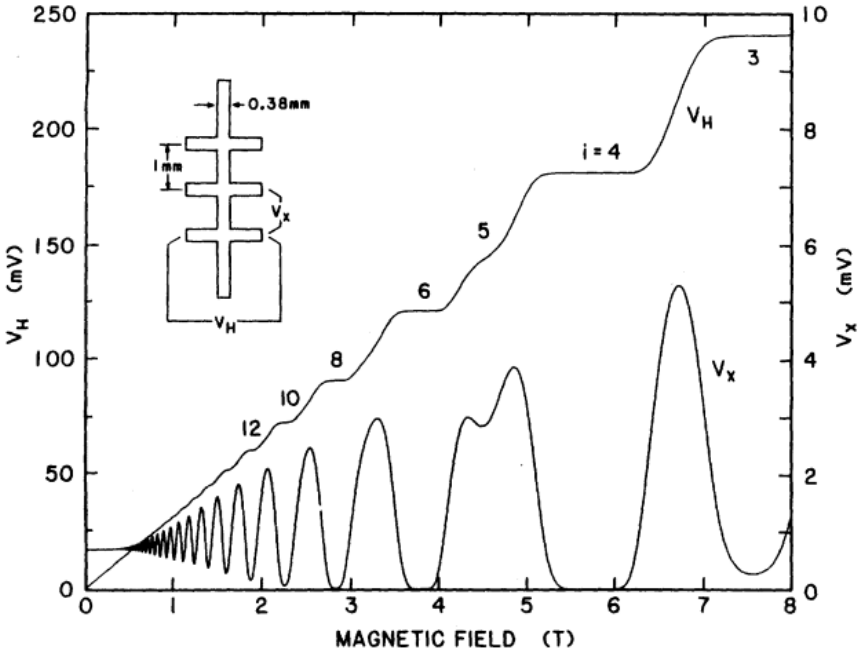

Figure 1.2: Hall Voltage V_H and longitudinal voltage V_x as a function of the magnetic field for the QHE. A scheme of the experimental setup is shown in the inset. Longitudinal voltage is in general zero, with peaks when the Fermi energy crosses a Landau level, and the Hall voltage changes value. © 1985 IEEE. Reprinted, with permission, from M. E. Cage, R. F. Dziuba and B. F. Field, "*A Test of the Quantum Hall Effect as a Resistance Standard,*" in IEEE Transactions on Instrumentation and Measurement, vol. IM-34, no. 2, pp. 301-303, June 1985, doi: 10.1109/TIM.1985.4315329.[23].

He measured values of ν to be exact integers with an astonishing precision of one part in a billion [24]. This discovery revolutionized the understanding of electrical resistance and played a crucial role in defining the fine-structure constant (α) [25]. The profound implications of the QHE and the exceptional precision awarded von Klitzing the 1985 Nobel Prize in Physics.

The underlying explanation of the QHE emerged through the contributions of numerous researchers. Initially, the focus shifted towards conductive chiral edge states within the sample [26, 27]. These states were characterized as exponentially localized and exhibited current flow in opposite directions along the edges. Later developments explored the QHE through the lens of topological invariants. The integer ν in the conductance quantization was identified as the Chern number, a specific topological invariant [28]. This connection between the QHE

and topological invariants provided a profound understanding of the phenomenon beyond the initial description of edge states. It established the QHE due to the system's underlying topological nature.

1.1.2. Su-Schrieffer-Heeger model

The first model we are interested in is the Su-Schrieffer-Heeger (SSH) model, initially proposed to understand the electronic properties of polyacetylene $(CH)_x$, a one-dimensional chain of alternating carbon and hydrogen atoms [29]. Figure 1.3 visually depicts this chain structure. We are interested in this model because is the simplest physical system showing topological property[30].

The SSH model describes a system with alternating single and double bonds, leading to step-wise hopping probabilities for electrons between neighboring sites. Interestingly, exchanging the single and double bonds does not alter the system's energy, resulting in two degenerate ground states. This degeneracy, a vital feature of the model's topological order, will be explored further in this section.

For simplicity, we will consider a lattice with a predefined dimerization (the difference in lengths between single and double bonds) without delving into the complexities that lead to this phenomenon.

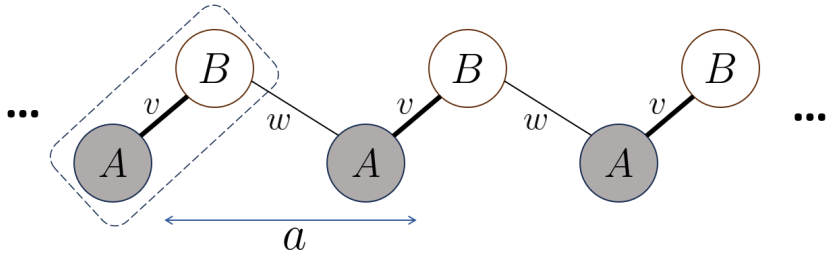

Figure 1.3: Graphical representation of the tight-binding SSH model. Sites A (B) are represented with grey (white) circles. Hoppings are depicted by black lines, note that intracell hoppings (v) are different than intercell ones (w). The unit cell is enclosed with dashed lines, and the lattice periodicity constant a is shown over the lattice.

For a chain of N unit cells, each containing two sites (A and B), the single-particle Hamiltonian describing an electron is:

$$H = \sum_{n}^{N} (\varepsilon_A c_{2n}^{\dagger} c_{2n} + \varepsilon_B c_{2n+1}^{\dagger} c_{2n+1}) + (v c_{2n}^{\dagger} c_{2n+1} + w c_{2n+1}^{\dagger} c_{2n+1} + h.c.), \tag{1.2}$$

where c_{2n} (c_{2n+1}) represents the electron annihilation operator on the A (B) site in the n-th unit cell, ε_A (ε_B) denotes the on-site energy of the A (B) sub-lattice, v is the hopping amplitude within a unit cell and w the hopping amplitude between adjacent unit cells. For convenience, we set $\varepsilon_A = \varepsilon_B = \varepsilon$, meaning the same on-site energy for all sites. This introduces a constant energy shift in the spectrum and can be neglected for our analysis since it does not alters the states. In real-space representation, the SSH Hamiltonian matrix for a $N = 3$

chain with open boundary conditions reads as:

$$H = \begin{pmatrix} 0 & v & 0 & 0 & 0 & 0 \\ v & 0 & w & 0 & 0 & 0 \\ 0 & w & 0 & v & 0 & 0 \\ 0 & 0 & v & 0 & w & 0 \\ 0 & 0 & 0 & w & 0 & v \\ 0 & 0 & 0 & 0 & v & 0 \end{pmatrix}. \tag{1.3}$$

Thanks to the translation symmetry of the lattice, we can use the momentum k as a quantum number and take advantage of Bloch's theorem. Diagonalizing the Hamiltonian by using a Fourier transform as:

$$c_{2n} = \int_{-\pi/a}^{\pi/a} dk e^{ikan} c_A(k), \tag{1.4}$$

$$c_{2n+1} = \int_{-\pi/a}^{\pi/a} dk e^{ikan} c_B(k), \tag{1.5}$$

giving a Hamiltonian as:

$$H = \int_{\pi/a}^{\pi/a} dk \psi_k^\dagger \mathcal{H}(k) \psi_k, \tag{1.6}$$

with $\psi_k = (c_A(k), c_B(k))^T$, and the Bloch Hamiltonian:

$$\mathcal{H}(k) = \begin{pmatrix} 0 & v + we^{-ika} \\ v + we^{ika} & 0 \end{pmatrix}. \tag{1.7}$$

The eigenvalues $E(k)$ can be obtained from equation 1.7 as:

$$E(k) = \pm\sqrt{(v + we^{-ika})(v + we^{ika})} = \pm\sqrt{v^2 + w^2 + 2vw\cos(ka)}, \tag{1.8}$$

and, given $\phi(k) = arg(v + we^{ika})$, the bulk eigenstates:

$$|u_\pm(k)\rangle = \frac{\sqrt{2}}{2} \begin{pmatrix} \pm e^{i\phi(k)} \\ 1 \end{pmatrix}. \tag{1.9}$$

Since this thesis focuses on edge states, let's explore the eigenstates of a finite SSH chain to identify their presence. We will utilize Open Boundary Conditions (OBCs) to simulate an open system. Specifically, we choose to start with an A site and end with a B site.

We compute the system's eigenvalues and eigenstates by diagonalizing the finite Hamiltonian matrix obtained for this specific configuration. Figure 1.5(b) showcases the resulting band structure for various values of the intracell hopping parameter (v) while keeping the intercell hopping parameter (w) fixed. We observe the emergence of certain states within the band gap for specific values of v. Furthermore, the gap closes entirely when v and w become equal ($v = w = 1$), and these additional states subsequently disappear.

Figure 1.5(a) depicts the zero-energy eigenmodes corresponding to these gap states. We can observe their localization at the chain's edges, confirming their identity as edge states.

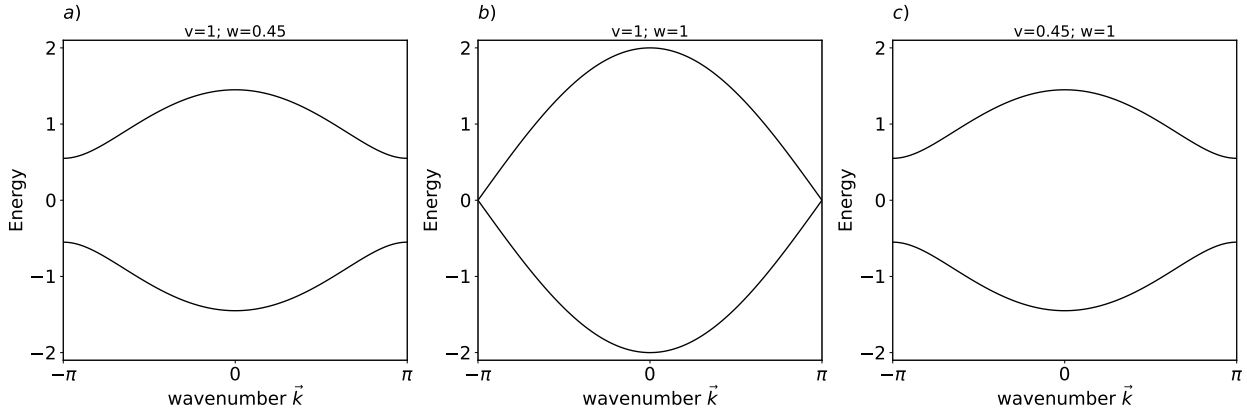

Figure 1.4: Dispersion relations of the SSH model, for three arranges of parameters: **a)**: $v = 1$, $w = 0.45$; **b)**: $v = 1$, $w = 1$; **c)**: $v = 0.45$, $w = 1$. For $v = w$ the gap closes, and exchanging v with w the bands are the same.

While the band structures might appear identical for systems with the same v and w values, our observations suggest that crucial information beyond the band structure exists. This observation hints at the potential presence of a topological transition, where the system's properties undergo a fundamental change that cannot be captured solely by its band structure by altering the system's parameters (like v and w in this case).

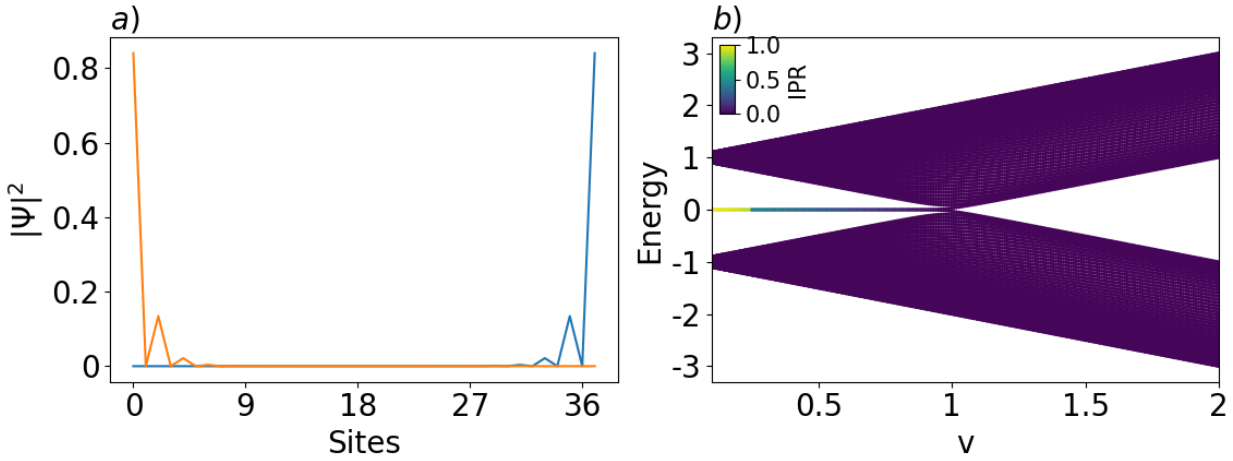

Figure 1.5: **a)** Probability distribution of the two edge states on each site of a SSH model with 19 unit cells, $v = 0.4$ and $w = 1$. **b)** Eigenvalues of a finite SSH model with 50 unit cells, as a function of v and fixed $w = 1$. There are two degenerate edge states with zero energy living in the gap when $|v| < |w|$. The color scale corresponds to the localization of each state measured by the inverse participation ratio (IPR). For a given state $|\Psi\rangle = \sum_n \alpha_n |c_n\rangle$ the IPR is obtained by $IPR = \sum_n |\alpha_n|^4$. Resulting equal to 1 (0) for a fully localized (extended) state.

Let's shift our focus toward the Bulk Hamiltonian to explore this possibility. This Hamiltonian captures the system's collective behavior within its bulk region, excluding the edges.

Equation 1.7 represents the SSH model's Hamiltonian but we can utilize an alternative

representation using the Pauli matrices and introducing a non-zero difference (Δ) between the on-site energies of A and B sites:

$$\begin{aligned}\mathcal{H}(k) &= \begin{pmatrix} \Delta & v + we^{ika} \\ v + we^{ika} & -\Delta \end{pmatrix} \\ &= \vec{h} \cdot \vec{\sigma}. \end{aligned} \tag{1.10}$$

Here, $\vec{\sigma} = (\sigma_x, \sigma_y, \sigma_z)^T$ denotes the vector of Pauli matrices. And $\vec{h} = (v+w\cos(ka), w\sin(ka), \Delta)^T$ is a newly defined vector. This reformulation highlights the critical role of Δ in the system's behavior. It becomes clear that only when $\Delta = 0$ can the gap in the band structure close. This condition arises because the eigenvalues (energy spectrum) of the Hamiltonian are given by: $E = \pm|\vec{h}| = \pm\sqrt{\Delta^2 + v^2 + w^2 + 2vw\cos(ka)}$. Therefore, the energy gap remains open unless Δ becomes zero, regardless of the values of v and w.

Even though exchanging v and w does not affect the band structure, continuously transforming one system into the other while maintaining an open gap ($\Delta \neq 0$) is impossible. Adding the Δ term can break the system's topological order.

To clarify this, we analyze the path traced by the endpoint of the vector $\vec{h}$ (defined in Equation 1.10) as we traverse the Brillouin zone. Regardless of the system configuration, this path will always form a closed loop. Crucially, when $\Delta = 0$, the path of $\vec{h}$ remains confined to the d_x,d_y plane. If the origin lies on this path for a specific momentum value (k), the band gap closes at that k, leading to the previously discussed transition. Figure 1.6 shows a visual representation of this vector traversing the Brillouin zone.

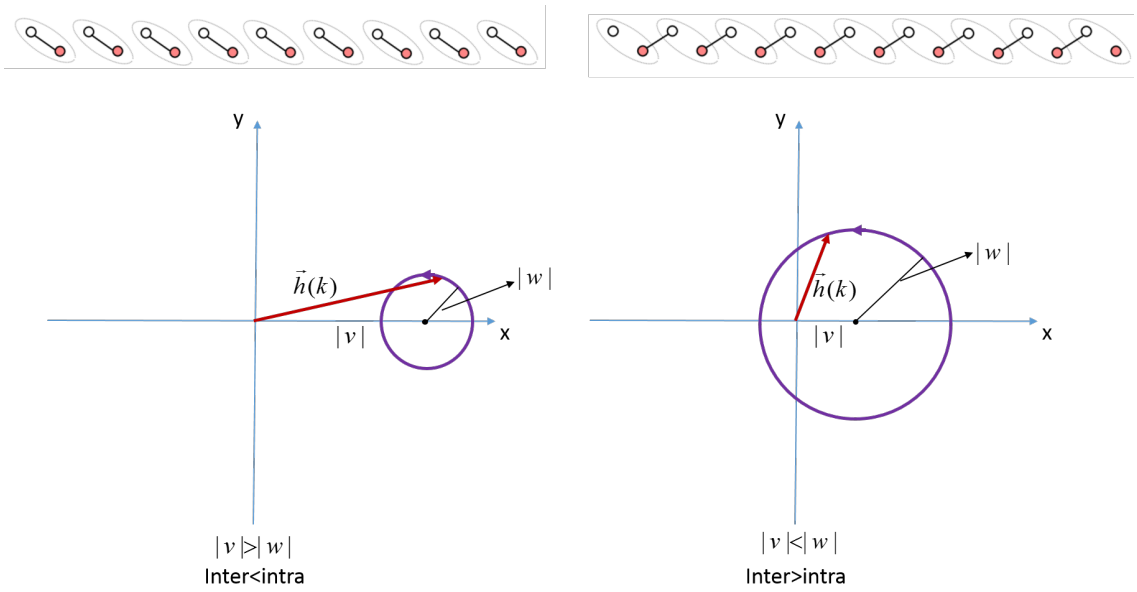

Figure 1.6: Schematic representation of the path traced by $\vec{h}$ by sweeping through the Brillouin zone in both trivial (not enclosing the origin) and topological (enclosing the origin) phases. Figure from Baocheng Zhu, *Lecture notes on Topological Insulators* [31].

This path possesses a well-defined winding number (ν) around the origin, which is a powerful tool for characterizing the system's topology. By introducing the unit vector $\hat{h} = \frac{h}{|h|}$,

the winding number can be calculated as [32]:

$$\nu = \frac{1}{2\pi} \int \left(\hat{h}(k) \times \frac{d}{dk} \hat{h}(k) \right)_z dk. \tag{1.11}$$

Interestingly, the winding number in the SSH model can only take two values: 0 or 1, depending on the chosen parameters. The system is considered in its trivial phase when the intracell hopping (v) surpasses the intercell hopping (w), resulting in a winding number of 0. In contrast, when w exceeds v, we obtain a winding number of $\nu = 1$, signifying the topological phase.

To conclude, a topological invariant is defined as an integer that characterizes an insulating system (possessing a gap in its energy spectrum) and remains unchanged under continuous transformations (adiabatic deformations). These invariants presents two key properties:

- They are only well-defined in the limit of infinitely large systems (thermodynamic limit).
- They depend on the specific symmetries that must be preserved during the transformations.

The winding number (ν) of the SSH model serves as a prime example of a topological invariant, revealing the system's underlying topological nature.

1.1.3. Graphene

After exploring the Su-Schrieffer-Heeger model, using it as an example for future models by having characterized its topological characteristics, we turn our attention to graphene. This material consists of a single layer of carbon atoms arranged in a honeycomb lattice. Despite its seemingly simple structure, graphene possesses remarkable properties, including high mechanical strength [33], high thermal conductivity [34] and electrical conductivity [35], and the distinction of being the first isolated 2D material. The groundbreaking characterization of its electrical properties made by Geim and Novoselov [36, 37] in 2004 opened a new era of research. Now we study its characterisation and electronic properties using a tight-binding perspective in order to use this as a basis for other systems.

We describe the graphene structure as a triangular Bravais lattice with two atoms per unit cell. Its lattice vectors are:

$$\vec{a}_1 = a\left(-\frac{1}{2}\hat{x} + \frac{\sqrt{3}}{2}\hat{y}\right); \quad \vec{a}_2 = a\left(\frac{1}{2}\hat{x} + \frac{\sqrt{3}}{2}\hat{y}\right); \quad \vec{\delta} = \frac{a}{\sqrt{3}}\hat{y}, \tag{1.12}$$

where $a = a_0\sqrt{3}$ with $a_0 \approx 0.142$nm. The nearest-neighbor vectors connecting sites A and B are:

$$\vec{\delta}_1 = \frac{a}{\sqrt{3}}\hat{y}; \quad \vec{\sigma}_2 = a\left(\frac{1}{2}\hat{x} - \frac{1}{2\sqrt{3}}\hat{y}\right); \quad \vec{\sigma}_3 = a\left(-\frac{1}{2}\hat{x} - \frac{1}{2\sqrt{3}}\hat{y}\right). \tag{1.13}$$

The reciprocal lattice vectors, obtained using $\vec{a}_i \cdot \vec{b}_j = 2\pi\delta_{ij}$, are:

$$\vec{b}_1 = \frac{4\pi}{a}\left(-\frac{1}{2}\hat{x} + \frac{1}{2\sqrt{3}}\hat{y}\right); \quad \vec{b}_2 = \frac{4\pi}{a}\left(\frac{1}{2}\hat{x} + \frac{1}{2\sqrt{3}}\hat{y}\right). \tag{1.14}$$

These vectors define the first Brillouin zone, which inherits the hexagonal shape of the underlying Bravais lattice (Figure 1.7b). Notably, this zone has two nonequivalent vertices, denoted

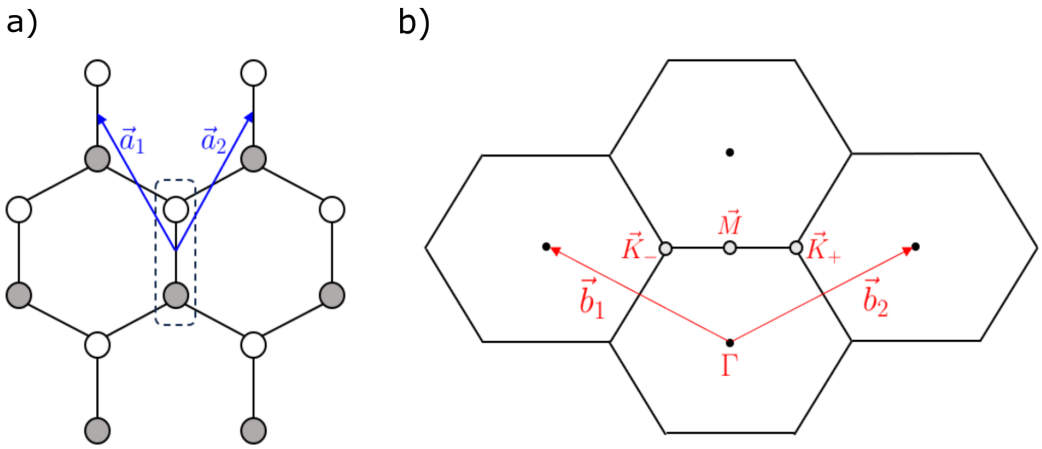

Figure 1.7: **a)** Graphene scheme lattice, the honeycomb structure is produce by a bipartite triangular Bravais lattice with site A (grey dots) and B(white dots). The lattice vectors are highlighted in blue. **b)** Reciprocal lattice described by the reciprocal vectors $\vec{b}_1$ and $\vec{b}_2$ highlighted in red. The first Brillouin zone lies in just one hexagon, high symmetry point are pointed in the lattice.

as:

$$\vec{K}_+ = \frac{4\pi}{3a}\left(\frac{1}{2}\hat{x} + \frac{\sqrt{3}}{2}\hat{y}\right) \quad \vec{K}_- = \frac{4\pi}{3a}\left(-\frac{1}{2}\hat{x} + \frac{\sqrt{3}}{2}\hat{y}\right), \tag{1.15}$$

and another high symmetry point denotes as $\vec{M} = \frac{2\sqrt{3}\pi}{3a}\hat{y}$. With this, we now explore the electronic structure of this material.

1.1.3.1. Graphene band structure

To obtain the spectrum of an infinite graphene surface, we start by defining its tight-binding Hamiltonian. Since graphene is made only with carbon atoms, the onsite energy of A and B sites are the same. Considering c_i the electronic annihilation operator in site i, the Hamiltonian is:

$$H = E_0 \sum_i c_i^\dagger c_i + t \sum_{\langle ij \rangle} c_i^\dagger c_j. \tag{1.16}$$

Here, t accounts for the first neighbor hopping amplitude between sites. For graphene, this quantity is $t \approx 3.0eV$[38], but we will leave this quantity unspecified since we care more about the system's structure than the carbon atoms themselves. Also, since E_0 only imposes a shift in the spectrum, we set $E_0 = 0$ for convenience.

Counting in translational symmetry produced by the lattice vector, we use $\vec{k}$ as a quantum number and take advantage of the Bloch theorem by diagonalizing the Hamiltonian with a Fourier transform. This procedure is standard in solid-state physics as we did before for the SSH system, but now we apply it in 2 dimensions

$$c_i(\vec{r}_i) = \frac{1}{\sqrt{N}} \sum_{\vec{k}} c_i(\vec{k}) e^{i\vec{k}\cdot\vec{r}_i}. \tag{1.17}$$

leading to a Hamiltonian as:

$$H = \sum_{\vec{k}} \Psi^{\dagger}_{\vec{k}} \mathcal{H}(\vec{k}) \Psi_{\vec{k}}, \tag{1.18}$$

with $\Psi^{\dagger}_{k} = (c^{\dagger}_{A\vec{k}}, c^{\dagger}_{B\vec{k}})$, and the Bloch Hamiltonian

$$\mathcal{H}(\vec{k}) = \begin{pmatrix} 0 & t\alpha(\vec{k}) \\ t\alpha(\vec{k})^{*} & 0 \end{pmatrix}, \tag{1.19}$$

where $\alpha(\vec{k}) = (1 + e^{-i\vec{k}\cdot\vec{a}_1} + e^{-i\vec{k}\cdot\vec{a}_2})$ as discussed in [39]. With this Hamiltonian we obtain the dispersion relation by diagonalizing the 2×2 matrix:

$$E(\vec{k}) = \pm t|\alpha(\vec{k})| \tag{1.20}$$

$$= \pm t\sqrt{3 + 2\cos\Big(\vec{k}\cdot\vec{a}_1\Big) + 2\cos\Big(\vec{k}\cdot\vec{a}_2\Big) + 2\cos\Big(\vec{k}\cdot(\vec{a}_2 - \vec{a}_1)\Big)}, \tag{1.21}$$

replacing the lattice vectors and working out the trigonometric functions we obtain:

$$E(k_x, k_y) = \pm t\sqrt{1 + 4\cos\frac{\sqrt{3}k_x a}{2}\cos\frac{k_y a}{2} + 4\cos^2\frac{k_y a}{2}}. \tag{1.22}$$

The wavevectors $\vec{k} = (k_x\hat{x} + k_y\hat{y})$ are within the first hexagonal Brillouin zone. If the bands crosses then $\alpha(\vec{k}) = 0$, it can be verified that this occurs only for $\alpha(\vec{k} = \vec{K}_{\pm})$, therefore the crossing occurs at the points $\vec{K}_{+}$ and $\vec{K}_{-}$ just as depicted in Figure 1.8.

The "touching" between the conduction and valence bands has remarkable consequences if we work at low energies near $\vec{K}_{+}$ or $\vec{K}_{-}$. By working up a Taylor expansion of the Hamiltonian 1.19 near the special points, we obtain:

$$\mathcal{H}_{\pm}(\vec{q}) = -\frac{\sqrt{3}}{2}(\pm q_x\sigma_x + q_y\sigma_y), \tag{1.23}$$

where $\pm$ denotes for $\vec{K}_{+}$ and $\vec{K}_{-}$, $\vec{q}$ is the momentum measured from the special points and $\sigma_{x,y}$ are the first and second Pauli matrices. This Hamiltonian corresponds to massless fermions in a linear dispersion and velocity $\hbar c = \frac{\sqrt{3}}{2}ta$ as is the electrons where Dirac fermions.

As mentioned for SSH, this thesis is interested in edge states more than anything else, so we will leave the description of symmetries out of this discussion; if the reader is curious, the work of Rodriguez [40] would be helpful.

If we want to produce a finite system, the results will vary depending on the type of edge termination we impose. For this thesis, we focus on zig-zag terminations like in the ribbons shown in 1.9.

This section has established the key features of the graphene lattice, including its defining vectors and the resulting reciprocal space with its Brillouin zone.

A subsequent subsection will address further exploration of graphene and other systems, particularly their ribbon band structures and the potential presence of edge states, building upon the foundation laid here.

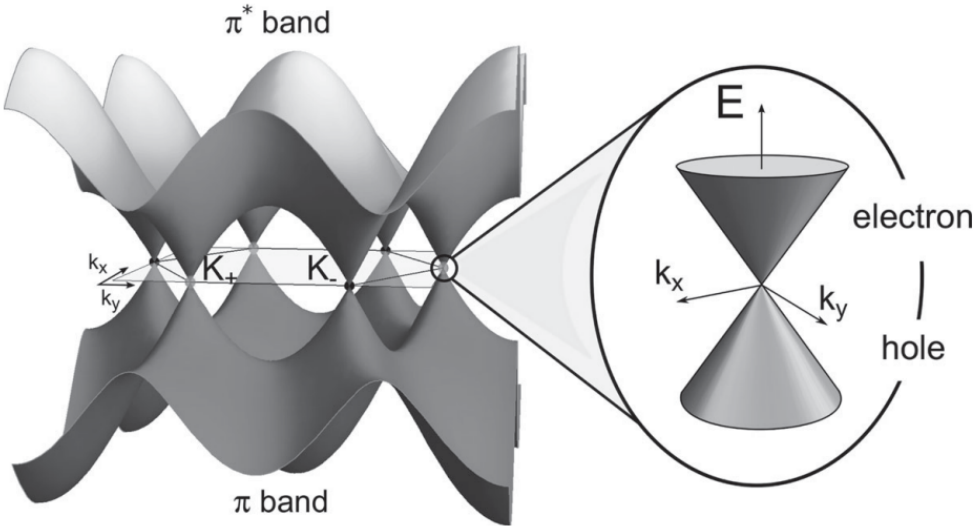

Figure 1.8: Graphene band structure. π^* band correspond to the conduction band and π to the valence band. The dispersion relation is linear close the $\vec{K}_+$ (gray dots) and $\vec{K}_-$ (black dots), this produces what are known as "Dirac cones" at this points. Figure from Fòa Torres, L.E.F., Roche, S. and Charlier, J.-C. (2020) 'Electronic Properties of Carbon-Based Nanostructures', in *Introduction to Graphene-Based Nanomaterials: From Electronic Structure to Quantum Transport*. Cambridge: Cambridge University Press, pp. 11–69. [39]. Reproduced with permission of Cambridge University Press through PLSclear.

1.1.4. Haldane model

While graphene on its own is not in a topological phase, the work of Duncan Haldane adds a clever twist to this. He proposed a modified graphene model known as the Haldane model to obtain the Quantum Hall Effect (QHE) without Landau levels [10].

The model changes graphene by breaking inversion symmetry and time-reversal symmetry, showing the theoretical foundation of topological insulators. This changes in the Hamiltonian are the following:

1. Adding a mass term with sub-lattice dependence (differing between sites A and B).
2. Adding a complex term to the hopping interaction between atoms that are next-nearest neighbors (NNN). This term has the form $t_2 e^{i\phi}$, where t_2 represents the hopping amplitude and ϕ is a phase factor.

As Haldane highlights, the specific pattern of this phase factor $e^{i\phi}$ serves to mimic the effects of a synthetic magnetic field within the material. However, this approach achieves the desired effect without introducing any magnetic flux. These additions produce a Hamiltonian as

$$H = \Delta \sum_j \xi_j c_j^\dagger c_j + t_1 \sum_{\langle i,j \rangle} c_i^\dagger c_j + t_2 \sum_{\langle\langle i,j \rangle\rangle} c_i^\dagger c_j e^{-i\epsilon_{ij}\phi}, \tag{1.24}$$

where $\xi_j = +1$ when $j \in A$, $\xi_j = -1$ when $j \in B$, ϵ_{ij} indicates the sign of the phase, Figure 1.10 presents a scheme to understanding this sign with the direction of each arrow been the positive and the opposite direction the negative. Following the approach with graphene, we

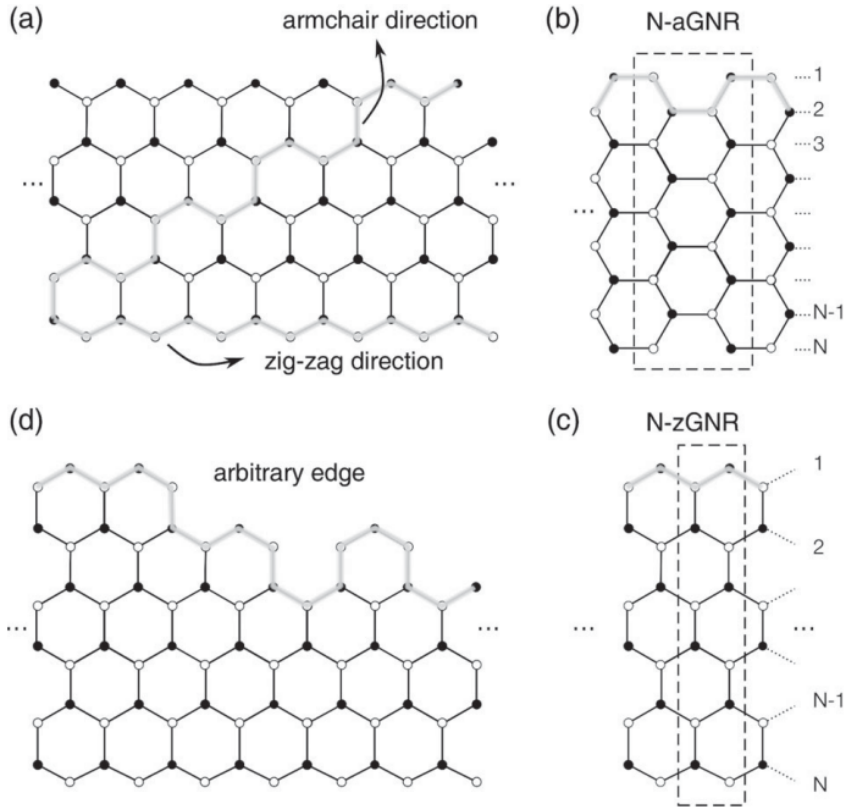

.

Figure 1.9: **a)** Scheme of the Graphene lattice, in light grey are highlighted cut directions to obtain both armchair and zigzag terminations.**b)** and **c)** show Ribbons with armchair and zigzag edges where the shape of the edges at the top of each scheme is highlighted. The unit cell is portrait in the dashed boxes. **d)** A general shape ribbon. Figure from Fòa Torres, L.E.F., Roche, S. and Charlier, J.-C. (2020) 'Electronic Properties of Carbon-Based Nanostructures', in *Introduction to Graphene-Based Nanomaterials: From Electronic Structure to Quantum Transport*. Cambridge: Cambridge University Press, pp. 11–69. [39]. Reproduced with permission of Cambridge University Press through PLSclear.

apply the Fourier transform to the Hamiltonian using eq.1.17.

$$H = \sum_{\vec{k}} \Psi^{\dagger}_{\vec{k}} \mathcal{H}(\vec{k}) \Psi_{\vec{k}}, \tag{1.25}$$

where, again, $\psi^{\dagger}_{\vec{k}} = c^{\dagger}_{A\vec{k}}, c^{\dagger}_{B\vec{k}}$ along with the bloch Hamiltonian

$$\mathcal{H}(\vec{k}) = \begin{pmatrix} \Delta + t_2\beta_A(\vec{k}) & t_1\alpha(\vec{k}), \\ t_1\alpha(\vec{k})^* & -\Delta + t_2\beta_B(\vec{k}), \end{pmatrix} \tag{1.26}$$

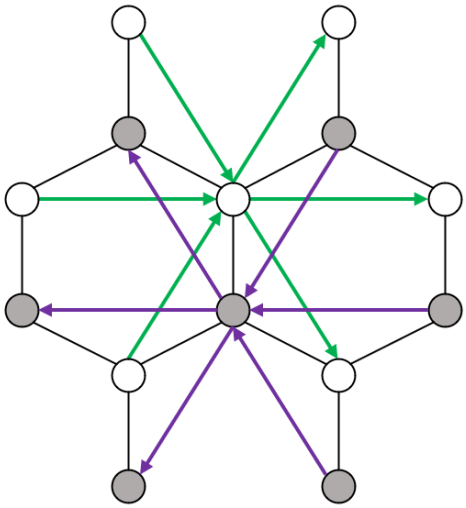

Figure 1.10: Scheme for NNN hoppings for the Haldane model. Purple (Green) arrows for sub-lattice A (B) with onsite energy Δ ($-\Delta$). The direction of each arrow indicate the positive phase $+\phi$, negative phase is each arrow in opposite direction.

with $\alpha(k)$ the same factor as in eq. 1.19 and the new terms

$$\beta_A(\vec{k}) = -2\sum_{\vec{b}_i}\cos\Big(\vec{k}\cdot\vec{b}_i + \phi\Big), \tag{1.27}$$

$$\beta_B(\vec{k}) = -2\sum_{\vec{b}_i}\cos\Big(\vec{k}\cdot\vec{b}_i - \phi\Big), \tag{1.28}$$

where the vectors $\vec{b}_i$ correspond to the positions of 3 NNN sites

$$\begin{aligned}\vec{b}_1 &= \vec{a}_1,\\ \vec{b}_2 &= \vec{a}_3,\\ \vec{b}_3 &= \vec{a}_1 - \vec{a}_2,\end{aligned} \tag{1.29}$$

A rearrangement of the Hamiltonian by using the Pauli matrices leads to

$$\mathcal{H}_{Hald}(\vec{k}) = t_1\Big[1+\cos\Big(\vec{k}\cdot\vec{a}_1\Big)+\cos\Big(\vec{k}\cdot\vec{a}_2\Big)\Big]\sigma_x + t_1\Big[\sin\Big(\vec{k}\cdot\vec{a}_1\Big)+\sin\Big(\vec{k}\cdot\vec{a}_2\Big)\Big]\sigma_y +$$

$$\Big[\Delta + 2t_2\sin\phi\sum_{\vec{b}_i}\sin\Big(\vec{k}\cdot\vec{b}_i\Big)\Big]\sigma_z + \Big[2t_2\cos\phi\sum_{\vec{b}_i}\cos\Big(\vec{k}\cdot\vec{b}_i\Big)\Big]\mathbb{I}, \tag{1.30}$$

identifying each term multiplying each Pauli matrix as the component $\vec{d}$ for $\mathcal{H}_{Hald} = \vec{d}\cdot\vec{\sigma} + d_0\mathbb{I}$, and of course $\vec{a}_1$ and $\vec{a}_2$ are the vectors defined for the Graphene triangular lattice. Diagonalizing this Hamiltonian we obtain the band structure

$$E(\vec{k}) = 2t_2\cos\phi\sum_{\vec{b}_i}\cos\Big(\vec{k}\cdot\vec{b}_i\Big) \pm \sqrt{t_1|\alpha(\vec{k})|^2 + \Big(\Delta + 2t_2\sin\phi\sum_{\vec{b}_i}\sin\Big(\vec{k}\cdot\vec{b}_i\Big)\Big)^2}. \tag{1.31}$$

We have effectively broken time-reversal symmetry. Thanks to the inversion and time-reversal breaking terms, an energy gap has been opened in the band structure.

The topological characterization is also presented in [10]; by varying the parameters, the system could manifest QHE and behave as a standard insulator for different combinations of M and ϕ. The various behaviors get encapsulated by the Chern number.

$$C = \frac{1}{4\pi} \int_{BZ} \frac{\vec{d}(\vec{k})}{|\vec{d}(\vec{k})|^3} \Big(\frac{\partial \vec{d}(\vec{k})}{\partial k_x} \times \frac{\partial \vec{d}(\vec{k})}{\partial k_x} \Big) d^2\vec{k}, \tag{1.32}$$

where $\vec{d}(\vec{k})$ is the vector identified before.

This number is a topological invariant, so as presented in the SSH model sections, it is computed for an infinite sheet of the model. $C = 0$ is achieved for $|M| > 3t_2 \sin\phi$, leaving the system as a trivial insulator. $C = \pm 1$ when $|M| < 3t_2 \sin\phi$ denotes the system as a "Chern insulator". This is represented in Figure 1.11 Of course, this topological order is accompanied by a special characteristic: when we have a nontrivial insulator $C \neq 0$, this number accounts for the total number of edge states moving through the boundary of a finite system.

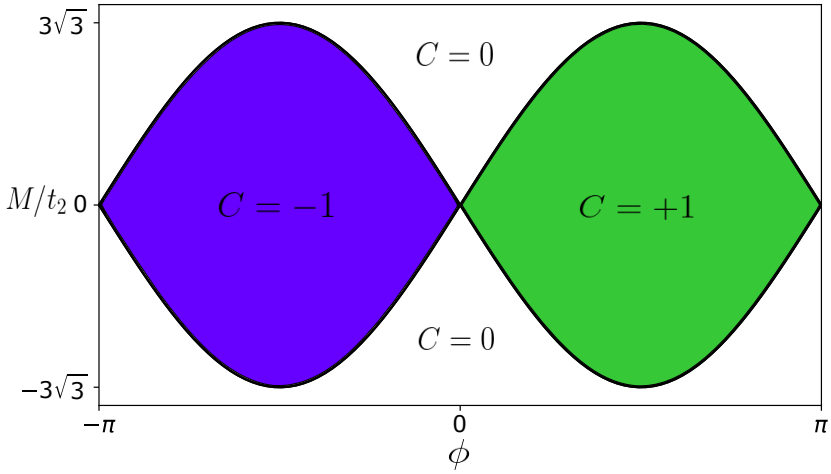

Figure 1.11: Phases Diagram of the Haldane model. As mentioned, the election of parameters influences the Chern number C, implying the total number of edge states.

This subsection reviewed the Haldane model, focusing on its topological characterization in the bulk. We use this model as a base for the following subsection.

1.1.5. Modified Haldane model

Another relevant model for this thesis is the modified Haldane model proposed by Colomés and Franz in 2018 [2]. We are motivated to study this model because it presents antichiral propagating edge states, as depicted in 1.1.

As the name suggests, this system directly modifies the Haldane model. This modification only affects the σ_z term in 1.30 by adding a shift between the Dirac points, thus paving the way for states with the same direction of propagation. Giving all NNN hoppings the same phase in each sub-lattice effectively changes σ_z into $\sigma_0 = \mathbb{I}$ achieving the desired result. In eq. 1.24 this is performed by imposing $\epsilon_{ij} = +1$ to all phases, this results in the scheme

illustrated in Figure 1.12.

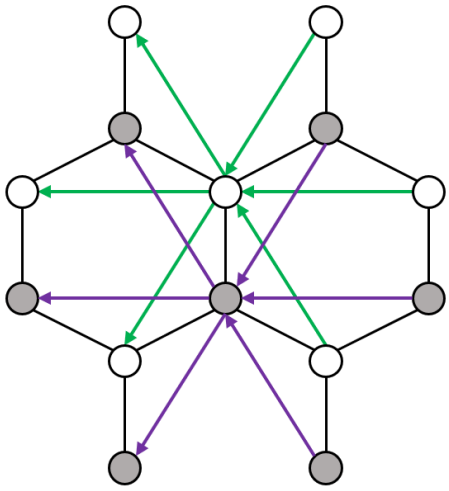

Figure 1.12: Phase sign convention for NNN hoppings in the modified Haldane model. Purple and green arrows for sub-lattices A and B achieve the same interactions. The direction of each arrow indicate the positive phase $+\phi$, negative phase is each arrow in opposite direction

We focus in the NNN term so we set $\Delta = 0$ for the on-site energies. By using the Fourier transform to this Hamiltonian we obtain

$$\mathcal{H}(\vec{k}) = \begin{pmatrix} t_2\beta(\vec{k}) & t_1\alpha(\vec{k}) \\ t_1\alpha(\vec{k})^* & t_2\beta(\vec{k}) \end{pmatrix}, \tag{1.33}$$

with the factor for the NNN hopping phase is just

$$\beta(\vec{k}) = -2\sum_{\vec{b}_i} \cos\Big(\vec{k}\cdot\vec{b}_i + \phi\Big). \tag{1.34}$$

differing from the two factors used in the Haldane model in eq.1.26. Dissecting this Hamiltonian with the Pauli matrices we get

$$\mathcal{H}_{MH}(\vec{k}) = t_1\Big[1 + \cos\Big(\vec{k}\cdot\vec{a}_1\Big) + \cos\Big(\vec{k}\cdot\vec{a}_2\Big)\Big]\sigma_x + t_1\Big[\sin\Big(\vec{k}\cdot\vec{a}_1\Big) + \sin\Big(\vec{k}\cdot\vec{a}_2\Big)\Big]\sigma_y +$$

$$2t_2\Big[\sin\phi\sum_{\vec{b}_i}\sin\Big(\vec{k}\cdot\vec{b}_i\Big) + \cos\phi\sum_{\vec{b}_i}\cos\Big(\vec{k}\cdot\vec{b}_i\Big)\Big]\mathbb{I}. \tag{1.35}$$

Thus, obtaining the band structure for this model by diagonilizing this Hamiltonian at each $\vec{k}$

$$E(\vec{k}) = t_2\beta(\vec{k}) \pm t_1|\alpha(\vec{k})|. \tag{1.36}$$

The intriguing part of this model comes from its edge states. This means that the final characterization for this model will come from the next section.

1.2. Zoology of edge states

In this section, we will show the type of edge states obtained from the two-dimensional systems we described before. Each edge state is associated with a specific band structure that will give us information about the directions for the propagation of these states.

Since we need boundaries for the edge states to exist, as mentioned in the Graphene subsection 1.1.3, we imposed zig-zag boundaries for all our two-dimensional materials. With this in mind, Figure 1.13 encapsulates the three systems we are interested in this thesis for the specific parameters mentioned in the caption.

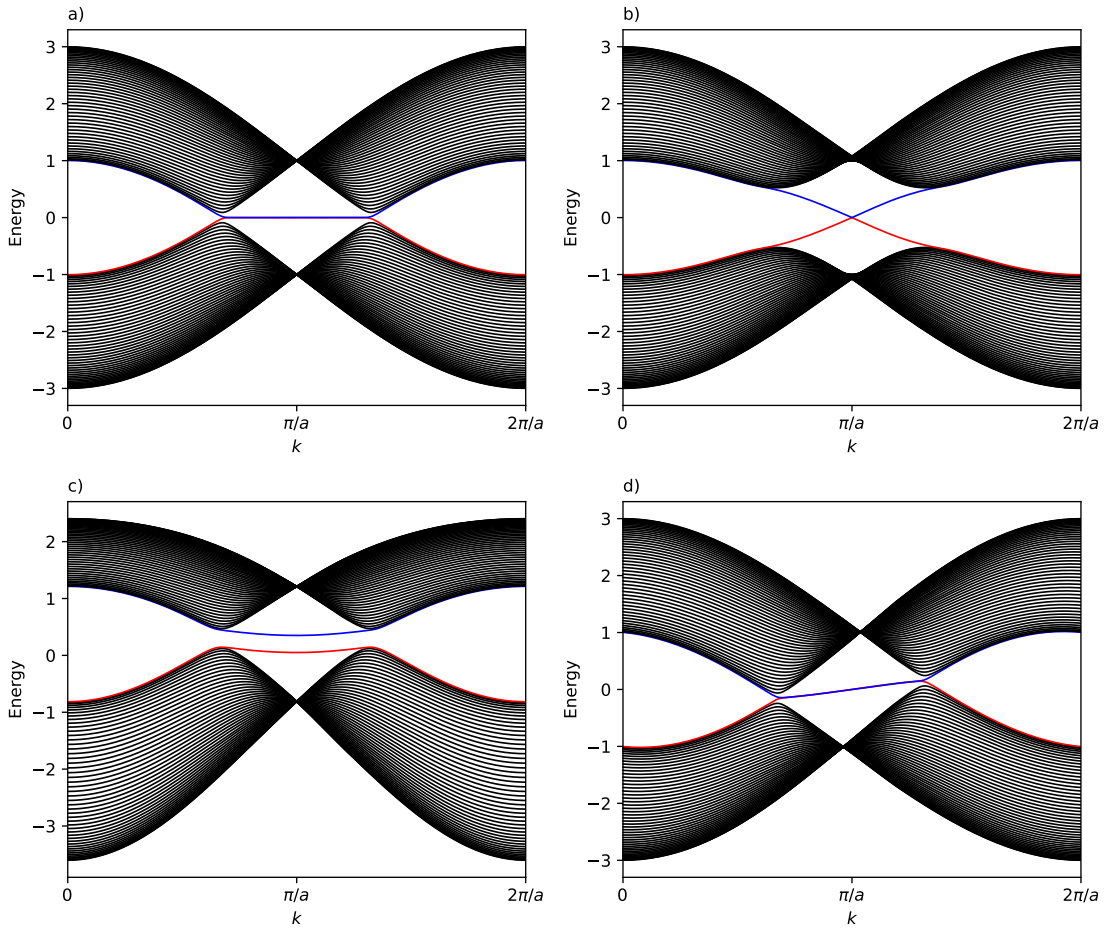

Figure 1.13: Band structure for **a)** Graphene model with $t = 1$, **b)** and **c)** correspond to the Haldane model in the topological ($\phi = \pi/2$, $t_2 = 0.1$ and $\Delta = 0$) and trivial ($\phi = 0$, $t_2 = 0.1$ and $\Delta = 0.15$) phases respectively and **d)** the modified Haldane model with $\phi = \pi/2$, $t_2 = 0.03$ and $t_1 = 1$. Here a corresponds to the lattice length found in 1.12.

We observe edge states in graphene, even though they are not topologically protected. This edge state is observed in the band structure 1.13a), residing near the $k = \pi$ region that looks like a flat band. The constant dispersion shows us that the propagation velocity is near 0 since

$$\vec{v}_g = \frac{1}{\hbar}\nabla_{\vec{k}} E \tag{1.37}$$

defines the *group velocity* $\vec{v}_g$ of the electron wavefunction [41]. For the Haldane model, thanks to Δ and $t_2 e^{i\phi}$ the band structure opens and the flat bands presented in graphene are now two bands crossing the gap, the edge states disappear? No, the two bands near the gap cross each other in $k = \pi$, presenting an opposite sign of slope, this produces two edge states traveling opposite directions at each boundary according to eq.1.37.

It is important to notice that the band structure presented in Figure 1.13 b) corresponds to the non-trivial phase and 1.13 c) accounts for the trivial phase. The first noticeable effect is that in Figure 1.13 c) the states in the near the gap do not cross each other.

Last but not least, the band structure of the modified Haldane model [2] in Figure 1.13 d) the Dirac points shift their energy, and the middle bands now present edge states but with the same direction of propagation (they have the same slope). These is states are called anti-chiral states and have been found in twisted graphene [42] and also as a result of electron-phonon interaction [43, 44] the characteristic discussed in the introduction called antichiral edge states.

Figure 1.14 presents a scheme for the propagating edge states in the Haldane and modified Haldane models.

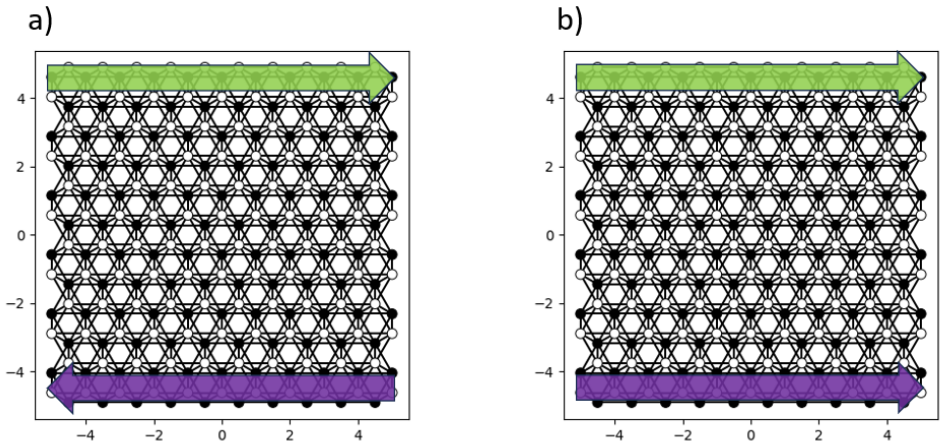

Figure 1.14: Direction of propagation of the edge states in the **a)** Haldane model, and **b)** the modified Haldane model.

1.3. Non Hermitian considerations

All the systems we have shown share one fundamental property: Hermiticity, meaning their Hamiltonian operator is self-adjoint, thus ensuring the conservation of probability. However, in recent years, there has been a trend in studying crystalline systems that do not preserve this property, where electron-electron or electron-phonon interactions [45, 46], disorder [47], and couplings between systems and the environment are commonly modeled with gains and losses [48, 49] through a non-Hermitian terms.

These interactions lead to the study of non-Hermitian systems, leading to a rich tapestry of novel phenomena. This became a field of research on its own, unraveling new topological phenomena produced by the non-preserving interactions [6, 50–52].

A non-Hermitian phenomenon that we are particularly interested in is the non-Hermitian Skin effect [6, 53], where the extended states of a finite system end up localizing close to a boundary, accompanied by a high sensitivity to boundary conditions. Since we are interes-

ted in building a bulk-boundary correspondence, this effect does not allow us to base the topological invariants on the bulk eigenstates.

Even though this effect is an obstacle, we can take advantage of some of its consequences to develop new physics. An example of this is shown in [4], where an unconventional reflection is characterized in the propagation of wave packets, dubbed the Dynamic Skin Effect, as a cause of both non-Hermitian Skin effect and the Hermitian wave packet spreading. A realization of this effect is studied in this work.

With this, we have finished the ground floor of this thesis. We have reviewed the systems crucial to this work and defined some characteristics for our future results. In the next section, we introduce the original ideas on topolectrical circuits and explain why this platform could help develop new ideas on quantum materials.

1.4. Electrical circuits as simulators

In 2018, Stefan Imhof et al. [54] proposed to study topological phenomena utilizing electrical circuits as simulators. This innovative idea opened a new path to link the abstract theoretical framework of quantum materials with the experimental investigation.

This work served as a foundation for the field, where the versatility of electrical circuits opens the gates of creativity and allows investigators to reach beyond usual interactions and still obtain experimental confirmations without the usual limits.

By carefully designing circuits, research with this platform has helped to probe phenomena such as edge states [55], Chern insulators [56], topological transitions [57–59], and non-Hermitian phenomena [3, 60–62]. This scheme, apart from facilitating the study of topological physics, also promises to develop new electronic devices and applications.

The central idea is to use circuital formalism, resistor, capacitor, and inductor (RCL) components to construct analog systems similar to the ones we want to study. The circuit Laplacian governs the dynamic of the circuitry, which takes the role of the Hamiltonian, describing the evolution of a physical system.

a)

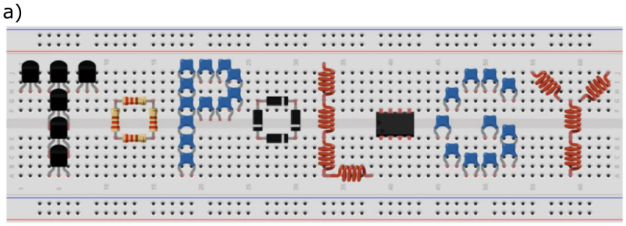

b)

Element	Picture	Symbol	Function	
Inductor (L)			Resonance	Hermitian
Capacitor (C)				
Resistor (R)			Loss	Non-Hermitian
Amplifier (U)			Gain	
Diode (D)			Non-reciprocity	
Transistor (T)			Non-linearity	
Superconducting qubit (Q)			Quantum circuit	

Figure 1.15: **a**) Conceptual sketch of topological experiments on a breadboard. **b**) Plethora of components that can be used in this circuitry. Image taken from Ling Lu. *Topology on a breadboard*. Nature Physics, [63] and *reproduced with permission from Springer Nature*

The accessibility, scalability, and operability of electronics help simplify the intricate boundary properties of topological phases. Freeing the research to experiment in physical models that, due to their simplifications, are too ideal for a realization in a lab. Also, these studies offer a quick and easy experimental approximation for researchers unfamiliar with complex experimental simulators. Additionally, the well-developed electrical engineering software enables platforms beyond traditional labs to study these systems effectively.

1.5. About this thesis

This thesis aims to study edge and topological states inspired by solid-state physics models via electrical circuits. The aim is to propose electrical circuits as a simulator or to realize ideas.

The objective of this thesis is twofold: **(i)** Re-examining known models and their realizations in electrical circuits and the opportunities that this simulator provides; **(ii)** use the experience in (i) to adventure a little further in new propositions.

With this in mind, as specific objectives, this thesis studies the SSH model, a graphene model and the Haldane model. We also propose circuits for the modified Haldane model [2], elucidating its antichiral states through the circuit and study the effects of gain and loss terms with simulations by electrical circuits [60, 62] by observing the Dynamic skin effect [4] in a proposed non-Hermitian SSH circuit.

This thesis is structured into four chapters encompassing the introduction, describing critical concepts as the foundation for exploration. The second chapter will focus into Laplacian theory, establishing the necessary tools for circuit exploration. The third chapter will present our results, ranging from known topological model realizations in circuits to our newly proposed modified Haldane circuit and the observation of Dynamic skin effect with its examination. The final chapter will provide an account of the conclusions drawn from this work.

Chapter 2

Circuit Analogs of quantum Hamiltonians: Design and Debugging

This chapter explores the potential of electrical circuits as tools for simulating tight-binding systems with translational symmetry. The focus is to design circuit analogies for lattice structures and establishing connections between circuit analysis and solid-state physics.

In the first section, we elaborate the concept of the circuit Laplacian, along its matrix representation and the parallels between circuit components and tight-binding model parameters.

The second section discusses the creation of specific circuit connections that model the hopping elements in tight binding models. Selecting circuit parameters and components is fundamental to replicate solid-state physics's properties and interactions.

The third section focuses on practical measurements and impedance structure analysis. We enable direct comparisons between circuit and solid-state band structures by extracting the admittance band structure through systematic procedures.

In the "Debugging with the Grounded Laplacian"subsection, we address discrepancies between the designed circuit and its solid-state counterpart. By analyzing the grounded Laplacian matrix, we identify and resolve issues, leading to a deeper understanding of circuit behavior.

This chapter provides formal guidance for researchers and engineers to design, measure, and debug topolectrical circuits, allowing to explore phenomena in condensed matter physics through electrical circuit emulation.

2.1. Laplacian formalism

If we want to simulate a tight-binding system with electrical circuits, it is necessary to know what the **circuit Laplacian** is. Consider a network with N nodes with D-periodic dimension. The connections between nodes are with components that do not generate power (passive elements), like resistors, inductors, and capacitors. These nodes are labeled with an index j from 1 to N, while the ground is labeled with 0 by convention. Let V_j and I_j be the **voltage measurement** to the ground (V_0) and the **current entering** the node j, respectively. Two nodes, j, and l, can be connected with an admittance g_{jl}, which is 0 if there is no connection. I_{jl} with 2 indices represents the current flowing from node j to node l. Using Kirchhoff's law of nodes, we obtain an equation for the total current on an arbitrary

node j:

$$I_j = \sum_{l=0}^{N} I_{jl} = \sum_{l=0}^{N} g_{jl}(V_j - V_l) = \sum_{l=0}^{N} J_{jl} V_l. \tag{2.1}$$

This equation can be written in matrix form as follows:

$$\mathbf{I} = J(\omega)\mathbf{V}, \tag{2.2}$$

where $\mathbf{V}$ and $\mathbf{I}$ have V_j and I_j for components, ω is the frequency of the oscillating voltage and J is the systems grounded Laplacian. The matrix J with elements J_{ij} governs the response of the circuit to a given signal.

The matrix J can be decomposed in the systems Laplacian $L = D - C$ and the matrix $W = diag(w_1, w_2, .., w_N)$. L encapsulates the structure of connectivity in the network, C is the adjacency matrix, and D contains the total conductance at each node. The matrix W shows the grounding of the circuit at each node.

An example of this can be seen in Figure 2.1, where the equation for node a is written as:

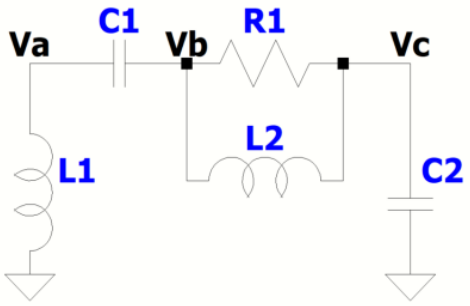

$$W = \begin{pmatrix} (i\omega L_1)^{-1} & 0 & 0 \\ 0 & 0 & 0 \\ 0 & 0 & i\omega C_2 \end{pmatrix}$$

$$C = \begin{pmatrix} 0 & i\omega C_1 & 0 \\ i\omega C_1 & 0 & (i\omega L_2)^{-1} + R_1^{-1} \\ 0 & (i\omega L_2)^{-1} + R_1^{-1} & 0 \end{pmatrix}$$

$$D = \begin{pmatrix} i\omega C_1 & 0 & 0 \\ 0 & i\omega C_1 + (i\omega L_2)^{-1} + R_1^{-1} & 0 \\ 0 & 0 & (i\omega L_2)^{-1} + R_1^{-1} \end{pmatrix}$$

Figure 2.1: Example of a circuit Laplacian $J = D - C + W$ in a illustrative RLC circuit of nodes $\{a, b, c\}$. Note that W and D are diagonal matrices that account for the total conductance of each node to ground and to the rest of the circuit respectively. C is the adjacency matrix containing the information on how nodes are related.

$$I_a = \sum_j C_{aj}(V_a - V_j) + w_a V_a = i\omega C_1(V_a - V_b) + \frac{1}{i\omega L_1} V_a, \tag{2.3}$$

Where I_a and V_a are the currents and voltages at node a. The incoming current I_a must be equal to the outgoing current flowing to each node j connected through a conductance C_{aj}, plus the current flowing directly to the ground through admittance w_a^{-1}. As mentioned in previous chapters, each admittance or conductance can be real or imaginary.

In this study, the circuits consist of repeating groups of M nodes and its corresponding conductance. These groups are collectively referred to as the unit cell. Each node in the circuit is assigned two indices: the first index, ρ, specifies the unit cell that the node belongs to, and the second index, α, specifies the node within the unit cell. For example, node $(2, 1)$ is the first node of the second unit cell.

The circuit Laplacian can be written as a function of the relative position between the

unit cells, $\mathbf{R}_\rho - \mathbf{R}_\sigma$, and the frequency of the voltage, ω:

$$J_{\rho,\alpha;\sigma,\beta}(\omega) = J_{\rho,\alpha}(\mathbf{R}_\rho - \mathbf{R}_\sigma, \omega), \tag{2.4}$$

this is because the Laplacian only depends on the connectivity of the nodes, which is the same for all unit cells, thus allowing a reciprocal space representation $J_{\alpha,\beta}(\mathbf{k})$.

Circuits are graphs, so their connectivity entirely determines them. Unlike the study of crystalline networks in solid-state physics, there is no fixed distance or orientation of the Bravais vectors of the network. An additional gauge for the circuit is introduced defined by the equivalent classes between all the different Bravais vectors that describe the circuit (any spacial arrangement of nodes is as good as any other) so the election of vectors is entirely arbitrary. Once we fix the vectors, the translational invariant J can be diagonalized using a spatial Fourier transform to D-dimensional reciprocal space k in M-dimensional block matrices.

$$J_{\alpha,\beta}(\mathbf{k}, \omega) = \sum_\rho J_{\alpha,\beta}(\mathbf{R}_\rho, \omega) e^{-i\mathbf{R}_\rho \cdot \mathbf{k}}. \tag{2.5}$$

This operation provides a mapping of the Laplacian spectrum to the wave vector k, establishing the admittance band structure of the circuit. Compared with tight-binding models, modifying the connections between nodes is the same as changing the hopping elements in the Hamiltonian. However, as can be seen in equation (2.2), this also affects the diagonal terms because of the total conductance in each node. Connections to the ground also appear as a diagonal term, which is accounted as on-site energy in a tight-binding model. At this point, it is possible to identify some analogies between each part of the circuit and its associated tight-binding model components, as shown in Table 2.1:

Table 2.1: Typical concepts of solid state physics find their analogue in circuit physics.

Concept on Solid state physics	Analogy on circuits
Sites	Nodes
Hamiltonian	Grounded Laplacian
Eigenvalue problem	Kirchhoff's equations
Hoppings	Conductivities connecting nodes
Onsite energies	Grounding terms + total conductance per node
Eigenenergies	Admittance
Wavefunction	Voltage profile

2.2. Designing Circuit Connections for Tight-Binding Emulation

In this subsection, we focus on designing connections that mimic the characteristics of tight-binding models using the circuit Laplacian as a parallel to a tight-binding Hamiltonian. We will make deliberate choices while developing these designs to ensure rigor and practicality. We discover practical ways to replicate the behavior of tight-binding interactions in circuits by examining specific connection designs.

2.2.1. Onsite terms

The effect of diagonal terms in the Hamiltonian can vary significantly depending on their implementation. One notable effect is the ability to shift the energy band structure, mainly when the terms are the same for all sites. Another effect is the potential to break inversion symmetry, for example, in a bipartite lattice, resulting in a gap opening.

When designing the diagonal terms in J, it is essential to be careful with their placement. The equation for $J = D - C + W$ in Figure 2.1 involves two diagonal matrices, D and W, with specific elements. Manipulating matrix D can be challenging because it depends on the total conductance of each node, which is affected by the connections between nodes. Therefore, a thorough understanding of node connections is needed to control the system's behavior.

Matrix W represents the admittance going from each node to the ground. It provides information about the components connected to the ground in each node. It is possible to directly connect passive elements like capacitors, inductors, or resistors to the ground to achieve specific effects, such as shifting the band structure. An important thing to have in mind when dealing with its admittance, $g_C = i\omega C$, $g_L = 1/i\omega L$, and $g_R = 1/R$, is that they can be real or imaginary. This allows the utilization of complex-valued terms in the circuit design with positive (capacitors) and negative (inductors) values.

To maintain the intuitive association of resistances with dissipative elements, components related to onsite energies (real terms in the Hamiltonian) are intentionally chosen to be purely imaginary. This choice involves predominantly using capacitors and inductors connected to ground. When comparing matrix J with the Hamiltonian H, it is necessary to match the real (imaginary) part of H with the imaginary (real) part of J, ensuring the parallelism between the two systems, which can be expressed by the equation

$$H = i\bar{J}. \tag{2.6}$$

A direct consequence of this choice is that the admittance band structure is now purely imaginary, in contrast to the energy band structure of a solid, which is strictly real in a Hermitian model.

While purely imaginary on-site terms are ideal for emulating solids and ensuring the hermiticity [57] of the system, parasitic resistances are unavoidable in realistic circuits. While these parasitic terms are typically small and uniform, they can affect the system's behavior. Therefore, it is important to consider the influence of both parasitic and the implemented imaginary terms when designing topolectrical circuits.

2.2.2. Hoppings

Hopping terms are at the core of the tight-binding approximation. These terms simplify complex theoretical interactions by representing the probability of an electron hopping from one atom to another in the lattice. Typically, hopping occurs between nearest neighbors, although longer-range interactions are also possible.

Designing hopping elements for the grounded Laplacian is straightforward. It involves connecting two nodes using circuit elements such as capacitors, inductors, or resistors. The matrix C in Eq. (2.2) contains information about the lattice connectivity. This matrix is designed to resemble the desired hopping elements in the Hamiltonian.

The circuit depicted in Fig. (2.1) has components C_1, R_1, and L_2 acting as nearest-neighbor (NN) hoppings, connecting nodes V_a with V_b and V_b with V_c. The effect of this arrangement on

the Laplacian preserves the same structure as a hopping term would have in the Hamiltonian, thanks to the current being equal to the conductance connecting the nodes multiplied by the voltage difference between the nodes (Eq. (2.1)).

It is important to note that in the given example, we connected the nodes V_b and V_c with more than two elements. As mentioned earlier, the graph nature of circuits allows for this flexibility in connectivity. In solid materials, this implies that a hopping term can be constructed from two different interactions, resulting in an "effective hopping" for that specific element. Additionally, one could connect nodes V_a and V_c with another element, introducing next-nearest-neighbor hopping to the Hamiltonian and enabling long-range interactions.

Following the same logic applied to defining onsite terms for emulating real-valued hoppings, we will utilize purely imaginary conductance, specifically inductors (representing negative conductance) and capacitors (representing positive conductance). Capacitors are generally used due to their positive values, but inductors are equally valid alternatives.

2.2.2.1. Designing non-reciprocal hopping elements with INICs

One type of connection utilized in this thesis uses an active element in order to obtain an active component connection. This connection is motivated by the Haldane model, discussed in Chapter 1, and involves a next-nearest-neighbor (NNN) complex hopping with a defined phase and magnitude. As mentioned before, an essential requirement for this element is its non-reciprocal nature from sites of the same sub-lattice. This section will focus on how to design this general type of connection rather than exploring its specific implementation within each lattice. The objective is to create the element (INIC) in its most general form without considering the particular context of a graphene-like structure or similar systems.

As a starting point, working with resistances could be a suitable approach. Resistances possess purely real admittance, which can result in a strictly imaginary hopping term. However, there are two significant challenges associated with this approach:

1. Resistances exhibit reciprocal admittance according to Equation (2.1).

2. This approach restricts us to a single phase, $\phi = \pi/2$.

An active element is required to overcome these limitations. By utilizing an operational amplifier (Op-Amp) and arranging the elements appropriately, an Impedance Converter with Current Inversion (INIC) is constructed. Figure 2.2 illustrates this component.

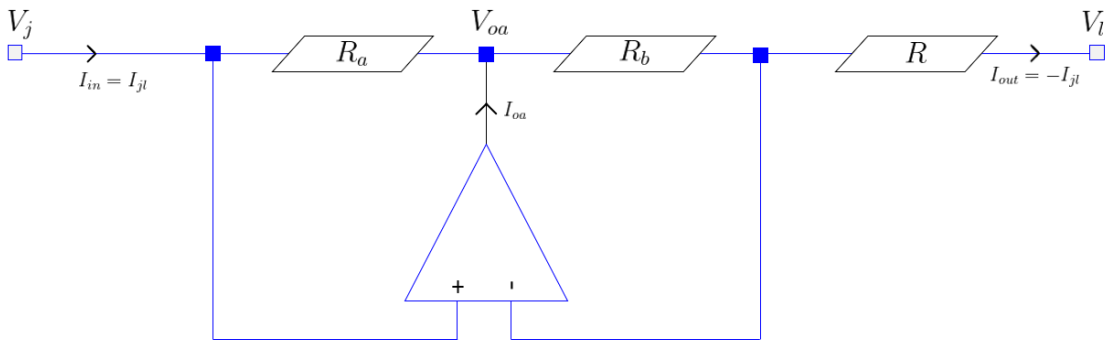

Figure 2.2: INIC electrical scheme based on the implementation of T. Hofmann *et al.*. Physical Review Letters, (**24**) 122 (2019)[56] with the notation accordingly to equation (2.7).

An INIC circuit primarily utilizes an Op-Amp to convert impedance and invert the current flowing through it. The Op-Amp [64], with its high-gain voltage amplification capabilities, amplifies the voltage across the input impedance. It accomplishes voltage amplification by applying negative feedback using external resistors or other components.

The current entering the operational amplifier is given by $I_{in} = (V_j - V_{oa})/R_a$, while the current leaving is $I_{out} = (V_j - V_l)/R$. Assuming an infinite impedance of the Op-Amp inputs, the relations simplify to $I_{out} = (V_{oa} - V_j)/R_b$ as no current can enter the Op-Amp. In Laplacian form, this yields [56]:

$$\begin{pmatrix} I_{in} \\ I_{out} \end{pmatrix} = \frac{1}{R} \begin{pmatrix} -\nu & \nu \\ -1 & 1 \end{pmatrix} \begin{pmatrix} V_j \\ V_l \end{pmatrix}, \tag{2.7}$$

where $\nu = R_b/R_a$. As the matrix is not symmetric, circuit reciprocity is broken.

The amplified voltage across the input impedance and inverted current allows the INIC to convert the impedance while maintaining a consistent relationship between the input and output signals. This is beneficial when interfacing different components or systems with mismatched impedance characteristics.

In summary, by utilizing the amplification and inversion capabilities of an Op-Amp, the INIC circuit can convert an impedance. This enables impedance matching with almost anything we would like to achieve. In particular, if $R_a = R_b$, the coupling gives R from in to out and $-R$ from out to in, just as the Haldane term needs. It is worth mentioning that this kind of elements can be easily generalized from resistances for any conductance; for example, in [62], the same idea is implemented with capacitors for a non-reciprocal nearest-neighbor connection.

The next section will focus on how to use the information gained from these circuits by measuring voltages and currents, with the objective of computing the admittance matrix.

2.3. Measuring Admittance Bands: Mapping Circuit Behavior to a Tight-Binding Model

This section focuses on the practical measurements and admittance structure analysis required to establish direct comparisons between circuit and solid-state band structures. By computing the admittance band structure researchers can gain valuable information about the behavior and characteristics of systems. The utilization of periodic boundary conditions (PBCs) to establish a reciprocal space representation of the Laplacian matrix and the subsequent measurement of the complete impedance matrix for each $\mathbf{k}$ are covered.

Impedance is a quantity commonly measured in the study of circuits, it reflects how the system resist the flow of current. Measuring it requires injecting a known current through the circuit and measuring the resulting voltage profile, then using a relationship between the voltage and the current the impedance is calculated. Applying an external current through a node j, the impedance is:

$$G_{ij} = V_i^{(j)}/I_j \Rightarrow \ V_i^{(j)} = G_{ij} I_j. \tag{2.8}$$

Here $V_i^{(j)}$ represents the voltage measured in node i when the only source of current is I_j.

One can rewrite the equation 2.8 in matrix form:

$$\mathbf{V} = G\mathbf{I}, \tag{2.9}$$

where G is called the impedance matrix. Identifying from eq.2.9 and eq.2.2 that $G = J^{-1}$ is in fact the inverse matrix of the Laplacian J. With this in mind, we now call the J matrix the "Admittance Matrix" and if the eigenvalues of G were to be obtained, the eigenvalues of J can be calculated by inverting those of G. If the other way around is needed then it can be expressed as $G = \sum_{j_n \neq 0} \frac{1}{j_n} \psi_n \psi_n^\dagger$, j_n are the admittance eigenvalues and ψ_n are the eigenvectors of J. This eigenvectors are related with the potential profile $\mathbf{V}$ proportional to the input current distribution $\mathbf{I}$. Also is worth noticing that if the circuit elements are reciprocal, then G is always symmetric [65].

For a system of N nodes, the process of exciting a node and measuring the voltage profile must be repeated N times to reconstruct the entire G matrix, with each N-th measurement exciting a different node. This process ensures the reconstruction of the complete G matrix, which can then be inverted to obtain J. This provides a direct measurement of the Laplacian matrix, akin to measuring the system's Hamiltonian, something that is typically challenging in generic transport or scattering experiments on physical crystals.

In contrast to solid-state physics, where translational invariance naturally exists in crystalline systems, circuits require the introduction of periodic boundary conditions (PBCs) to establish a periodic framework, enabling a reciprocal space representation of J. This allows for obtaining its eigenvalues j for each $\mathbf{k}$ and, consequently, the admittance band structure of the system $j(\mathbf{k})$ through direct measurement.

An issue arises with this approach, as the previously mentioned method requires N measurements, where N represents the total number of nodes in the circuit. However, assuming translational invariance (TI) symmetry in the systems and M nodes in each unit cell, then there are only M non-equivalent nodes, as each unit cell provides equivalent information for the analysis of the admittance structure. Therefore, to reconstruct G, it is sufficient to repeat the measurement procedure only M times, supporting each substructure once, significantly reducing the number of measurements.

In each of the M measurement procedures, the voltages of N nodes are obtained, and using the voltage and current information, the impedance matrix is reconstructed using eq.2.8, resulting in an $M \times N$ matrix G. The matrix is then Fourier transformed into the $(M \times M)$ matrix for each vector $\mathbf{k}$ using eq.(2.10), resulting in $G_{\alpha,\beta}(\mathbf{k})$. In this transformed matrix, the second index represents a node on the unit cell and is summed over all repetitions, encoding the information of each position in the indexation of $G_{\alpha,\beta}(\mathbf{R}_\rho)$ for all N nodes.

$$G_{\alpha,\beta}(\mathbf{k},\omega) = \sum_\rho G_{\alpha,\beta}(\mathbf{R}_\rho,\omega) e^{-i\mathbf{R}_\rho \cdot \mathbf{k}}. \tag{2.10}$$

To obtain the admittance band structure, the eigenvalues of the impedance matrix are calculated for each $\mathbf{k}$ and then inverted: $j(\mathbf{k},\omega) = \frac{1}{g(\mathbf{k},\omega)}$.

In this section, we learned how to effectively access the Admittance Band structure of systems by drawing analogies between circuit and solid-state models. However, relying solely on this procedure makes it challenging to identify discrepancies between the circuit results and the theoretical results. Differences in the band structure may stem from various sources, and a subset of these sources might yield identical effects. The next subsection delves into the discussion of detecting potential errors, such as incorrect connections, missing components,

or elements not operating as expected.

2.3.1. Debugging with the grounded Laplacian

In the final section, the chapter addresses the detection and resolution of discrepancies that may arise in the circuits behavior compared to the theoretical results. By examining the grounded Laplacian matrix, researchers can systematically identify issues such as disconnected elements, faulty grounding connections, improper circuit element selection, missing boundary terms and many others.

One effective method for identifying these discrepancies involves examining the grounded Laplacian matrix of the circuit $J(\mathbf{R})$. By measuring the complete G matrix and computing $J(\mathbf{R})$ as the inverse of $G(\mathbf{R})$, valuable information can be gained regarding any errors or deviations between the circuits band structure via direct comparison with theoretical Hamiltonian. Although the measurement of the complete G matrix and subsequent computation of $J(\mathbf{R})$ can be computationally demanding, this approach allows for a comprehensive assessment of the circuits behavior, enabling the detection of issues.

Moreover, measuring these discrepancies can reveal the potential effects of such deviations in a solid system. Additionally, studying these undesired terms can lead to the exploration of new phenomena and a deeper understanding of the underlying behavior. Thus, while initially unintended, these deviations in circuit behavior can uncover intriguing and previously unexplored phenomena in solid-state systems.

To illustrate this procedure, a circuit was designed in LTSpice[1] to emulate a small Haldane model. The circuit had a width of 4 unit cells in the confined direction and 10 unit cells in the periodic direction, as shown in Figure 2.3a). In Figure 2.3b), the band structure of the circuit is overlapped with a theoretical computation of the model with the same width. However, it is evident that the two bands closest to 0 do not match near $k = \pi$. To investigate this discrepancy, the grounded Laplacian matrix, denoted as J, was measured.

Figure 2.3c) illustrates the imaginary part of the grounded Laplacian, which differs from the real part of the Numerical Hamiltonian by a factor of 10^{-5}. It can be assumed that they are practically equal. However, the problem becomes more apparent when comparing the real part of J with the imaginary part of H in 2.3d), as there are noticeable differences between J and H. Based on the indexing used in these calculations, it is known that these matrix elements correspond to connections between next nearest neighbor (NNN) nodes, specifically on the boundary of the circuit. This can be visualized in Figure 2.3a), where missing connections are clearly visible between NNN B nodes (pink dotted box) on the top boundary and A (green dotted box) on the bottom boundary.

2.3.2. Two point impedance: detection of boundary modes

Before delving into the time evolution of voltages within our circuits, let's equip ourselves with a powerful tool capable of predicting the presence of edge states beforehand: the two-point impedance, denoted as $Z_{ab} = (V_a - V_b)/I$ between nodes a and b [57]. here $V_a - V_b$ is the voltage difference between the nodes and I es the magnitude of the current that enters one node and leaves the other. It is worth noting that this differs from the calculation in eq. 2.8, where measurements are referenced to ground (V_0). To determine Z_{ab} is necessary to express the potentials V_i in terms of the input current, elegantly employing the circuit

[1] Webpage of the SPICE simulator of choice. https://ltspice-simulator

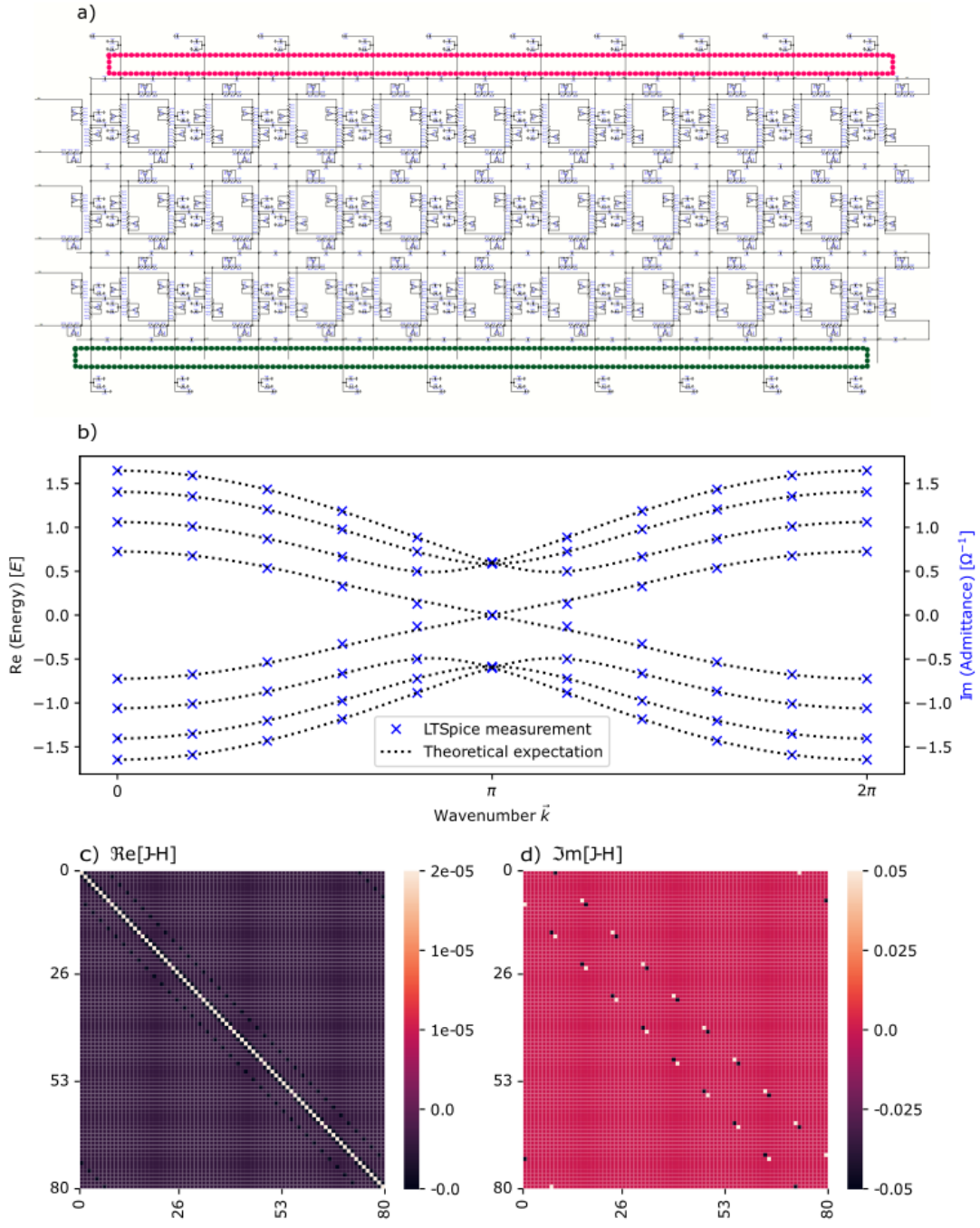

Figure 2.3: **a)** Electrical circuit intended to emulate a Haldane model ribbon of 4×10 unit cells with periodic boundary conditions, pink and green dotted boxes highlight the connections missing. **b)** Band structure obtained from the circuit in a) (blue crosses) compared to the theoretical result (dashed lines), **c), d)** Difference between the Laplacian J obtained from the same circuit and the Hamiltonian of the theoretical model.

Green's function G. This yields the following expression for the two-point impedance [66]:

$$Z_{ab} = \sum_{i=a,b} \frac{G_{ai} I_i - G_{bi} I_i}{I} = G_{aa} + G_{bb} - G_{ab} - G_{ba} = \sum_{j_n \neq 0} \frac{|\psi_{n,a} - \psi_{n,b}|^2}{j_n}. \tag{2.11}$$

This equation says that the impedance for each mode n depends on the squared magnitude of the potential difference between the two nodes involved, weighted by its eigen-impedance j_n^{-1}. As stated before, in the context of this work we consider only circuits made up of periodic sub-lattices, and since Bloch's theorem bless us with the momentum and band index one can simplify the eigenstates for the last formula $\psi_{\mathbf{k},m}(\mathbf{R},\alpha) = \varphi_m(\mathbf{k},\alpha)e^{i\mathbf{k}\cdot\mathbf{R}}$, this yields a refined impedance formula:

$$Z_{\mathbf{R}}^{\alpha\beta} = \sum_{\mathbf{k},m} \frac{|\varphi_m(\mathbf{k},\alpha) - \varphi_m(\mathbf{k},\beta)e^{i\mathbf{k}\cdot\mathbf{R}}|^2}{j_{\mathbf{k},m}}, \tag{2.12}$$

it can become large for a finite density of nontrivial eigenstates with small $j_{\mathbf{k},m}$. These impedance divergences, akin to resonances in RLC circuits, amplify even further when eigenstates find themselves localized within specific regions—a hallmark of edge states.

Essentially, the presence of a localized state within the circuit is due to a significant impediment to the flow of current and voltage. This obstruction manifests as a substantial rise in Z_{ab}, providing a strong indication of the existence of edge states. As mentioned at the beginning of this subsection, this tool allow us to detect the edge states before by not performing any time-dependent measurement, also this is the conventional tool used in the current literature to express the existence of edge states as shown for the work of [57] for the Topological Boundary Resonance (TBR).

2.4. Probing the Dynamics: Unveiling Time-Dependent Behavior

While the previous section explored extracting information through admittance band structure measurements, we shift our focus to time-dependent observations. We study the dynamic behavior of the system by observing the evolution of an excitation through the voltage profile. In solid-state physics, this approach would be analogous to directly observing the electronic wavefunction in the lattice, a feat currently beyond our reach.

However, by observing the voltage profile's temporal evolution, we can gain valuable information about the dynamics of the circuit and its topological properties. This exploration will provide a complementary perspective to the static study captured by the band structure analysis and more importantly it would allow us to observe the edge states that we are looking for directly.

2.4.1. Equations of motion

To delve into the circuit's temporal evolution, we must first establish its equations of motion. These equations, as eloquently detailed by Hofmann et al. (2019)[56], express the relationships between currents, voltages, and their time derivatives within the system:

$$\frac{d}{dt}\mathbf{I}(t) = C\frac{d^2}{dt^2}\mathbf{V}(t) + \Sigma\frac{d}{dt}\mathbf{V}(t) + L\mathbf{V}(t). \tag{2.13}$$

Where:

- $\mathbf{I}(t)$: N-component vector representing input currents,
- $\mathbf{V}(t)$: N-component vector representing node voltages against ground,

- C, Σ, L: Real-valued $(N \times N)$ matrices representing capacitance, conductance, and inductance, respectively.

These components collectively form the grounded circuit Laplacian [57] as

$$J(\omega) = i\omega C + \Sigma + \frac{1}{i\omega} L. \tag{2.14}$$

Focusing on the homogeneous case ($\mathbf{I} = 0$), we can recast the equation of motion into $2N$ first-order differential equations utilizing voltages and their first-time derivatives as independent variables. This transformation introduces the Hamiltonian matrix, H:

$$-i\frac{d}{dt}\psi(t) = H\psi(t), \tag{2.15}$$

here $\psi(t) = (\dot{\mathbf{V}}(t), \mathbf{V}(t))^\top$, encompassing both voltage and its derivative, and H emerges as a $(2N \times 2N)$-Hamiltonian block matrix:

$$H = i\begin{pmatrix} C^{-1}\Sigma & C^{-1}L \\ -\mathbb{I} & 0 \end{pmatrix}, \tag{2.16}$$

with $\mathbb{I}$ the identity matrix.

2.4.2. Eigenfrequencies and Eigenstates: The Rhythm of Evolution

The Hamiltonian's eigenfrequencies, denoted as ω_m dictate the time evolution of its eigenstates $\psi_m = \psi_m e^{i\omega_m t}$. These frequencies, linked to the admittance eigenvalues $j(\omega_m) = 0$, govern the circuit's resonance behavior.

As stated in [56], to ensure measurable real voltages and their time derivatives, these eigenfrequencies must come in pairs as $(\omega, -\omega^*)$, corresponding to complex conjugate pairs of eigenstates ψ, ψ^*. This leads to a natural pairing of eigenvalues as $\omega_n^{\pm}$, where $\omega_n^- = -(\omega_n^+)^*$ and $n \in \{1, ..., N\}$

The Hamiltonian's eigenvectors, crucial for comprehending its dynamics, can be constructed from the Laplacian's eigenvectors:

$$\psi_n^+ = \begin{pmatrix} i\omega_n^+ \mathbf{V}_n \\ \mathbf{V}_n \end{pmatrix}, \text{ and } \psi_n^- = \begin{pmatrix} i\omega_n^- \mathbf{V}_n^* \\ \mathbf{V}_n^* \end{pmatrix}. \tag{2.17}$$

Notably, for non-Hermitian Hamiltonians, the left eigenvectors might diverge from their right counterparts.

Having established the equations of motion and their connection to eigenstates, we are now equipped to explore the dynamics of the circuit directly through the voltage profile. This profile serves as a window into the system's eigenstates, revealing it's characteristics . In the next section, we will discuss the excitation methods done in this work for general circuits, allowing us to probe their dynamics.

2.4.3. Exciting! discussion on time dependent voltage excitation

In an experiment or, as in our case, a numerical simulation, we need to apply an external voltage source to a circuit to conduct a transient analysis. This leads to the question: What

type of voltage source can help us extract useful information from the system? And where in the circuit is the most convenient place to connect this source? With various possibilities available, which source will be the most effective? And where should we inject its energy to reveal the most informative responses?

Our toolbox offers a range of voltage source options, each with unique capabilities. The sinusoidal source allows us to examine the system at specific frequencies, providing a clear frequency probe. Pulse and step functions deliver abrupt changes, which is ideal for studying transient responses. For a broader perspective, complex waveforms like chirps or periodic sweeps offer a comprehensive view of the system's behavior across various frequencies. Each choice, however, has its strengths and limitations, so careful consideration is required.

This work employed two distinct voltage signals, each tailored to illuminate specific aspects of the circuit's behavior:

1. Sinusoidal Waves: These waves served as precise frequency probes, used both at resonant and off-resonant frequencies. By analyzing the circuit's response in and out of resonance, we gained insights into its stationary voltage patterns and its behavior at key frequencies.

2. Gaussian Pulses: As shown in Figure 2.4, these pulses delivered targeted bursts of energy, ideal for studying propagation characteristics. By observing how voltage signals moved through the circuit following a pulse injection, we could visualize its internal conductive pathways.

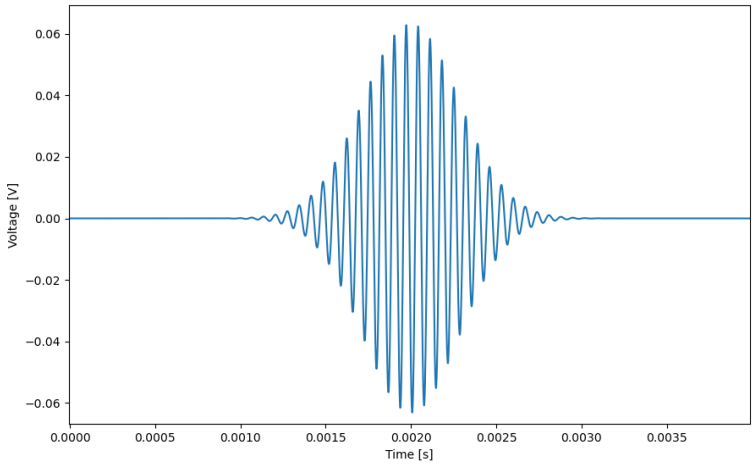

Figure 2.4: Typical Gaussian voltage profile of the external voltage source used to excite our circuits

The placement of these voltage sources was carefully chosen to align with the desired information:

- Edge State Investigation: To explore the edge states, the source was positioned at a circuit boundary, where these states are expected to be localized.

- Propagation Visualization: To unravel the voltage propagation, the pulse source was connected to various nodes, both within the bulk and at the edges. This diversified placement allowed us to observe the spatial and temporal evolution of voltage across the circuit's network.

By employing these diverse voltage signals and strategic placements, we aim to gain comprehensive information on the dynamic behavior of the circuit.

It is worth mentioning that Gaussian pulses can limit data analysis, mainly when the propagation time across an edge is similar to the pulse duration. This can lead to interference in the voltage signals and potentially obscure the propagation analysis. Additionally, due to the small size of the circuits studied in this work, the study of pulse propagation under periodic boundary conditions was limited to a single circuit traversal. In other words, the focus was observing the initial wavefront movement within a single cycle of the circuit.

Chapter 3

Results

Having established the theoretical framework of Laplacian theory and measurement techniques in the previous Chapter, we now present our investigation – the exploration of topological phenomena in a selection of model circuits. This section presents the design and measured band structures of four distinct topolectrical models: the Su-Schrieffer-Heeger (SSH) model [29], the Haldane model [10], the Modified Haldane model [2], adding some effects of real components to finish with a non-reciprocal SSH model [4] to demonstrate how this circuits serve as a bridge, not just to observe new topological models, but also to venture into the fascinating realm of non-Hermiticity. We will then dissect their topological properties through the lens of their Laplacians, visualize the edge states, and finally, observe the propagation of wave packets along these topologically protected states.

This investigation was made via numerical simulations using LTSpice[2], a free SPICE simulator software. The number of simulation that had to be done for this work was big enough to require automatization, this was implemented with Python using a library called PyLTSpice[3] that is specialized to run SPICE simulations.

3.1. Su–Schrieffer–Heeger model

Our initial focus was on a selection of well-established models to validate known results and establish a firm foundation for our subsequent analysis. Notably, the publication of T. Helbig et al. in 2019 (Phys. Rev. B 99, 161114) [58] served as a valuable guide for our early work.

Among these models, the Su-Schrieffer-Heeger (SSH) model held particular interest due to its well-documented topological properties, specifically the presence of edge states. Additionally, its one-dimensional nature made it simple enough as a starting point.

3.1.1. Circuit Implementation and Edge State Verification

The general idea of the SSH model relies on alternating single and double bonds in a one-dimensional molecule, translating to step-wise hopping probabilities. Figure 3.1**a** depicts the LTSpice implementation of this model, employing step-wise capacitors with values C_1 and C_2 as described in the caption. Focusing in the in and out current for a pair of nodes A

[2] Webpage of the SPICE simulator of choice. https://ltspice-simulator
[3] PyLTSpice is available on PyPi https://PyLTSpice.

and B in a j unit cell, the Kirchhoff equation of currents yields:

$$I_{Aj} = i\omega C_1(V_{Aj} - V_{Bj}) + i\omega C_2(V_{Aj} - V_{Bj-1}) + \frac{1}{i\omega L}(V_{Aj} - V_0), \tag{3.1}$$

$$I_{Bj} = i\omega C_1(V_{Bj} - V_{Aj}) + i\omega C_2(V_{Bj} - V_{Aj+1}) + \frac{1}{i\omega L}(V_{Bj} - V_0), \tag{3.2}$$

This yields to a set of equations for all the nodes that can be written down as:

$$\mathbf{I} = J_{SSH}\mathbf{V}, \tag{3.3}$$

where the matrix J_{SSH} gives:

$$J_{SSH} = \begin{pmatrix} i\omega(C_1+C_2)+\frac{1}{i\omega L} & -i\omega C_1 & 0 & 0 & 0 & \dots \\ -i\omega C_1 & i\omega(C_1+C_2)+\frac{1}{i\omega L} & -i\omega C_2 & 0 & 0 & \dots \\ 0 & -i\omega C_2 & i\omega(C_1+C_2)+\frac{1}{i\omega L} & -i\omega C_1 & 0 & \dots \\ 0 & 0 & -i\omega C_1 & i\omega(C_1+C_2)+\frac{1}{i\omega L} & -i\omega C_2 & \dots \\ \vdots & \vdots & \vdots & \vdots & \ddots & \end{pmatrix}$$

$$= i\omega C_2 \begin{pmatrix} (1+t)(1-\frac{\omega_0^2}{\omega^2}) & -t & 0 & 0 & 0 & \dots \\ -t & (1+t)(1-\frac{\omega_0^2}{\omega^2}) & -1 & 0 & 0 & \dots \\ 0 & -1 & (1+t)(1-\frac{\omega_0^2}{\omega^2}) & -t & 0 & \dots \\ 0 & 0 & -t & (1+t)(1-\frac{\omega_0^2}{\omega^2}) & -1 & \dots \\ \vdots & \vdots & \vdots & \vdots & \ddots & \end{pmatrix}, \tag{3.4}$$

here $\omega_0 = \frac{1}{\sqrt{L(C_1+C_2)}}$ is the resonant frequency. With this, imposing periodic boundary conditions and Fourier transforming eq.3.4 the momentum space representation of the grounded Laplacian is obtained

$$J_{SSH}(k) = i\omega(C_1 + C_2 - \frac{1}{\omega^2 L})\mathbb{I} - i\omega[(C_1 + C_2\cos(k))\sigma_x + C_2\sin(k)\sigma_y], \tag{3.5}$$

where $\{\sigma_i\}$ is the set of the Pauli matrices and $\mathbb{I}$ is the (2×2) identity matrix. For initial observations, eq.3.21, omitting the identity term, has the same structure as the one presented in eq.1.10 so this implementation should work for the analogy.

Our initial exploration focused on observing the edge voltage profile. As shown in Figure 3.1(b), exciting the system with a sinusoidal voltage source at the resonance frequency ω_0 applied to one edge yielded the expected result for the theoretical zero-energy eigenstate, $\psi_0(n) = (((-t)^n \mathrm{V}_0, 0)$. It is important to note that this measurement was conducted in the non-trivial phase of the system with $t < 1$.

3.1.1.1. Confirming the Non-Trivial Phase

Verifying the non-trivial phase was crucial, not only for interpreting the results but also for tuning the resonance frequency. This was achieved through a two-point impedance measurement, presented in Figure 3.1(c). As expected, a clear peak appears at the resonance frequency in the non-trivial phase. This aligns with the fact that admittance eigenvalues serve as an energy analog for circuits, and the presence of a zero-admittance mode translates to a

divergence in the two-node impedance, as discussed in the previous section and demonstrated by Cserti et al. (2011) [66].

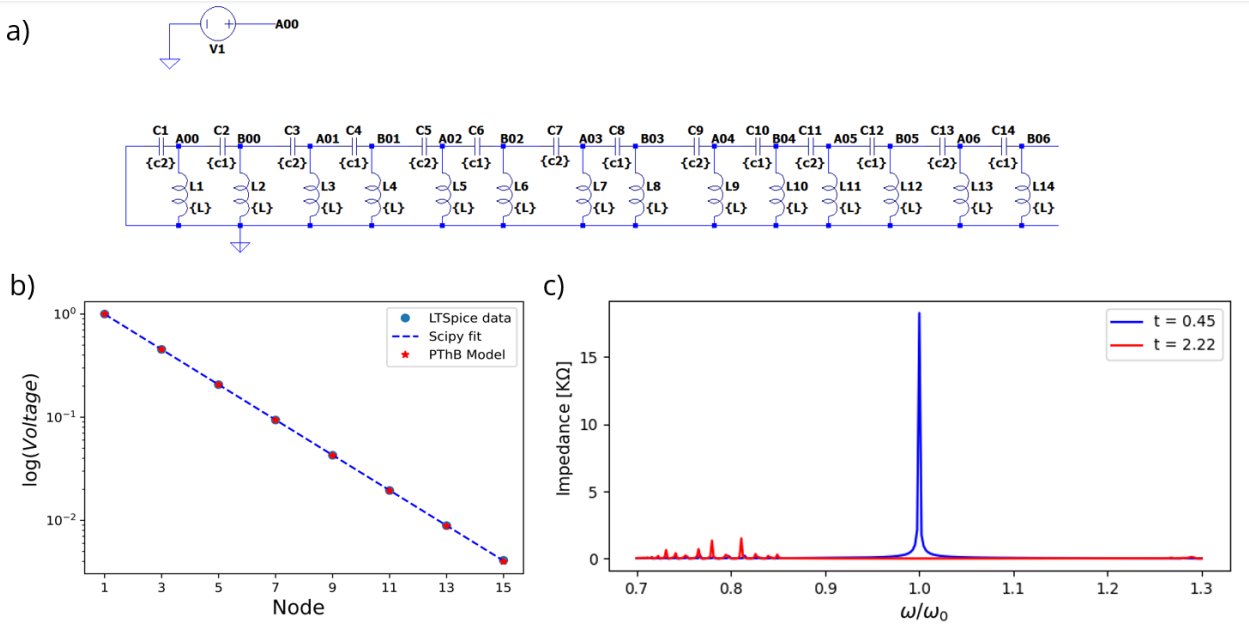

Figure 3.1: **a)** Su-Schrieffer–Heeger (SSH) scheme. Each unit cell has a pair of capacitors, C_1 and C_2, with identical grounded inductors L every two capacitors. An AC voltage source of amplitude V_0. With $t = C_1/C_2 < 1$ a characteristic 0 energy state can be found. This was implemented with LTSPice with parameters: $C_1 = 0.1\mu$F, $C_2 = 0.22\mu$F, L= 10μH y $V_0 = 1$V. The green lines indicate how to measure in the t^{-1} configuration in the same circuit. **b)** Simulated cero energy state $\psi_0(n)$ for the system described in **(a)**. This measurement matches with the theoretically expected state $\psi_0(n) = (((-t)^n V_0, 0)$, where n is the unit cell listed left to right, the same as the computed state using Python Tight-Binding.**c)** Two point impedance calculations for the configurations $t = 0.45$ y $t' = 2.2$. The non-trivial topological phase shows a peak of impedance in the middle of the gap, associated to the cero energy state, it can be noted that this behavior does not appear in the trivial phase t'.

The presented results are based on simulations using mostly idealized components, with the exception of the parameters required for calculations in LTSpice. In a real-world scenario with non-ideal components, it is expected that the two-point impedance measurement would exhibit a less sharp peak, as demonstrated by Lee et al. (2018) [57]. This deviation is due to factors such as component tolerances, parasitic, and inherent losses in physical systems.

3.1.2. Admittance band structure

To further strengthen the analogy between our circuit and the SSH model, and to definitively confirm that the observed edge states were not merely a fortuitous coincidence, we sought to directly visualize the band structure of the system. Following the procedure stated in the last section we excited all the nodes in the circuit with a sinusoidal voltage source in a AC analysis and then measured the voltages in all nodes with respect to ground and constructed the G matrix by the use of eq.2.8 tuning it near the resonance frequency

encountered in 3.1(c). Figure 3.2 summarizes our findings, showcasing the admittance band

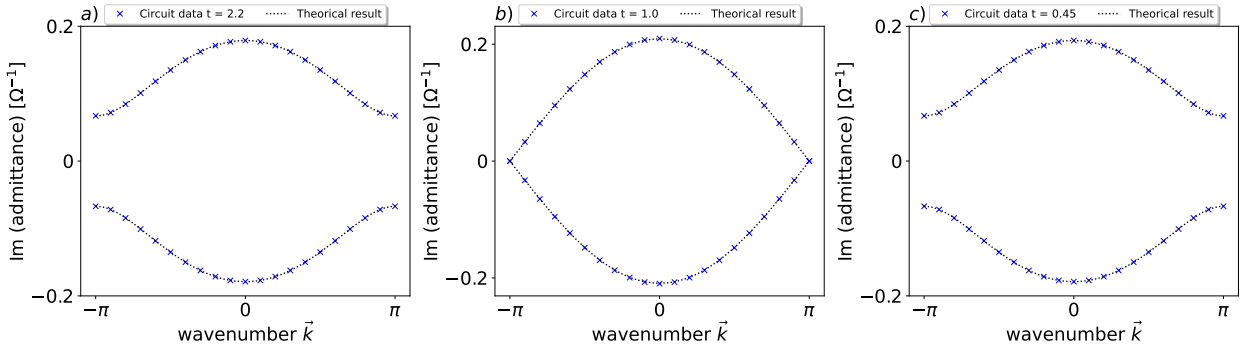

Figure 3.2: Simulated admittance band structure of the finite implemented circuit (blue crosses) with PBC compared with numerical calculation of its corresponding infinite SSH analog model (black dashed lines). **a)** $t' = C_2/C_1 = 2.22$ corresponding to the trivial phase. **b)** Phase transition limit by closing the gap in $t = 1$ and finally **c)** shows for $t = 0.45 = t\dot{t}^{-1} = (2.22)^{-1}$ in the topological phase.

structure calculated for three distinct sets of capacitance values between nodes: $C_1 = 0.1\mu$ F and $C_2 = 0.22\mu$ F. These capacitance values are arranged to achieve three pivotal values of t, representing the ratio between capacitors (analogous to hopping amplitudes in the system).

We looked to further validate the accuracy of our model by directly comparing its J matrix with the theoretical Hamiltonian, H. This comparison can be conducted in both position and momentum space, providing complementary perspectives. We focused on position space, aligning node indices to facilitate a direct subtraction of the measured J matrix from the theoretical H matrix of the corresponding model.

Figure 3.3 showcases the results of this operation. The color bar reveals a minuscule difference between the corresponding elements, significantly smaller than the overall matrix values. This alignment confirms that our circuit measurements mirror the theoretical tight-binding model.

Notably, in Figure 3.3(b) and 3.3(d), an imaginary diagonal term emerges in the measured J matrix. This term can be confidently attributed to parasitic resistances inherently introduced by LTspice to facilitate calculations. Its presence is therefore expected and does not undermine the validity of the overall agreement of the model with the theoretical Hamiltonian.

These results serve as a benchmark of the method at least for one-dimensional models. The next step is to go for two-dimensional models, as mentioned at the beginning of the chapter we are interested in honeycomb lattices so we implemented a Graphene model to start the two-dimensional studies

3.2. Graphene model

To initiate our exploration of two-dimensional systems, we constructed a circuit model of graphene, guided by Hofmann et al. (2019)[56]. The building block of the model consists of two nodes, A and B, connected by a capacitance C. Each node within a unit cell is connected to its counterparts in neighboring unit cells, also via capacitors C. This arrangement ensures that every node is connected with its three nearest neighbors through identical capacitors.

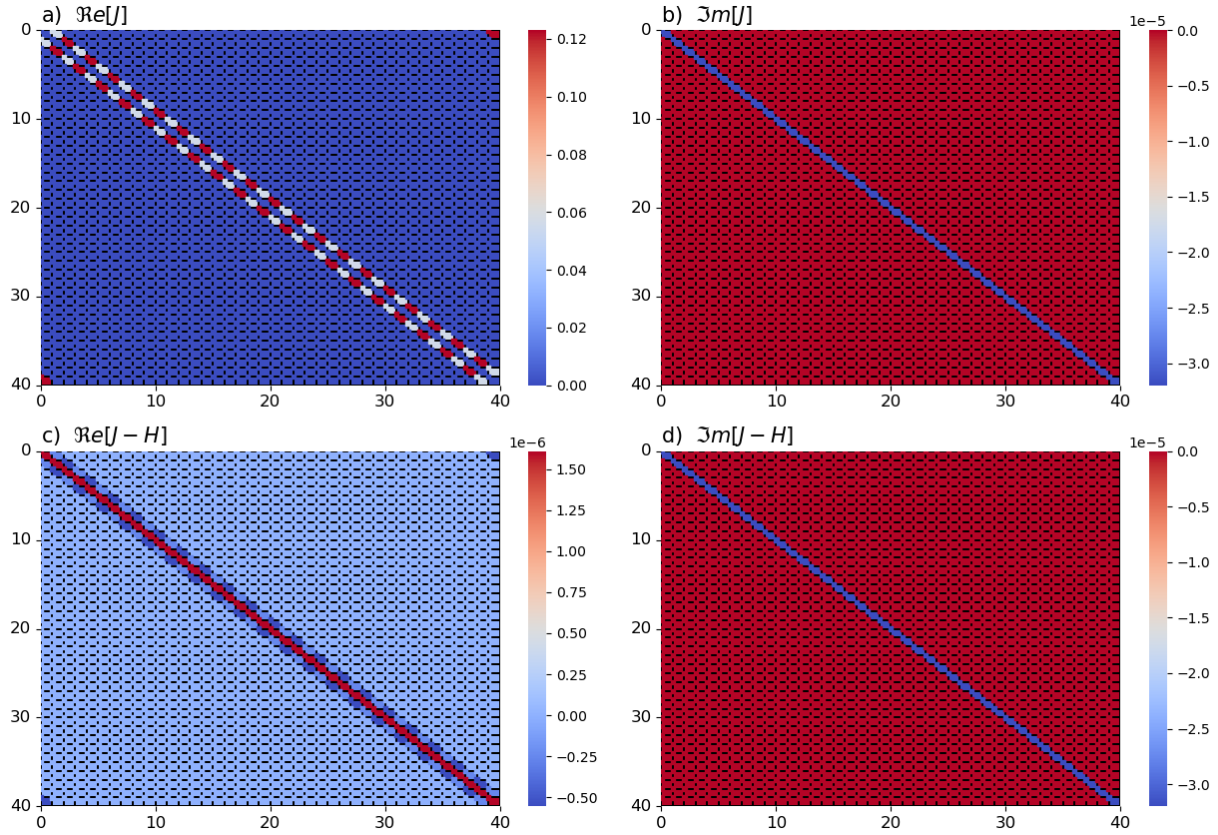

Figure 3.3: Comparison between the J matrix, computed from the circuit simulation, and the Hamiltonian H of the analog system for $t = 0.45$. While elements of J are measured in admittance ($[\Omega^{-1}]$), and those of H in energy ($[eV]$), the qualitative agreement between the matrices is evident.

Each node is grounded with an inductance $L_{g\alpha}$ and a capacitance $C_{g\alpha}$, this grounding could be different for each sub-lattice for the purpose of breaking inversion symmetry.

It is worth noticing that the physical arrangement of connections of this model deviates from the conventional hexagonal geometry of honeycomb lattice. However, this difference does not obstruct the accuracy the model in capturing the electronic characteristics of graphene. As discussed in chapter 2, the governing equations of our circuit rely just on the connectivity scheme of the network, leaving the geometric arrangement as a gauge freedom. This is thanks to the graph nature of the framework, which prioritizes connections over the physical distribution of nodes, as depicted in Figure 3.4.

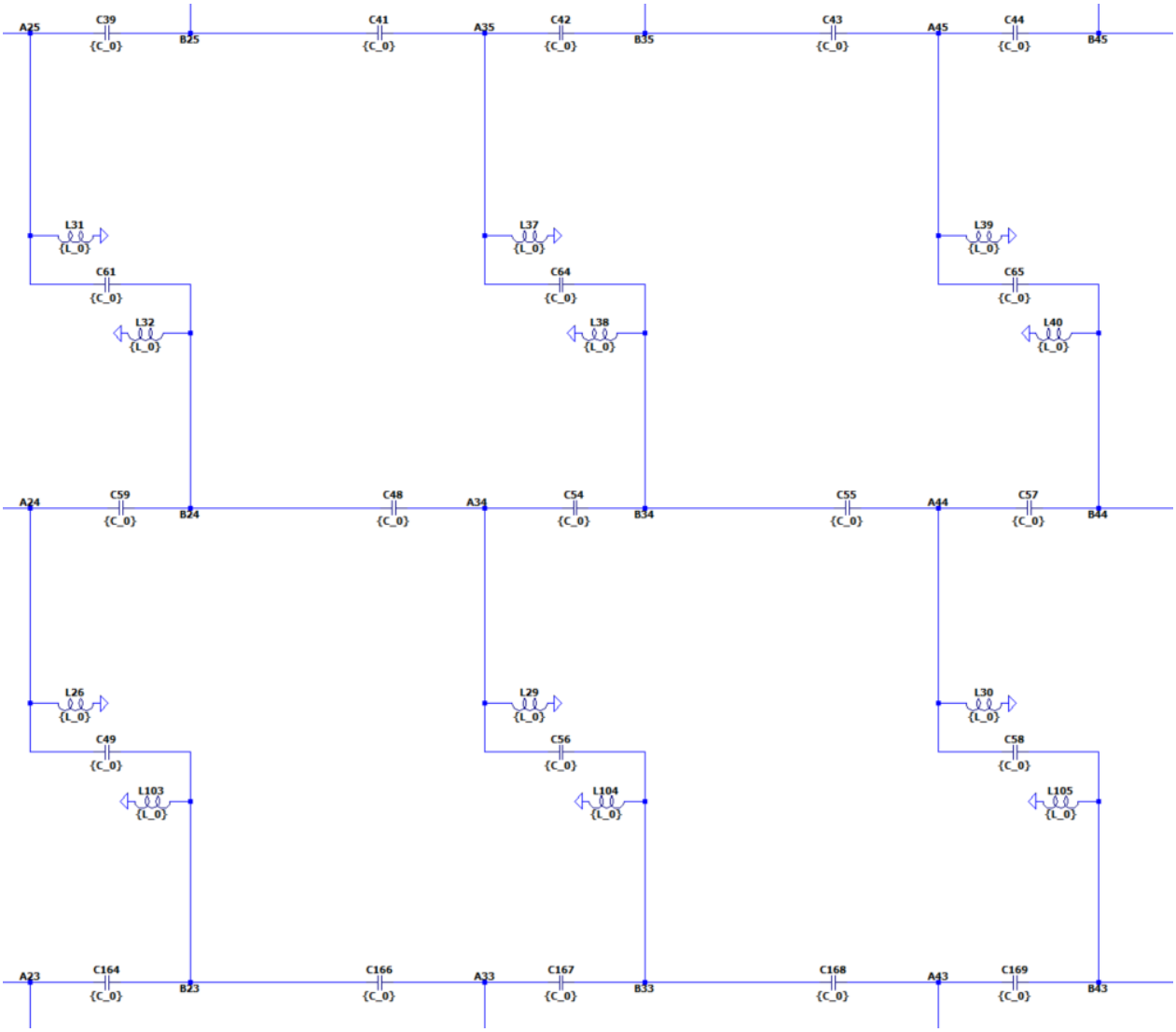

Figure 3.4: Circuit implementation of the graphene model for the bulk. The central unit cell consists of two nodes, labeled $A34$ and $B34$, connected to their nearest neighbors via C_0 capacitors.

For this implementation, writing the currents for a pair of nodes A and B in a j unit cell the equations yields to:

$$I_{Aj} = i\omega C(V_{Aj} - V_{Bj}) + i\omega C(V_{Aj} - V_{Bj-1}) + i\omega C(V_{Aj} - V_{Bj-2}) + \left[i\omega C_{gA} + \frac{1}{i\omega L_{gA}}\right](V_{Aj} - V_0), \tag{3.6}$$

$$I_{Bj} = i\omega C(V_{Bj} - V_{Aj}) + i\omega C(V_{Bj} - V_{Aj+1}) + i\omega C(V_{Bj} - V_{Aj+2}) + \left[i\omega C_{gB} + \frac{1}{i\omega L_{gB}}\right](V_{Bj} - V_0). \tag{3.7}$$

Considering the equations for all nodes in the circuits, the last equation can be written in matrix form:

$$\mathbf{I} = J_{Graph}\mathbf{V}, \tag{3.8}$$

where J_{Graph} is the grounded Laplacian of the system. Imposing periodic conditions and Fourier transforming J_{Graph} lead us to the momentum space representation

$$J_{Graph} = i\omega \left[\left(3C - \frac{1}{\omega^2 L} \right) \mathbb{I} - C(1 + \cos k_x + \cos k_y)\sigma_x - C(\sin k_x + \sin k_y)\sigma_y \right]. \tag{3.9}$$

As we are using the graphene model as a basis for the following systems, we study the band structure due to its importance in two-dimensions. Our focus is on ribbon geometry (semi-1D) to study edge states and excitation propagation, with this geometry k is just a number but node indexing takes a more important role for our calculations, we managed it by using the notation for G and J from chapter 2 as we will explain.

Computing G matrix of the ribbon $G_{\alpha,\beta}(\mathbf{k})$ now requires a larger unit cell due to the increased width. Consequently, α and β indices represent all nodes within this extended cell. To apply Eq.2.10, we sum all unit cell components along the periodic dimension, resulting in a $(2M \times 2M)$ matrix (M being the width). If we recall from the SSH model, G changes from a (2×2) matrix to a bigger dimension, this shows the importance of proper node indexing while building G from Eq.2.8. We adopted the indexing scheme from the PythTB[4] library to ensure consistency.

Figure 3.5 depicts the ribbon band structure obtained for a simplified graphene-like circuit of 20 unit cells width and also 20 unit cells in the periodic dimension with the specified parameters. The results from the circuit simulation (blue crosses) closely align with the band structure of the corresponding solid system (dashed curve) for the same parameters. This agreement validates the circuit model as a suitable analog for the graphene tight-binding Hamiltonian.

Figure 3.6 examines the measured J matrix and its difference from the theoretical Hamiltonian H. Notably, the scale of these discrepancies is significantly smaller than the overall magnitude of the matrix elements. This minimal difference validates the design of the circuit as an analog for the graphene tight-binding Hamiltonian. As anticipated, an imaginary diagonal term emerges in the J matrix. This component, similar to the SSH model in Figure 3.3, can be attributed to the parasitic resistances inherently introduced by LTspice during simulations.

Having established the graphene model as a stepping stone for two-dimensional honeycomb systems, we embark on a journey to replicate known edge states and study new phenomena. Two distinct directions guide our exploration:

- Our first objective is to incorporate topological effects into our framework. This begins with tackling the well known Haldane model, an example of a topologically non-trivial system exhibiting robust edge states.
- Next, we explore the Colomés and Franz model [2]. This model, currently lacking a simple experimental realization, presents a unique opportunity to show our circuit methodology as a powerful tool for theoretical exploration.

3.3. Haldane model

A key advantage of employing electrical circuits as simulators lies in their direct access to the wave function and its time evolution. Considering this, and aligning with the focus

[4] PythTB is available on PyPi https://PythTB

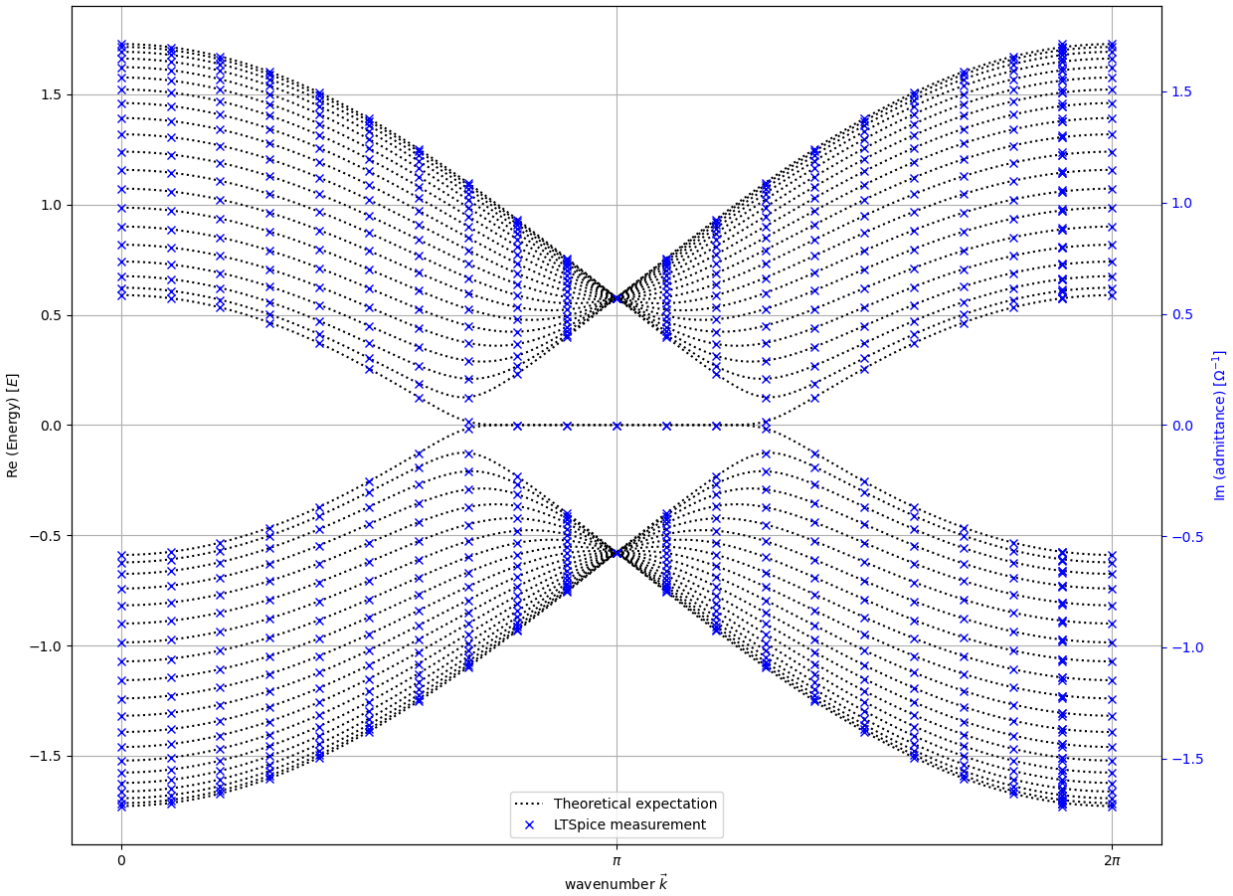

Figure 3.5: Measured admittance band structure of the implemented circuit (blue crosses) with $\omega \approx \omega_0$, $C = 10\mu$F and $L = 10\mu$H contrasted with the energy band structure of the corresponding tight binding model (dashed lines).

of the project, we aim to utilize this platform for the direct observation of edge states, both topologically protected (as demonstrated with SSH) and non-protected. In this section we study the model proposed by D. Haldane in 1988 [10], from now on the Haldane model.

Our exploration goes in four stages: **1.-** Designing the circuit. **2.-** Band Structure Analysis, highlighting the differences between the grounded Laplacian and the Hamiltonian. **3.-** Direct Observation of Edge States via voltage measurements. **4.-** Incorporating Real-World Elements.

We seek to not only replicate the known phenomena of edge states but also uncover their dynamics and interactions within the framework of circuit simulations. This pursuit aligns with this thesis objective of bridging between theoretical models and experimental realizations of topological quantum materials using electrical circuits as platform.

3.3.1. Circuit design

Building upon the description of the Haldane model introduced in Chapter 1, we now focus on translating its connectivity pattern into our circuit. As a reminder, the model features a honeycomb lattice where each site interacts with its nearest neighbors via a hopping amplitude t_1 and, crucially, with its next-nearest neighbors (NNN) through a complex hopping

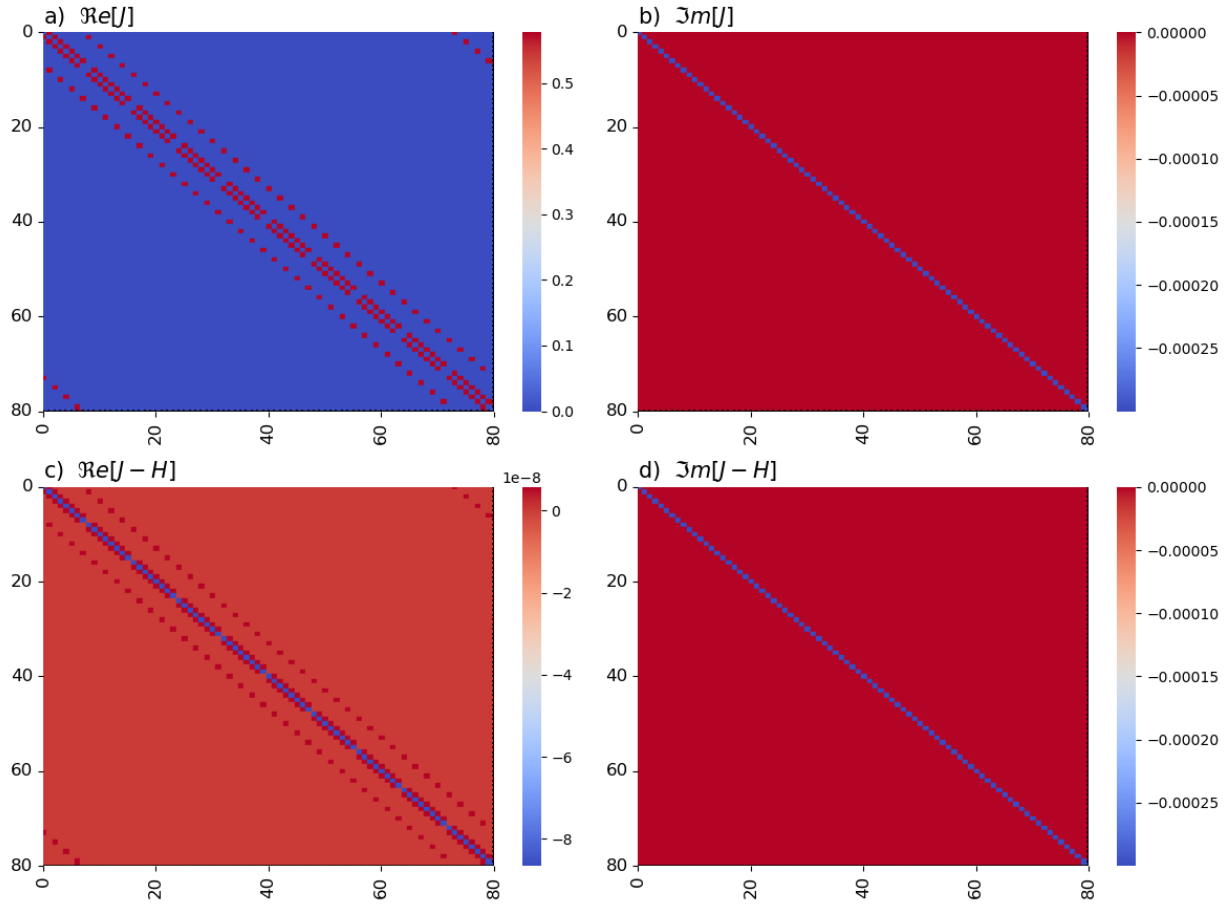

Figure 3.6: Comparison between the J matrix, computed from the circuit simulation ($\omega \approx \omega_0$, $C = 10\mu$F and $L = 10\mu$H), and the Hamiltonian H of the analog system for $t = 0.57$. While elements of J are measured in admittance ($[\Omega^{-1}]$), and those of H in energy ($[eV]$), the qualitative agreement between the matrices is evident.

$t_2 e^{i\phi}$. This complex term, with its specific phase rule depicted in Figure 1.10, plays a vital role in topological properties of the model.

To accurately replicate this NNN connection, we use the description from Chapter 2 and draw inspiration from the work of Hofmann et al. (2019) [56]. Their proposed Impedance Converter with Current Inversion (INIC) configuration suits our needs, described by Eq. 2.7. This element allows us to tune the phase of the hopping amplitude via proportion between R_a and R_b, and achieve non-reciprocity, ensuring that the hopping amplitude from site $A(B)$ to $A(B)$ differs from that for the reverse path. Figure 3.7 showcases the circuit designed to simulate the bulk of the Haldane model.

For this implementation, writing the currents for a pair of nodes A and B in a j unit cell

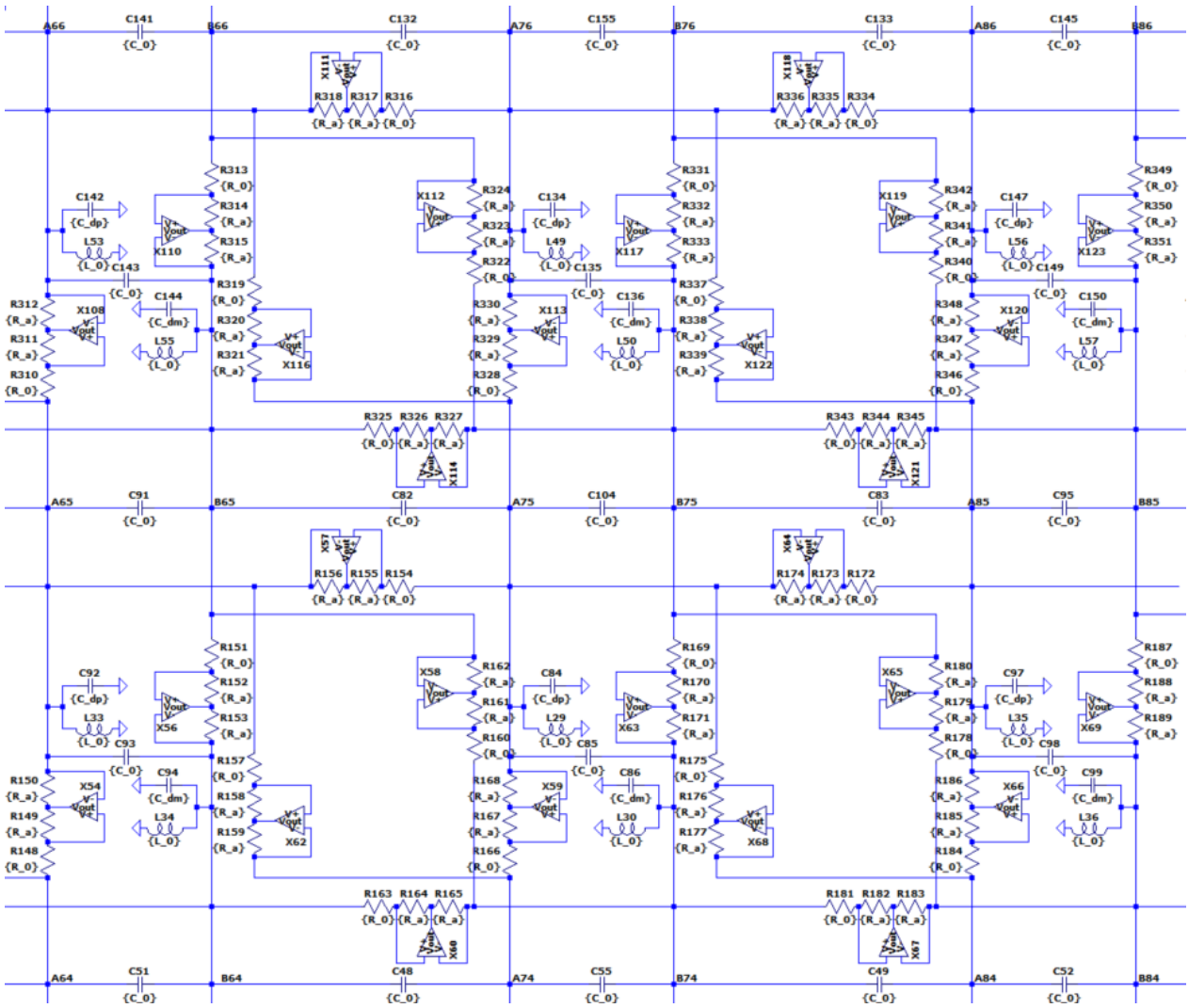

Figure 3.7: Zooming in on the bulk for the implementation of the Haldane model circuit, centered at unit cell 75 with nodes $A75$ and $B75$ exemplify the connections: Capacitors C_0 to NN, while INICs controlled by absolute resistance R_0 bridge the gap between next-nearest neighbors across sub-lattices. Each node is grounded with inductors L_0 and sub-lattice-specific capacitors (C_{dp} for A, C_{dm} for B), Although currently set to zero for simplicity, these sub-lattice capacitors hold the potential to break inversion symmetry, acting as a Semenoff mass [67].

and using the notation presented the first chapter, the Kirchhoff equations yields to:

$$
\begin{aligned}
I_{Aj} = {} & i\omega C_0\big(V_{Aj} - V_{Bj}\big) + i\omega C_0\big(V_{Aj} - V_{Bj-1}\big) + i\omega C_0\big(V_{Aj} - V_{Bj-2}\big) + \left[i\omega C_{dp} + \frac{1}{i\omega L_0}\right]\big(V_{Aj} - V_0\big) \\
& + \frac{1}{R_0}\big(V_{Aj} - V_{Aj-1}\big) + \frac{-1}{R_0}\big(V_{Aj} - V_{Aj-2}\big) + \frac{1}{R_0}\big(V_{Aj} - V_{Aj-3}\big) + \frac{-1}{R_0}\big(V_{Aj} - V_{Aj+1}\big) + \frac{1}{R_0}\big(V_{Aj} - V_{Aj+2}\big) \\
& + \frac{-1}{R_0}\big(V_{Aj} - V_{Aj+3}\big), \qquad (3.10)
\end{aligned}
$$

$$I_{Bj} = i\omega C_0\Big(V_{Bj} - V_{Aj}\Big) + i\omega C_0\Big(V_{Bj} - V_{Aj+1}\Big) + i\omega C_0\Big(V_{Bj} - V_{Aj+2}\Big) + \left[i\omega C_{dm} + \frac{1}{i\omega L_0}\right]\Big(V_{Bj} - V_0\Big)$$
$$+\frac{-1}{R_0}\Big(V_{Bj} - V_{Bj-1}\Big) + \frac{1}{R_0}\Big(V_{Bj} - V_{Bj-2}\Big) + \frac{-1}{R_0}\Big(V_{Bj} - V_{Bj-3}\Big) + \frac{1}{R_0}\Big(V_{Bj} - V_{Bj+1}\Big) + \frac{-1}{R_0}\Big(V_{Bj} - V_{Bj+2}\Big)$$
$$+\frac{1}{R_0}\Big(V_{Bj} - V_{Bj+3}\Big), \tag{3.11}$$

where $R_a = R_b = 1$ so it give us a phase of $\phi = \pi/2$ so all resistances are pure real numbers. Considering the equations for all nodes in the circuit, the last equation can be written in matrix form:

$$\mathbf{I} = J_{Hald}\mathbf{V}, \tag{3.12}$$

where J_{Hald} is the grounded Laplacian of the system in position representation. Imposing periodic conditions and Fourier transforming J_{Hald} lead us to the momentum space representation

$$J_{Hald} = i\omega\Bigg[\left(3C_0 + \frac{C_{dp} + C_{dm}}{2} - \frac{1}{\omega^2 L_0}\right)\mathbb{I} - C_0\Big(1 + \cos(k_x) + \cos(k_y)\Big)\sigma_x - C_0\Big(\sin(k_x) + \sin(k_y)\Big)\sigma_y$$
$$+\left(\frac{C_{dp} - C_{dm}}{2} + \frac{2}{\omega R_0}\Big(\sin(k_x) - \sin(k_y) - \sin(k_x - k_y)\Big)\right)\sigma_z\Bigg], \tag{3.13}$$

successfully replicating the structure of the Haldane model Hamiltonian 1.30 with $\phi = \pi/2$. The incorporation of INICs produces the desired effect within the J_{Hald} matrix, introducing a component proportional to σ_z that complements the original graphene-like J_{Graph}. Additionally, grounding capacitors effectively simulate the Semenoff mass component. As discussed in [10] is the interplay between this parameters what governs the topological phase diagram. To ensure our subsequent calculations reside within the topological phase, we strategically set $C_{dp} = C_{dp} = 0$ alongside with $\phi = \pi/2$.

3.3.2. Band Structure analysis

In the following we use a ribbon geometry with zig-zag terminations. To maintain the desired connectivity pattern, all missing nearest-neighbor (NN) connections were grounded with their corresponding capacitors C_0 at the boundaries.

Following the approach established in the graphene Section 3.2, we computed the conductance matrix G for the ribbon geometry. Implementing periodic boundary conditions and employing the measuring protocol, we obtained the admittance band structure. These results are visually in Figures 3.8 and 3.9, showcasing the band structure and J matrix, respectively.

Figure 3.8 shows the ribbon band structure obtained for a circuit of 10 unit cells width and also 10 unit cells in the periodic dimension with the specified parameters. Our results from the circuit simulation (blue crosses) align with the band structure of the corresponding solid system (dashed curve) for the same parameters.

Figure 3.9 shows the measured J matrix and its difference from the theoretical Hamiltonian H. The scale of these differences is smaller than the overall magnitude of the matrix elements. As anticipated, an imaginary diagonal term emerges in the J matrix. This component, similar to the SSH model in Figure 3.3, can be attributed to the parasitic resistances inherently introduced by LTspice during simulations. Also, the imaginary part of J shows that our NNN connections resulted as non-reciprocal terms since the symmetrical terms are of opposite

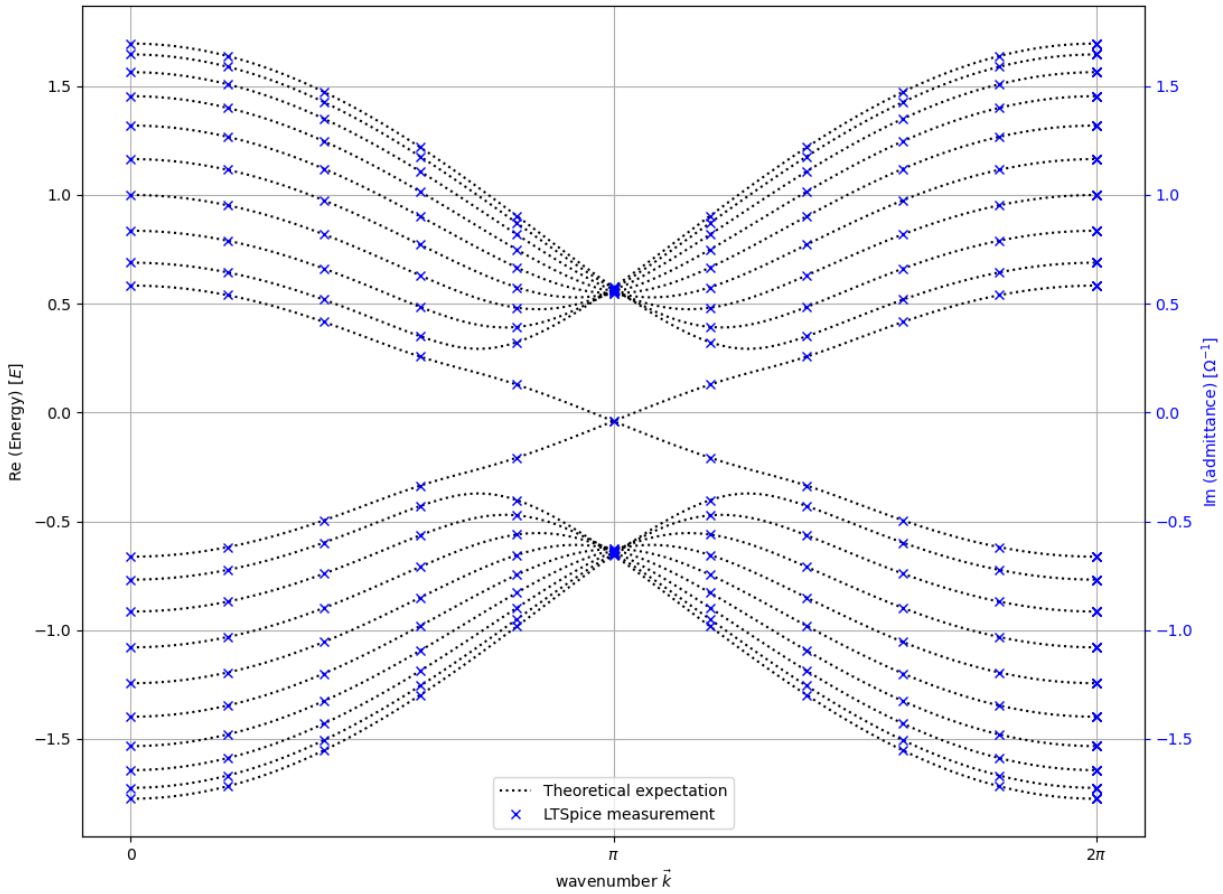

Figure 3.8: Measured admittance band structure of the implemented Haldane circuit (blue crosses) with $\omega \approx w_0$, $C_0 = 10\mu$F, $L_0 = 10\mu$H and $R = 20\Omega$ contrasted with the band structure of the corresponding tight binding model (dashed lines).

signs, thus emulating the nature of the Haldane complex hopping.

3.3.3. Observation of edge states

Having constructed a circuit that mirrors the Haldane Hamiltonian, we now want to directly observe its edge states. This begins by exciting the circuit and analyzing its response. The Haldane model is renowned for presenting topologically protected chiral edge states, which are predicted to emerge within the non-trivial topological phase. Thus, we aim to verify whether our circuit, tuned to reside within this phase, will exhibit these states.

In chapter 2 we discussed the diverse techniques for circuit excitation. Here, we opt for a pulse excitation scheme to probe the edge state dynamics. Figure 3.10 shows the results obtained from applying a pulse excitation to various nodes within the circuit.

Figures 3.10(a) and (b) provide show the presence of topologically protected chiral edge states within our circuit model. As predicted by the Haldane model, the applied pulse excitation remains confined to the designated edge, exhibiting little to no leakage into the bulk. Also, the excitation propagates along each edge in opposite directions. This observed behavior aligns with the theoretical expectations of chiral edge states within the Haldane model. A bulk injection give us a drastically different response as shown in Figure 3.10c)

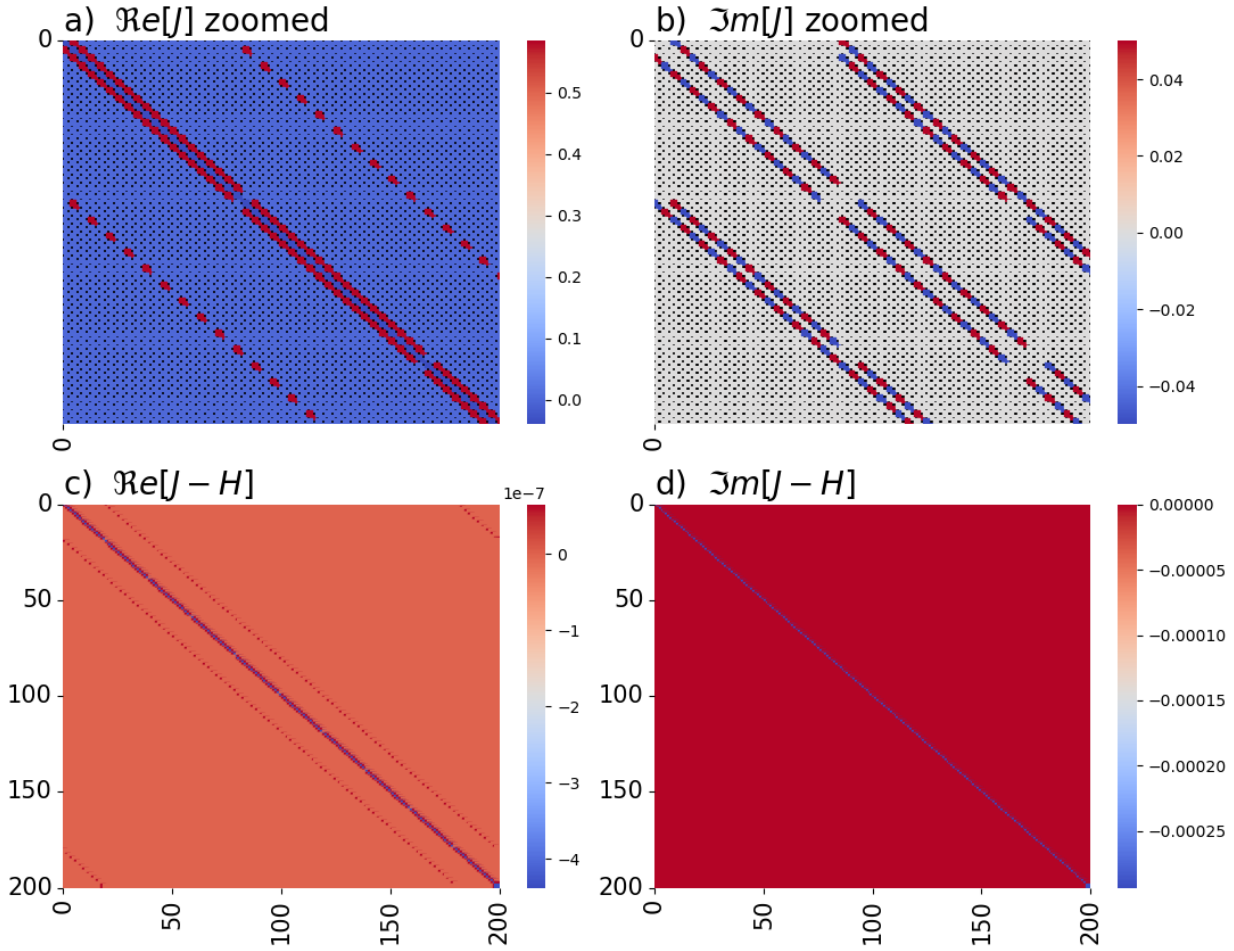

Figure 3.9: Zoomed J matrix in a) and b) showing the structure of the resulting connections. In c) and d) is the comparison between the J matrix, computed from the circuit simulation (same parameters as in 3.8), and the Hamiltonian H of the analog system for $t_1 = 0.58$, $t_2 = 0.05$ and $\phi = \pi/2$. While elements of J are measured in admittance ($[\Omega^{-1}]$), and those of H in energy ($[eV]$), the qualitative agreement between the matrices is evident.

where a localize voltage response is present.

However, it is important to acknowledge the presence of dissipation in the system. This is likely attributable to the parasitic resistances within the circuit components, as hinted at in Figure 3.9(d). These parasitic resistances introduce a finite imaginary component to the J matrix of the circuit, resulting in complex energy eigenvalues and consequently, some degree of dissipation. Also, as discussed in Chapter 2, thanks the grounding of the initial excitation node and the potential for interference for more than the first circuit cycle, we end up focusing on the initial wavefront for analysis. Exploring larger circuit sizes in the periodic dimension would allow to study the preservation of the wavefront in a more detailed manner, but the dissipation can also be well observed in 3.10d).

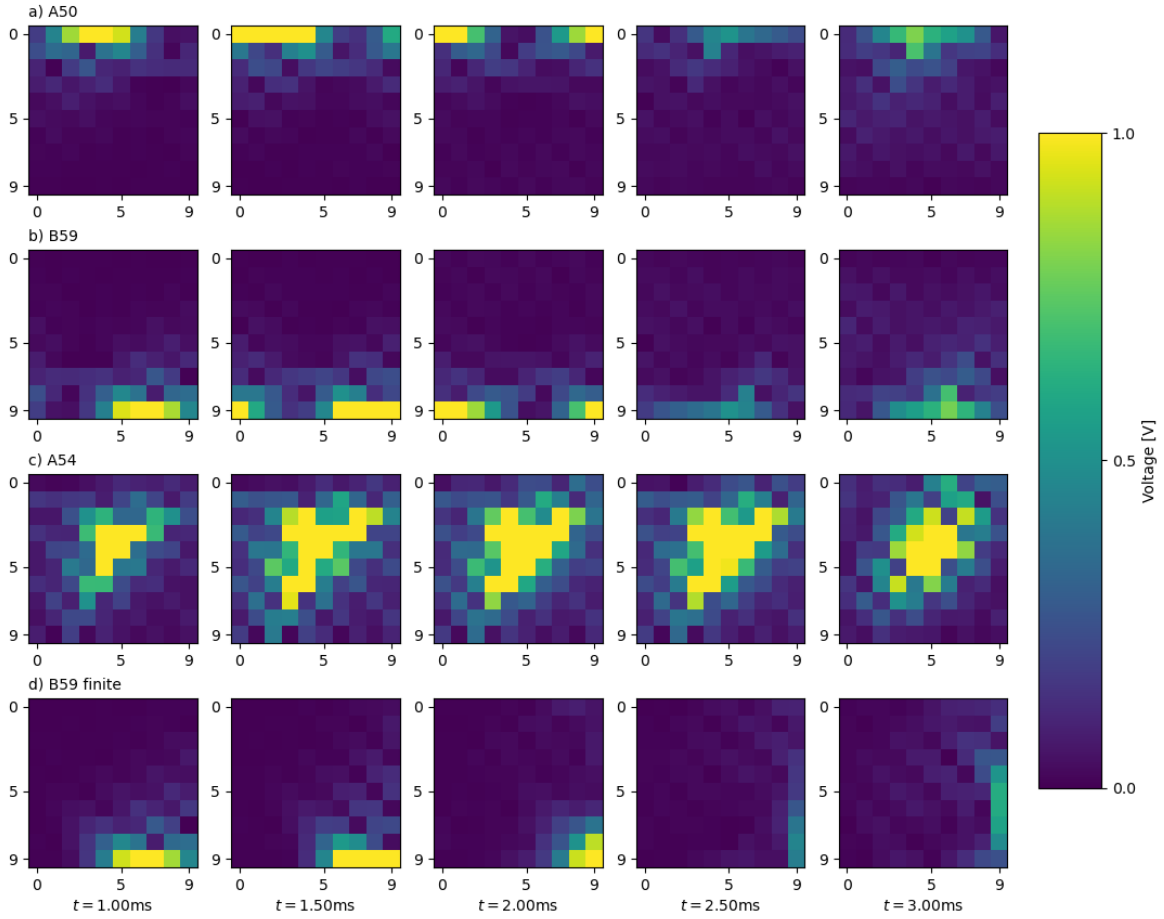

Figure 3.10: Time-resolved voltage signal per unit cell for a Gaussian pulse excitation in different nodes across the circuit. **a)** and **b)** Excitation applied at opposite boundaries. The voltage signal remains confined to the respective edge, propagating in opposite directions as expected for chiral edge states. **c)** showcase a localized circuit response for a bulk injection, differing from the edge excitation. **d)** Finite system without periodic boundary conditions. Here, the excitation pulse demonstrates its ability to traverse the system boundaries.

3.3.4. Real Operational Amplifiers

Our exploration thus far has relied on ideal operational amplifiers (Op-Amps) within the INICs, giving clear results about the circuit's behavior. Now, we take a crucial step towards realism by incorporating non-ideal Op-Amps readily available in the market, readily found within LTspice libraries. This transition raises a set of questions: Will employing real-world Op-Amps introduce new phenomena not observed with their idealized counterparts? Can the effects of these non-ideal components be directly observed and quantified within the J matrix? Will the robust nature of the Haldane model's topology be sufficient to preserve the observed edge states under the influence of these realistic components?

Addressing these questions through careful simulations and analysis will not only validate our circuit model's fidelity to real-world systems but also provide valuable information about the interplay between topological states and circuit imperfections.

Following the insights provided by Hofmann et al. (2019) [56], we replace the ideal Op-Amps with the LT1363 operational amplifiers (Op-Amp) as the non-ideal component implementation with the same structure presented in Figure 3.7.

A crucial aspect of the realistic Op-Amps is its requirement for a separate external voltage source beyond the one used for excitation. This voltage, specified as ranging from ±2.5V to ±15V, significantly impacts the circuit's computational overhead. Increasing the voltage leads to a disproportionate escalation in simulation time, particularly noticeable in tasks like band structure calculations. Figures 3.11 and 3.12 illustrate this, showcasing the dramatic rise in computation time for three different external voltages as the system size (number of nodes) increases. We could leave the external sources high and perform less calculations using the methodology presented in Section 2.3 to reduce the total number of iterations, but since we wanted to also obtain the complete J matrix this was not an option.

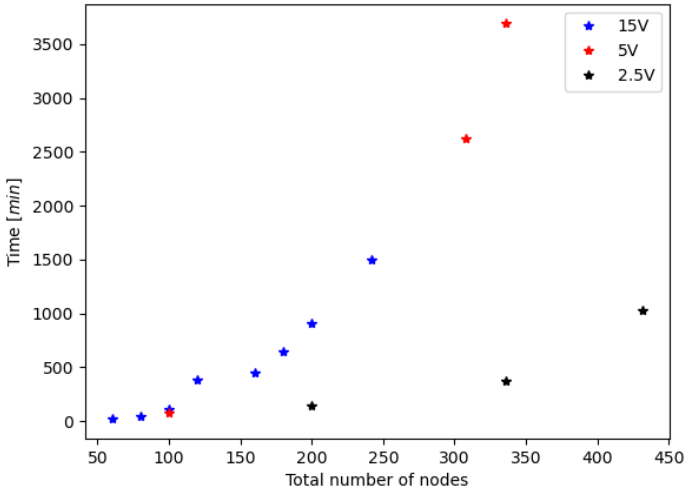

Figure 3.11: Total calculation time for band structure opposed to total number of nodes, each color represents the external voltage feeding the real Op-Amps.

Leaving the Op-Amps connected to a large external source does not allow for a quick convergence to the DC operating point that is needed to perform the band calculations in each iteration. However, we found that so much amplification is not necessary and that the external voltage of $V = \pm 2.5$ is more than sufficient, while also ensuring reasonable calculation times. The 3 voltages used correspond to those tabulated in the specifications of this Op-Amp model.

Considering this, the band structure of a Haldane model circuit with its real Op-Amps is presented in Figures 3.13 and 3.14 the J matrix comparison with the theoretical H Hamiltonian of the corresponding system.

While the overall shape of the band structure remains preserved, Figure 3.13 reveals differences between the ideal case (dashed lines) and the circuit response with non-ideal Op-Amps (crosses). To dissect these differences, Figure 3.14 compares the measured J matrix from the circuit simulation with the theoretical Hamiltonian H. As evident from the zoomed-in views in Figure 3.14(c) and (d), the major deviations originate from the next-nearest neighbor (NNN) terms associated with the INICs.

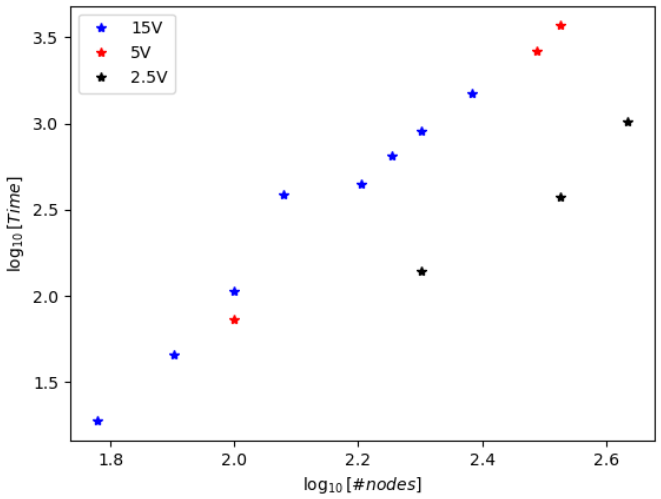

Figure 3.12: Another visualization of the data shown in Figure 3.11 but in $log - log$ scale. This representation shows the power law scale of the calculation times, alerting that for bigger systems the total times can increase drastically.

Our analysis suggests that the non-ideal Op-Amps introduce errors in the desired $\phi = \pi/2$ phase shift within the NNN terms. Unlike the ideal configuration, the realized INICs not only exhibit an imaginary component but also possess a small real component, indicating a deviation from the purely imaginary phase shift expected. Also this effect is increased in the negative configuration, giving an effective Z impedance in one direction and $|Z'| \neq |Z|$ in the opposite, differing from the $Z' = -Z$ expected from the ideal implementation. This adds a non-Hermitian extra term to the simulations.

Does this effect destroy the edge states? We replicate the excitation strategy previously employed with ideal Op-Amps.

Figures 3.15(a) and (b) shows that despite the band structure differences, chiral edge states persist within the circuit model even with non-ideal Op-Amps. Similar to the ideal case, the applied pulse excitation remains confined to the designated edge, with minimal leakage into the bulk. Additionally, the excitation propagates along each edge in opposite directions, echoing the theoretical expectations of chiral edge states.

However, a notable difference compared to the ideal case is the increased level of dissipation observed in the propagating wave packet. This phenomenon is visually apparent in Figure 3.15(d), where the wave packet exhibits a more pronounced decay compared to Figure 3.10(d). This heightened dissipation can be attributed to the non-ideal characteristics of the Op-Amps, most likely arising from the imperfect phase shift within the NNN terms.

The last way of evidencing the damping is in Figure 3.16 where the maximum of the voltage signal of each unit cell is shown for a Gaussian excitation. In this figure the dissipation effect is more evident and even a presence of bulk leakage is depicted.

In this section the Haldane circuit was revised, the circuit showed a good accordance with its tight binding homologous. The edge states where observed and the band structures computed, showing the capabilities of circuits as a platform for observing different topological manifestations. It also acknowledge the implementation of realistic components, showing its

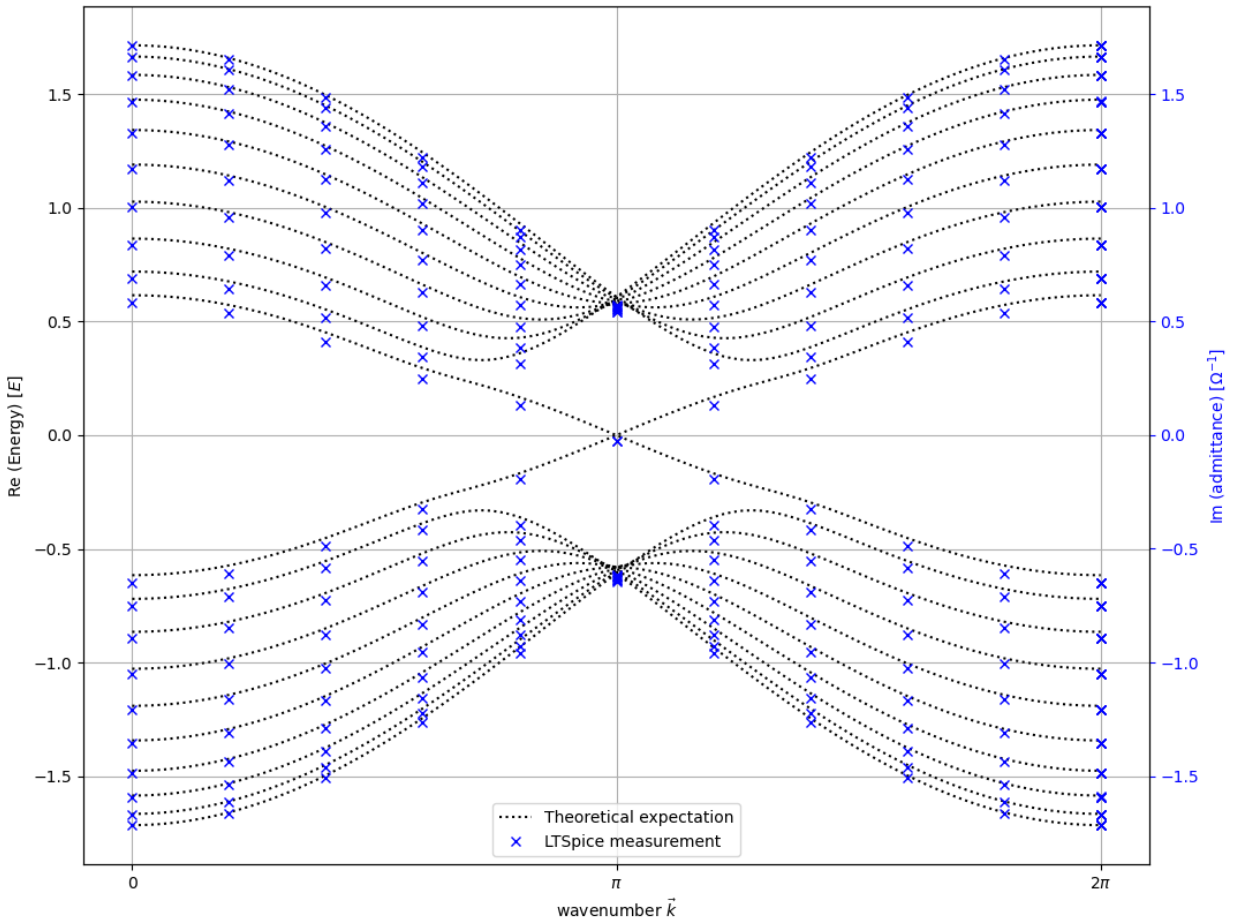

Figure 3.13: Measured admittance band structure of the Haldane circuit with realistic Op-Amps (blue crosses) with $\omega \approx w_0$, $C_0 = 10\mu$F, $L_0 = 10\mu$H and $R = 20\Omega$ contrasted with the band structure of the corresponding tight binding model (dashed lines).

effects in the Laplacian and consequently in the band structure.

The next section studies another model, proposed by Colomés and Franz [2] known as the modified Haldane model. The methodology will remain the same as the one presented in this section: Observe the expected edge states and compute the band structure.

3.4. Colomés and Franz model

The motivation for choosing the modified Haldane model is that, as discussed in [2], it is predicted to have antichiral edge states. That is, edge states that propagates in both boundaries but in the same direction, as opposed from the Haldane case. This antichiral states are accompanied by some bulk states that propagate in the opposite direction of the boundary ones. If we implement a successful design for this circuit it should present a similar response as the Haldane model in Figure 3.10 but with larger voltages in the bulk.

The exploration unfolds the same way as before in four stages: **1.-** Discussing the circuit design. **2.-** Band Structure Analysis, highlighting the differences between the grounded Laplacian and the Hamiltonian. **3.-** Direct Observation of Edge States via voltage measurements.

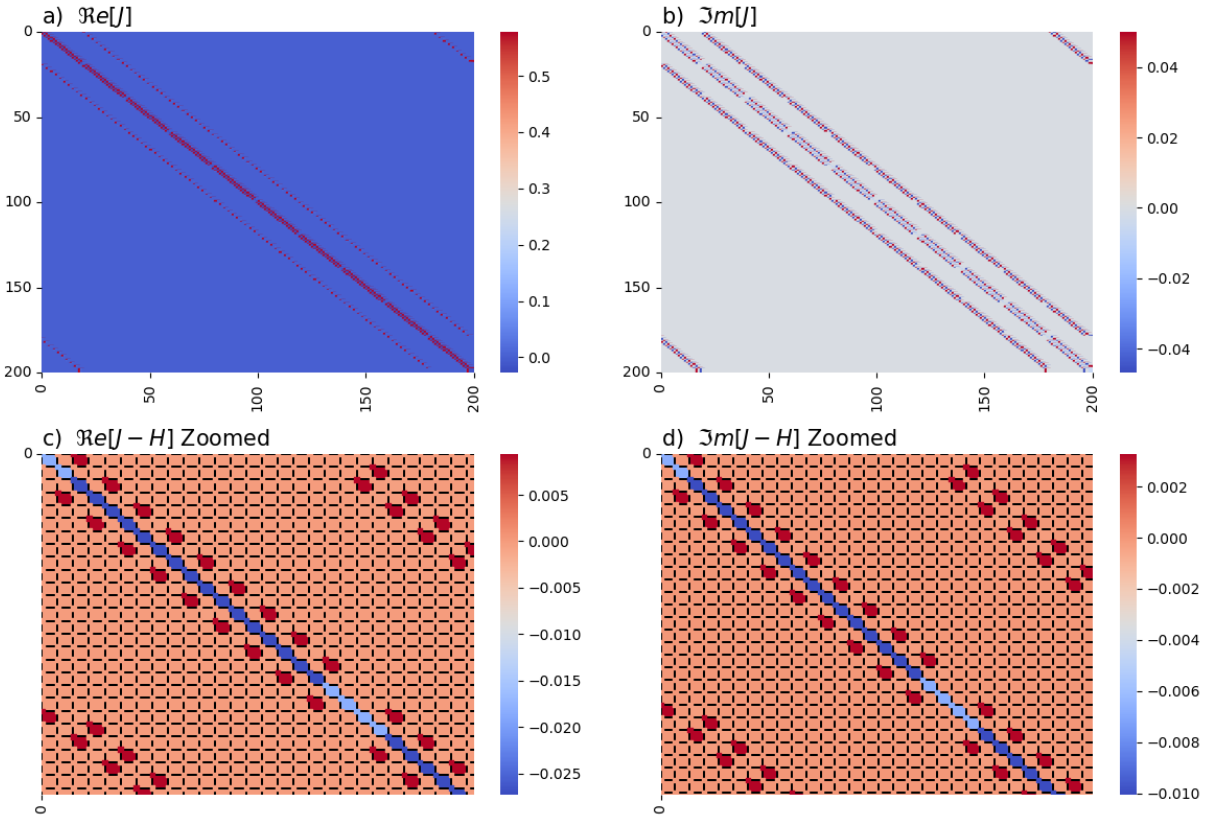

Figure 3.14: Comparison between the J matrix, computed from the circuit simulation (same parameters as in Figure 3.13), and the Hamiltonian H of the analog system for $t_1 = 0.58$, $t_2 = 0.05$ and $\phi = \pi/2$. In c) and d) is a zoomed portion of the difference matrix to accentuate the structure of the difference.

4.- Incorporating Real-World Elements.

3.4.1. Circuit design

This circuit presents a honeycomb structure with its nearest neighbors via a hopping amplitude t_1 and with its next-nearest neighbors (NNN) through a complex hopping $t_2 e^{i\phi}$ with a specific sign rule illustrated in Figure 1.12.

This complex hopping is also facilitated by an INIC implementation of R_0 absolute resistance that, for the beginning of this study, is done with idealistic Op-Amps. The NN connection is achieved using capacitors C_0 inherited from graphene circuit, as well as its grounding.

Figure 3.17 showcases the circuit designed to simulate the bulk of the modified Haldane model. Building upon the familiar connections employed in the Haldane model, this circuit introduces a crucial modification: the NNN connections in the B sub-lattice is turned around in order to replicate the sign rule shown in 1.12.

For this implementation, writing the currents for a pair of nodes A and B in a j unit cell

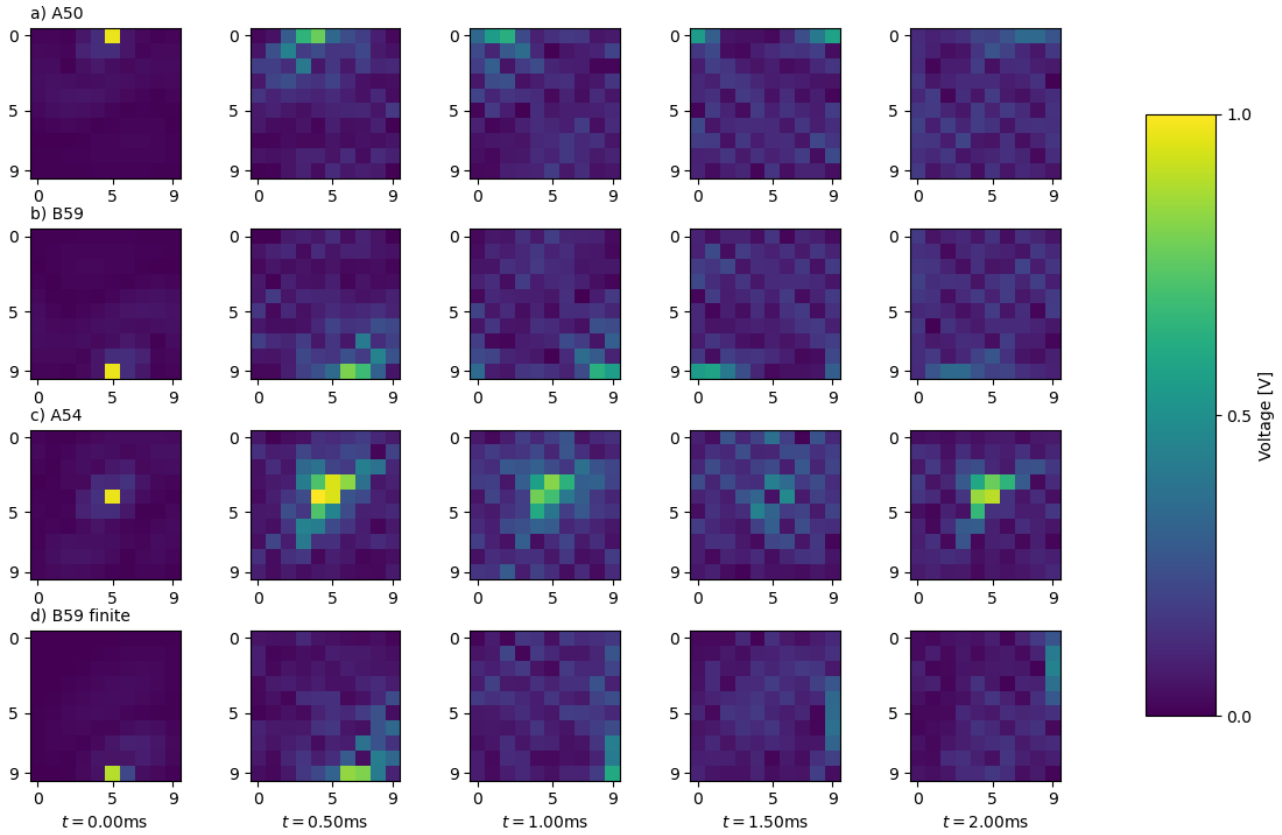

Figure 3.15: Time-resolved voltage signal per unit cell for a Gaussian pulse excitation in different nodes across the Haldane circuit with realistic Op-Amps. **a)** and **b)** shows the chiral edge states. **c)** showcase a localized circuit response for a bulk injection, differing from the edge excitation. **d)** is for a finite systems in all directions, we we that the excitation is able to travel across the boundary but with noticeable dissipation.

and using the notation presented the first chapter, the Kirchhoff equations lead to:

$$\begin{aligned} I_{Aj} = {} & i\omega C_0\big(V_{Aj} - V_{Bj}\big) + i\omega C_0\big(V_{Aj} - V_{Bj-1}\big) + i\omega C_0\big(V_{Aj} - V_{Bj-2}\big) + \left[i\omega C_{dp} + \frac{1}{i\omega L_0}\right]\big(V_{Aj} - V_0\big) \\ & + \frac{1}{R_0}\big(V_{Aj} - V_{Aj-1}\big) + \frac{-1}{R_0}\big(V_{Aj} - V_{Aj-2}\big) + \frac{1}{R_0}\big(V_{Aj} - V_{Aj-3}\big) + \frac{-1}{R_0}\big(V_{Aj} - V_{Aj+1}\big) \\ & + \frac{1}{R_0}\big(V_{Aj} - V_{Aj+2}\big) + \frac{-1}{R_0}\big(V_{Aj} - V_{Aj+3}\big), \end{aligned} \tag{3.14}$$

$$\begin{aligned} I_{Bj} = {} & i\omega C_0\big(V_{Bj} - V_{Aj}\big) + i\omega C_0\big(V_{Bj} - V_{Aj+1}\big) + i\omega C_0\big(V_{Bj} - V_{Aj+2}\big) + \left[i\omega C_{dm} + \frac{1}{i\omega L_0}\right]\big(V_{Bj} - V_0\big) \\ & + \frac{1}{R_0}\big(V_{Bj} - V_{Bj-1}\big) + \frac{-1}{R_0}\big(V_{Bj} - V_{Bj-2}\big) + \frac{1}{R_0}\big(V_{Bj} - V_{Bj-3}\big) + \frac{-1}{R_0}\big(V_{Bj} - V_{Bj+1}\big) \\ & + \frac{1}{R_0}\big(V_{Bj} - V_{Bj+2}\big) + \frac{-1}{R_0}\big(V_{Bj} - V_{Bj+3}\big). \end{aligned} \tag{3.15}$$

We establish the relationship between resistance values and the desired phase shift within

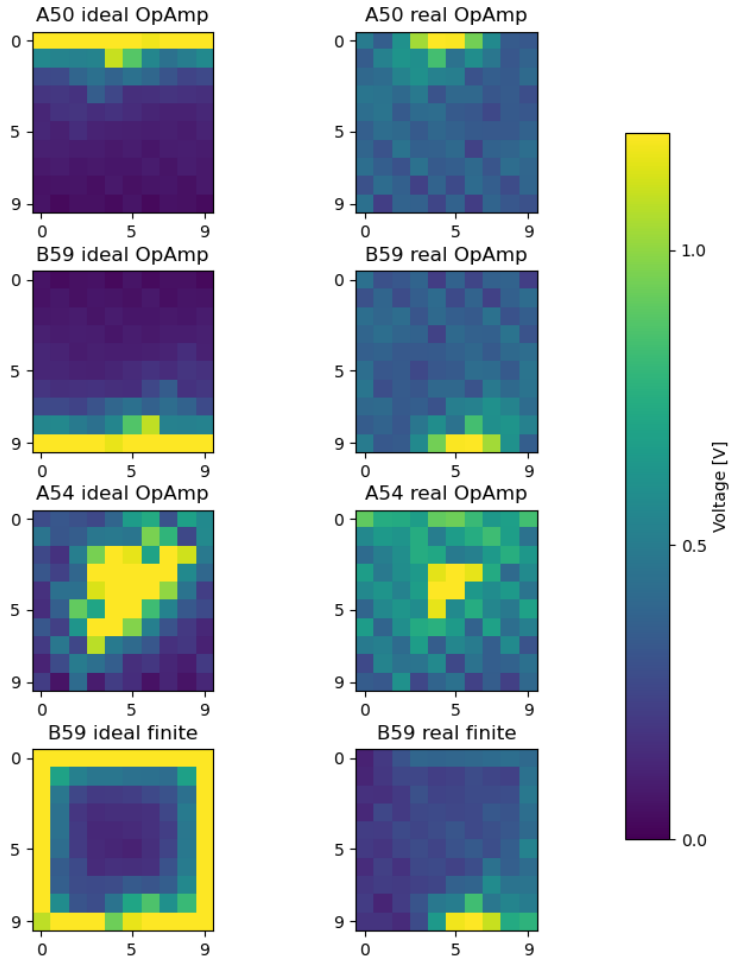

Figure 3.16: Comparison between ideal and real Op-Amp implementation for the maximum voltages of each unit cell for Gaussian pulse excitation across different nodes. Real Op-Amps show more dissipation than ideal ones, it allows for bulk leakage in edge injection.

the NNN terms. Setting $R_a = R_b = 1$ results in a phase shift of $\phi = \pi/2$, making all resistance values purely real numbers. This simplifies the calculations and analysis due to the absence of extra imaginary components.

Comparing Equations 3.15 and 3.11 reveals the key difference: the sign of the NNN hopping terms in the current expression for node B. This seemingly minor modification impacts the edge state behavior and band structure, justifying closer analysis in the subsequent sections.

Considering the equations for all nodes in the circuit, the current equation can be written in matrix form:

$$\mathbf{I} = J_{MH}\mathbf{V}, \tag{3.16}$$

where J_{MH} is the grounded Laplacian of the system in position representation. Imposing periodic conditions and Fourier transforming J_{MH} lead us to the momentum space represen-

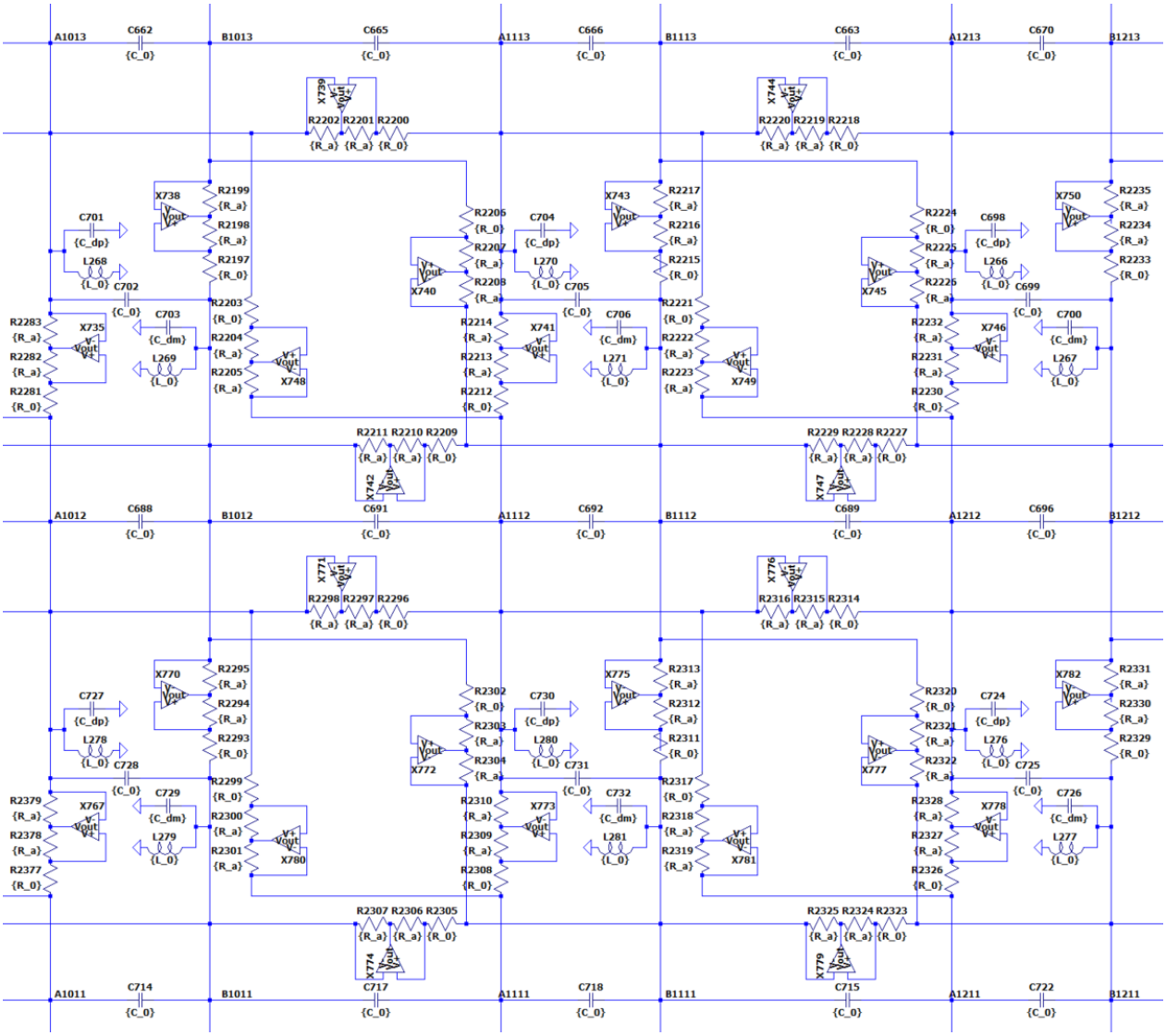

Figure 3.17: Zooming in on the bulk for the implementation of the Haldane model circuit, centered at unit cell $11, 12$ with nodes $A1112$ and $B1112$ exemplify the connections: Capacitors C_0 to NN, while INICs controlled by absolute resistance R_0 bridge the gap between next-nearest neighbors across sub-lattices, differing from 3.7 in the direction of the connection for the B sub-lattice. Each node is grounded with inductors L_0 and sub-lattice-specific capacitors (C_{dp} for A, C_{dm} for B), Although currently set to zero for simplicity, these sub-lattice capacitors hold the potential to break inversion symmetry, acting as a Semenoff mass [67].

tation

$$J_{MH} = i\omega \Bigg[\Bigg(3C_0 + \frac{C_{dp} + C_{dm}}{2} - \frac{1}{\omega^2 L_0} + \frac{2}{\omega R_0} \Big(\sin(k_x) - \sin(k_y) - \sin(k_x - k_y) \Big) \Bigg) \mathbb{I} - C_0 \Big(1 + \cos(k_x) + \cos(k_y) \Big) \sigma_x - C_0 \Big(\sin(k_x) + \sin(k_y) \Big) \sigma_y + \Big(\frac{C_{dp} - C_{dm}}{2} \Big) \sigma_z \Bigg], \tag{3.17}$$

successfully replicating the structure of the modified Haldane model Hamiltonian 1.35 by changing the INIC term from σ_z to $\mathbb{I}$ to act as a pseudoscalar potential [2]. This configuration of INICs produces the desired effect in the circuit. The grounding capacitors effectively simulate the Semenoff mass component but we are not interested in this effect for this study so we set $C_{dp} = C_{dp} = 0$.

3.4.2. Band structure analysis

In order to observe the edge states presented in the circuit a ribbon has to be constructed. We stick with the decision taken in Section 3.3.2 and perform a ribbon with zig-zag terminations, grounding each NN missing connections in the boundary with its corresponding capacitor C_0. We use this configuration since it is simpler to construct with the geometry of the circuit, it is not impossible to implement Armchair edges but it requires more work for the indexation of G.

To compute the conductance matrix G for the ribbon geometry we impose periodic boundary conditions. Following the protocol in Section 2.3 we successfully calculate the admittance band structure. These results are presented in Figures 3.18 for the band structure, and 3.19 the J matrix analysis.

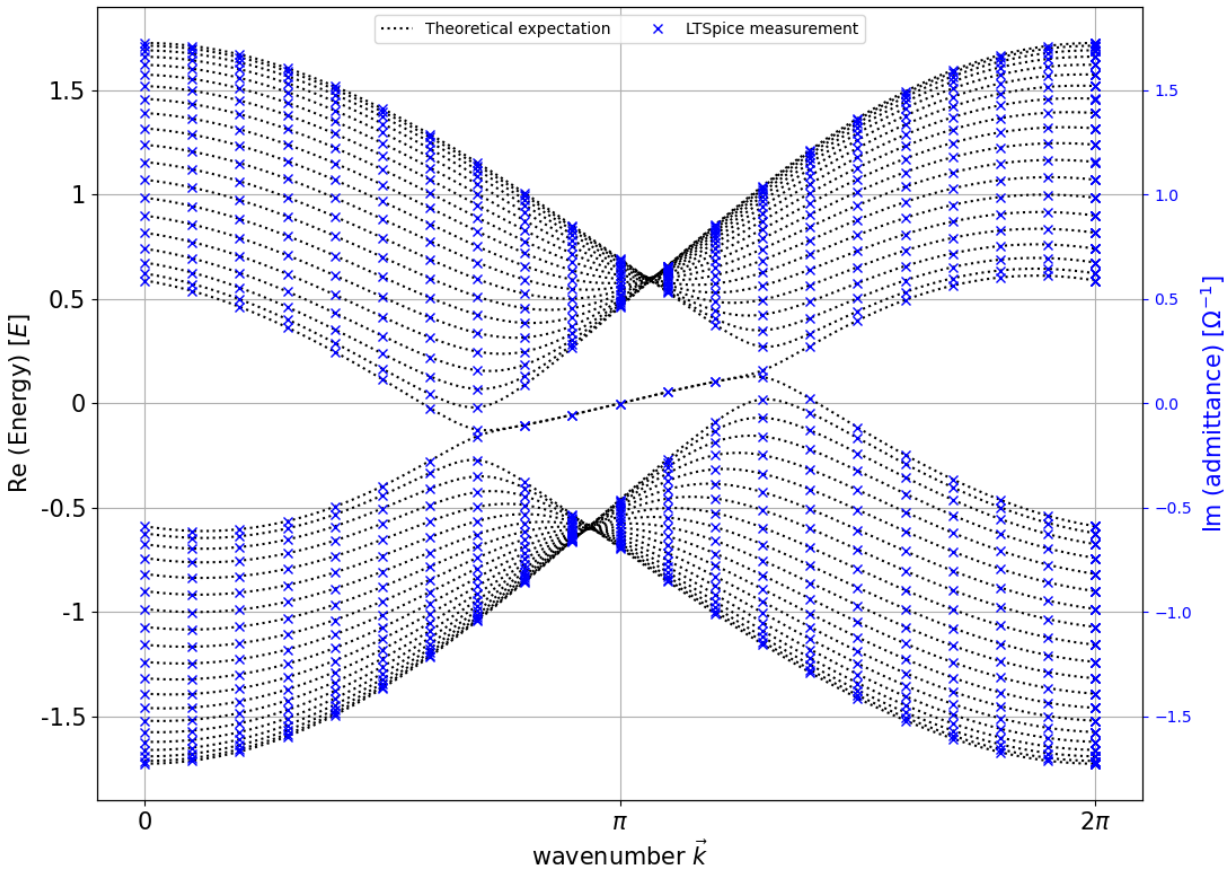

Figure 3.18: Measured admittance band structure of the implemented modified Haldane circuit (blue crosses) with $\omega \approx \omega_0$, $C_0 = 10\nu$F, $L_0 = 10\nu$F and $R = 34\Omega$ contrasted with the band structure of the corresponding tight binding model (dashed lines)

Figure 3.18 shows the ribbon band structure for a circuit of 20 units cells width and 20 unit cells in the periodic direction with the specified parameters. The data obtained with LTSpice (blue crosses) matches with the theoretical band structure of the tight binding model, assuring that our implementation is in the right direction.

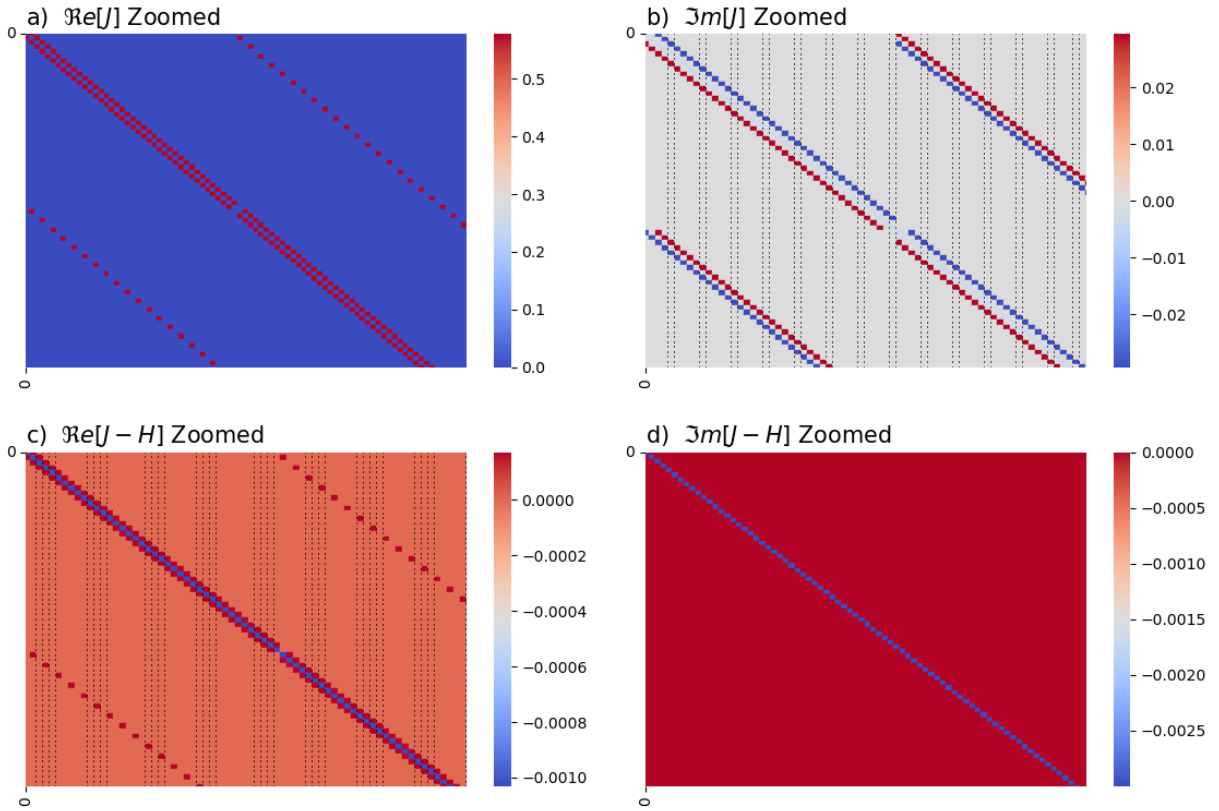

Figure 3.19: Zoomed in comparison between the J matrix, computed from the circuit simulation (same size and parameters as in Figure 3.18), and the Hamiltonian H of the analog system for $t_1 = 0.58$, $t_2 = 0.03$ and $\phi = \pi/2$. As the matrices are to big to actually notice a difference, thanks to the scale in the zoomed version the qualitative agreement between them is evident.

On the other hand, Figure 3.19 examines the measured J matrix and its difference from the theoretical Hamiltonian H. Just as in the Haldane model, the implementation of idealistic INICs produces the desired effects in with little to no discrepancies with the theoretical interactions. Again, an imaginary diagonal term emerges, attributed to the expected parasitic resistances inherently introduced in the grounding inductors by LTSpice during simulations. The change in the INICs direction for sub-lattice B is also noticeable in 3.19(b), by comparison with 3.9(b) the two sub-lattices share the same sign for the NNN connection, as expected from the design.

3.4.3. Edge states

Due to the results in Figure 3.18 and 3.19 we have the confirmation that our connection design is behaving as expected. As mentioned at the beginning of the section, the objective is to observe the edge states in this system so the next step is to excite the ribbon at its

boundaries and bulk to see its reaction.

As implemented in section 3.3.3, we check the dynamics with Gaussian pulses. Figure 3.20 shows the results obtained from this procedure.

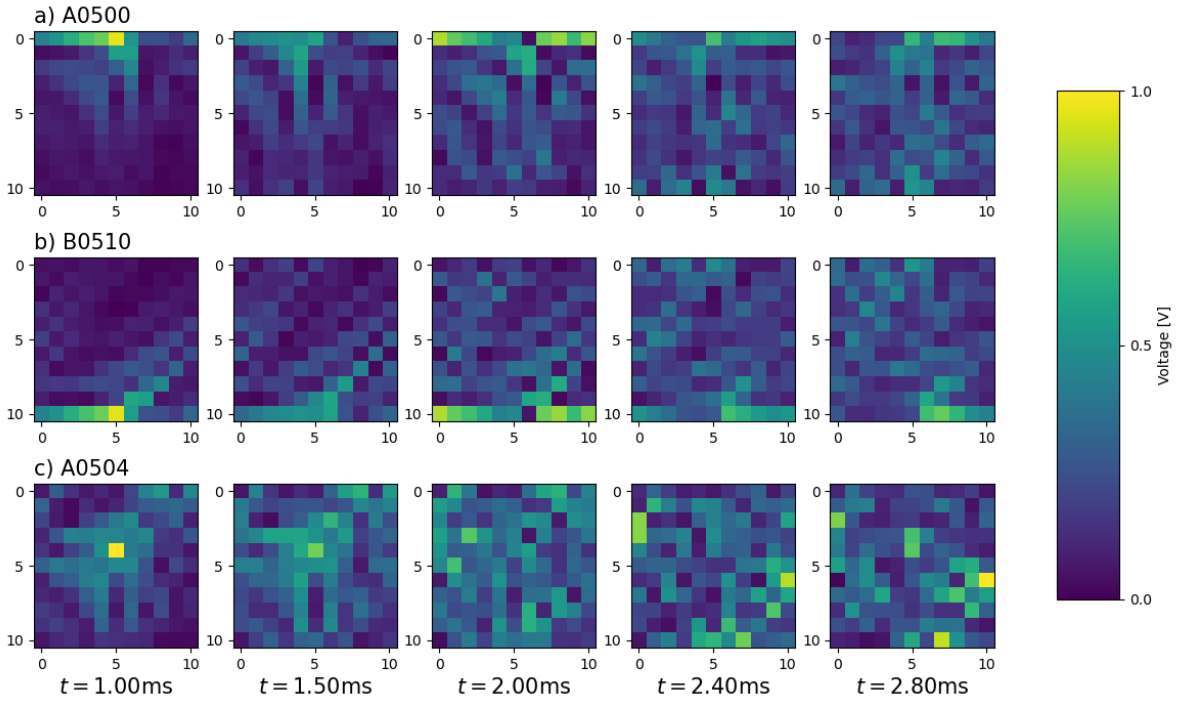

Figure 3.20: Time-resolved voltage signal per unit cell for a Gaussian pulse excitation in different nodes across the modified Haldane circuit with ideal Op-Amps. **a)** and **b)** shows the antichiral edge states. **c)** showcase a bulk injection, differing from the edge excitation since the voltage propagates en various directions.

Figures 3.20(a) and (b) reveal a distinct behavior compared to the ideal Haldane model. Contrary to the opposite-direction propagation in Figure 3.10, both injections in the modified model travel across their respective edges in the same direction. This phenomenon aligns with the predictions for anti-chiral edge states in Colomés et al.(2018)[2].

Figure 3.20 clearly showcases non-trivial bulk contributions accompanying the edge behavior. Compared to the ideal case, bulk nodes exhibit a non-negligible voltage response, indicating some degree of leakage from the edge into the bulk. This leakage arises from the inherent modification of the Haldane model, allowing for bulk states to hybridize with the edge states and propagate with them.

Based on the presented results, we can confidently conclude that the proposed antichiral edge states do indeed exist within the modified Haldane model and offer the potential for direct observation. This finding represents a significant step forward in the exploration of exotic phenomena within circuit-based platforms.

However, a crucial question remains: how do these antichiral edge states fare under the influence of more realistic components? To address this concern, we will follow the same investigative path taken in the Haldane implementation in the next subsection analyzing the system with non-ideal Op-Amps.

3.4.4. Real Operational Amplifiers

To address the concern of more realistic components we will implement non ideal Operational Amplifiers (Op-Amps) to our INIC implementation. Since this study is a continuation from the Haldane implementation we will keep the same LT1363 implemented before because we got satisfactory results from its implementation.

One of the observations made at the end on Section 3.3.4 was that the real INIC implementation present a non-Hermitian feature: Instead of giving impedance of $\frac{1}{R}$ in one direction and $\frac{-1}{R}$ to the other it actually gives an impedance $\frac{1}{R}$ to the positive direction and $Z = \mathrm{Re}[Z] + i\,\mathrm{Im}[Z]$ where $\mathrm{Re}[Z] \approx \frac{1}{R}$ but not quite the exact value. This should have repercussion on the band structure and be more evident in the difference between J and H.

Also, following the evidence presented before about the calculation times in Figures 3.11 and 3.11 we feed the LT1363s with a ± 2.5V external voltage source.

We implement a circuit with the same structure of the one in Figure 3.17 but with the LT1363 realistic Op-Amps. Figures 3.21 and 3.22 resume our results.

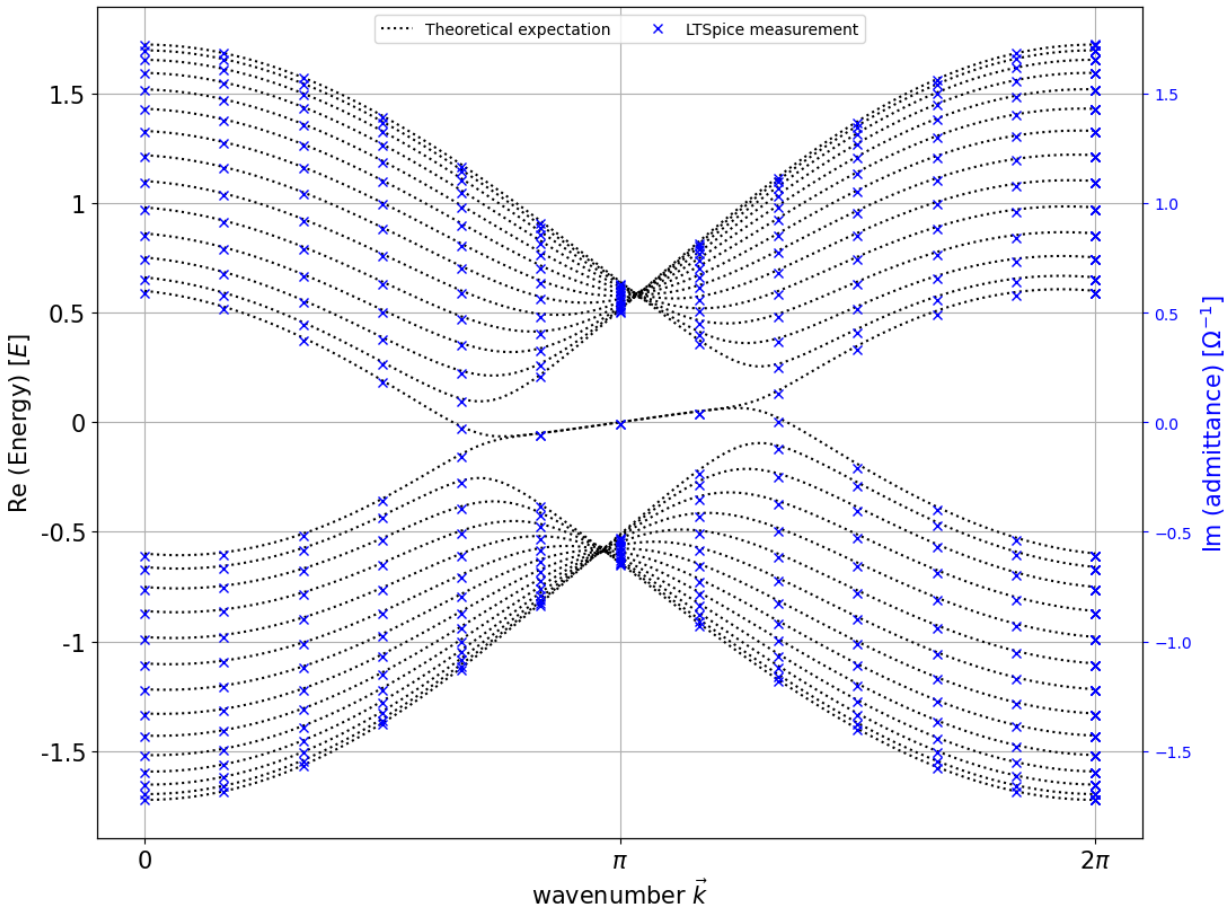

Figure 3.21: Measured admittance band structure of the modified Haldane circuit with realistic Op-Amps (blue crosses) with $\omega \approx w_0$, $C_0 = 10\mu$F, $L_0 = 10\mu$H and $R = 60\Omega$ contrasted with the band structure of the corresponding tight binding model (dashed lines).

The overall shape of the band structure remains preserved, Figure 3.21 reveals differences between the ideal case (dashed lines) and the circuit response with non-ideal Op-Amps

(crosses). To dissect these differences, Figure 3.22 compares the measured J matrix from the circuit with the theoretical Hamiltonian H. As evident from the zoomed-in views in Figure 3.14(c) and (d), the major deviations originate from the next-nearest neighbor (NNN) terms, as mentioned before, associated with the non-Hermitian effects of the realistic INICs

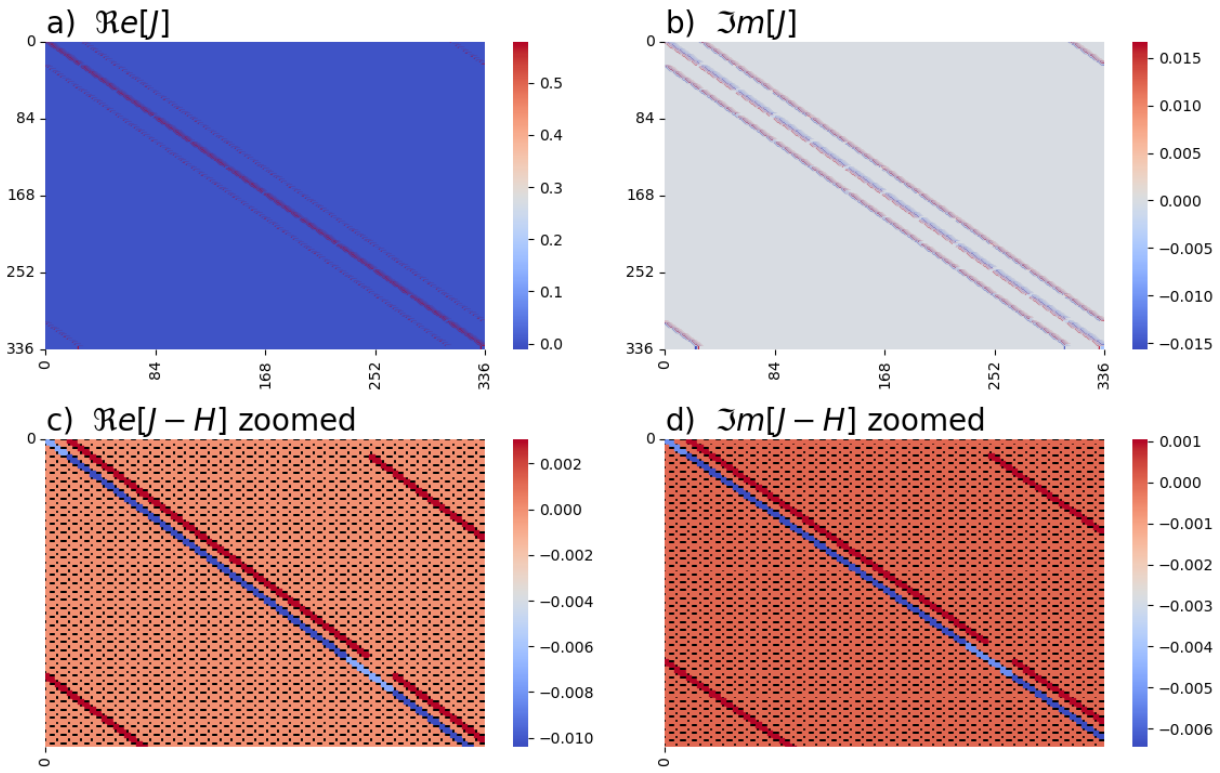

Figure 3.22: Comparison between the J matrix, computed from the circuit simulation (same parameters as in Figure 3.21), and the Hamiltonian H of the analog system for $t_1 = 0.577$, $t_2 = 0.017$ and $\phi = \pi/2$. In c) and d) is a zoomed portion of the difference matrix to accentuate the structure of the difference.

Does this effect destroy the edge states? Following the study mentioned in the Haldane implementation 3.3.4, we replicate the excitation strategy.

Figures 3.23(a) and (b) shows that despite the band structure differences, antichiral edge states persist within the circuit model even with non-ideal Op-Amps. Similar to the ideal case, the applied pulse excitation remains in the designated edge, propagating along each boundary in the same directions, echoing the theoretical expectations of antichiral edge states.

However, a notable difference compared to the ideal case is that, although the edge voltages present a level of dissipation through the propagation, the bulk states that where present in all Figure 3.20 are now suppressed. This phenomenon is visually apparent in Figure 3.15(a) and (b), where the bulk is on a darker blue than the ones in 3.20 and also in Figure 3.24. This phenomena can be attributed to the non-ideal characteristics of the Op-Amps, most likely arising from the imperfect phase shift within the NNN terms.

An initial idea to explain this last phenomenon was that, since the realistic INICs present a non-Hermitian term, there could be non-Hermitian skin effect [53] (NHSE) on the system. The NHSE manifest When adding non-Hermitian terms in a Hermitian Hamiltonian, the

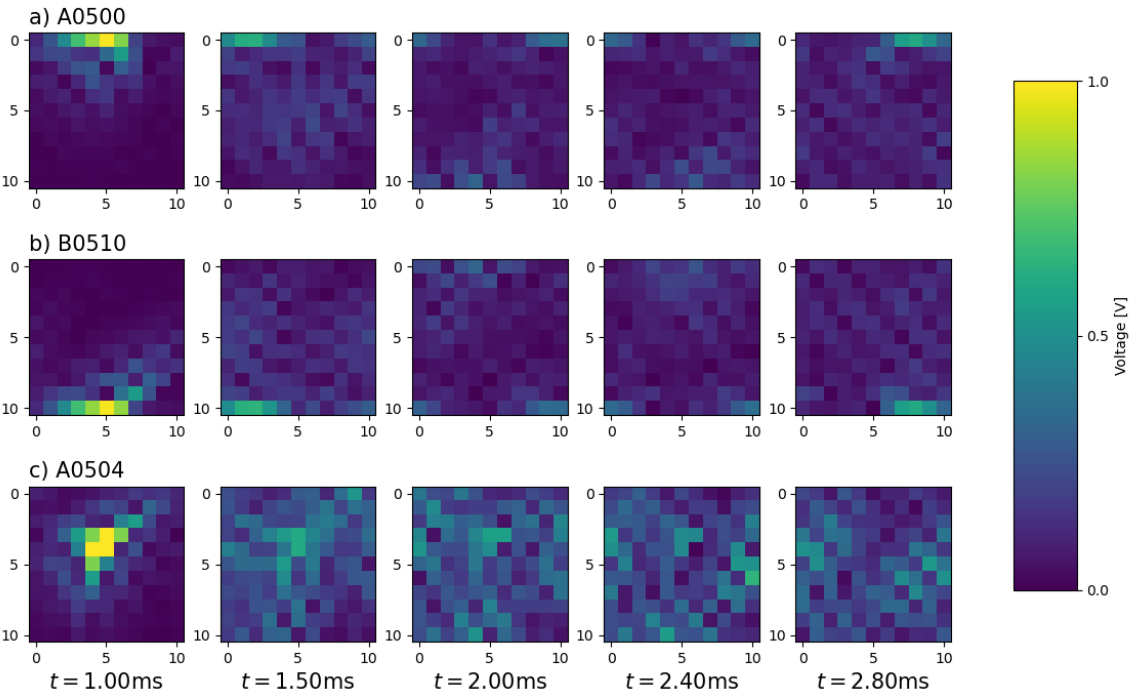

Figure 3.23: Time-resolved voltage signal per unit cell for a Gaussian pulse excitation in different nodes across the modified Haldane circuit with realistic Op-Amps. **a)** and **b)** shows the antichiral edge states. **c)** showcase a bulk injection, differing from the edge excitation since the voltage propagates en various directions.

bulk eigenstates of the original Hamiltonian localize at a boundary and lose their extended nature. To study this we went the other way around now, in order to check if the type of interaction associated to the realistic INICs where able to produce skin effect we built numerically a bigger tight-binding system with this exact interaction and checked if any bulk states produced any level of localization.

Figure 3.25 showcases the difference of our numerically created non-Hermitian Hamiltonian with the one obtained from the electrical circuit. The accordance between these two indicate us that we have the same type of interactions in both of them.

With the confirmation presented, in Figure 3.26 is presented the band structure for a bigger system with 50 unit cells of width and infinite on the other direction with 110 k-points. Each point has as color the Inverse Participation Ratio (IPR) in $\log_{10}$ scale to exaggerate any contribution to localization. It appears that none of the bulk states are localized since for all bulk states the IPR is fairly small.

Another way of visualizing the localization is to plot each of the states in a matrix and plot the weight of its component in color. We present this in Figure 3.27, a zoomed version to the states that stand out in 3.28 and the same idea but in logarithmic scale to exaggerate any localization.

In synthesis:

- Figures 3.27, 3.28, and 3.29 collectively demonstrate localization exclusively for edge states, providing evidence against the presence of skin effect.

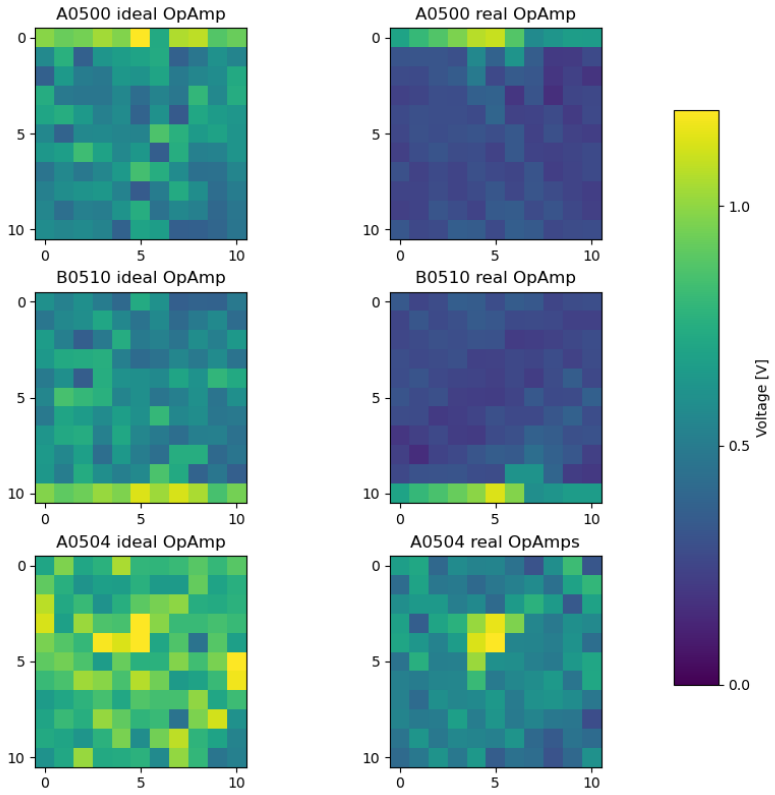

Figure 3.24: Comparison between ideal and real Op-Amp implementation of the modified Haldane model for the maximum voltages of each unit cell for Gaussian pulse excitation across different nodes. Real Op-Amps show more dissipation than ideal ones, ii allows for bulk leakage in edge injection.

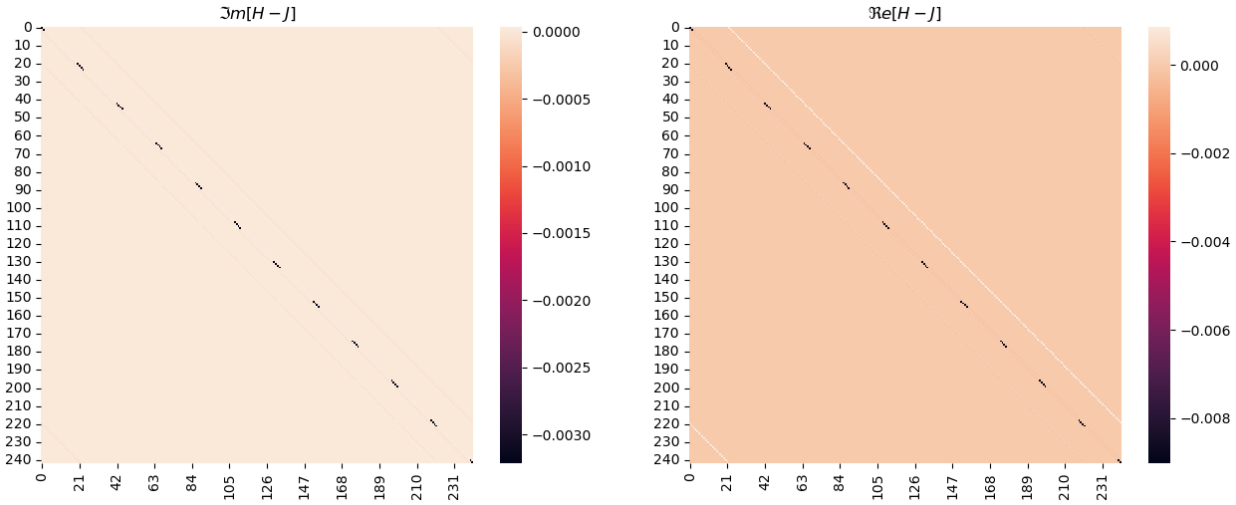

Figure 3.25: Difference between the non-Hermitian theoretical implementation of J, the main differences are from the grounding terms at the boundaries, witch are smaller than the scale of the elements in the H matrix.

- This conclusion signifies that the observed bulk propagation suppression in Figures 3.23 and 3.24 must stem from a different mechanism.

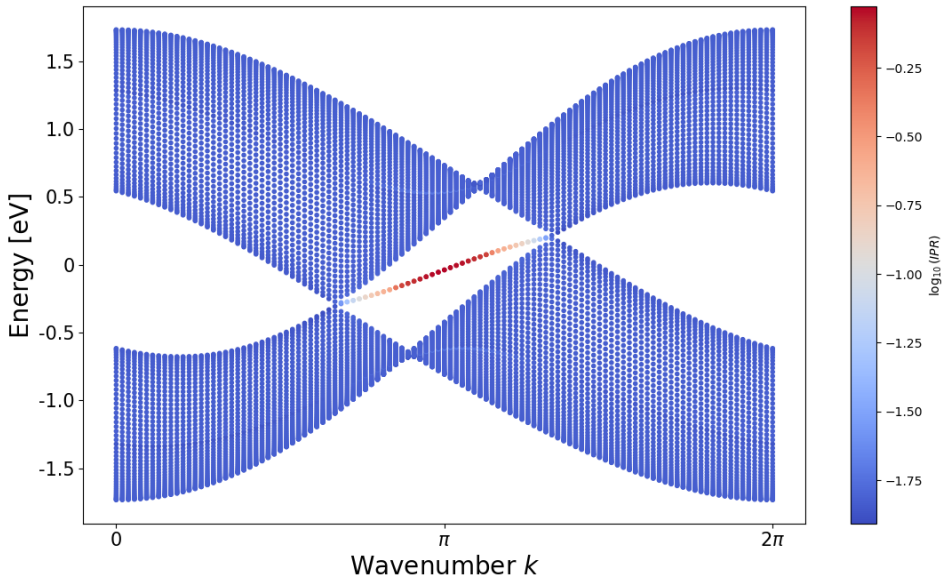

Figure 3.26: Band structure of the implementation of the non-Hermitian connection of the INICs for a bigger system in a tight binding Hamiltonian. Each point is colored according to the IPR of its associated state.

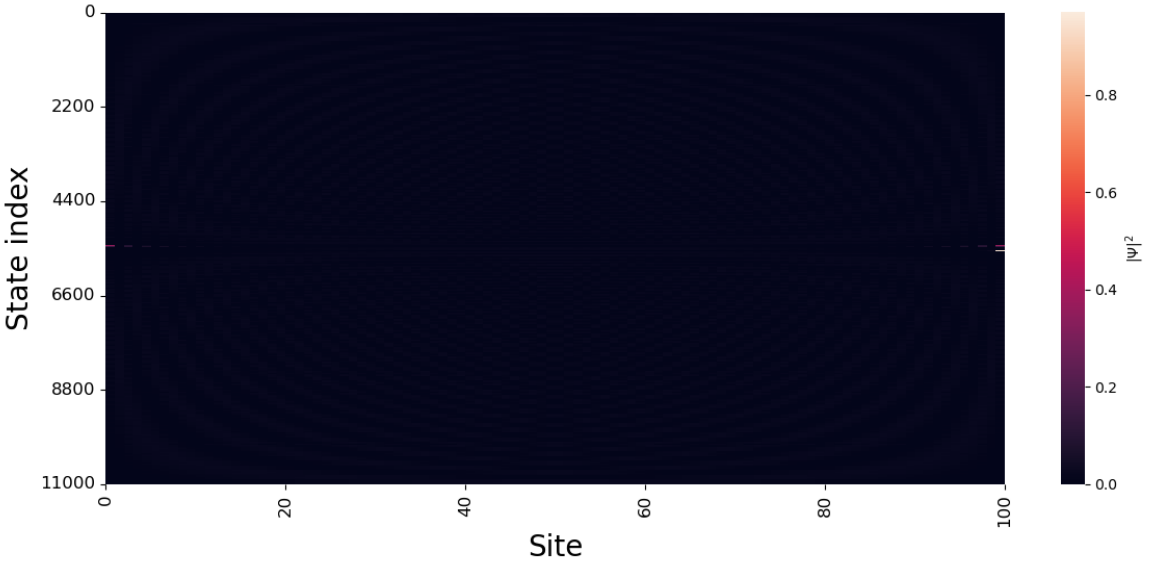

Figure 3.27: Matrix of states with the weights as color, just a few states present localization and they correspond to the energies in the gap, i.e. the edge states.

- Further supporting this notion, a hypothetical skin effect caused by realistic INIC implementation would have manifested as bulk suppression in the Haldane case as well. However, Figure 3.15 reveals the opposite, with leakage from edges into the bulk.

We discard the Skin effect as the source of the bulk suppression and the origin remains undetermined. Dissipation, as previously discussed in the Haldane section, appears as a potential candidate, but further investigation is required to establish its definitive role.

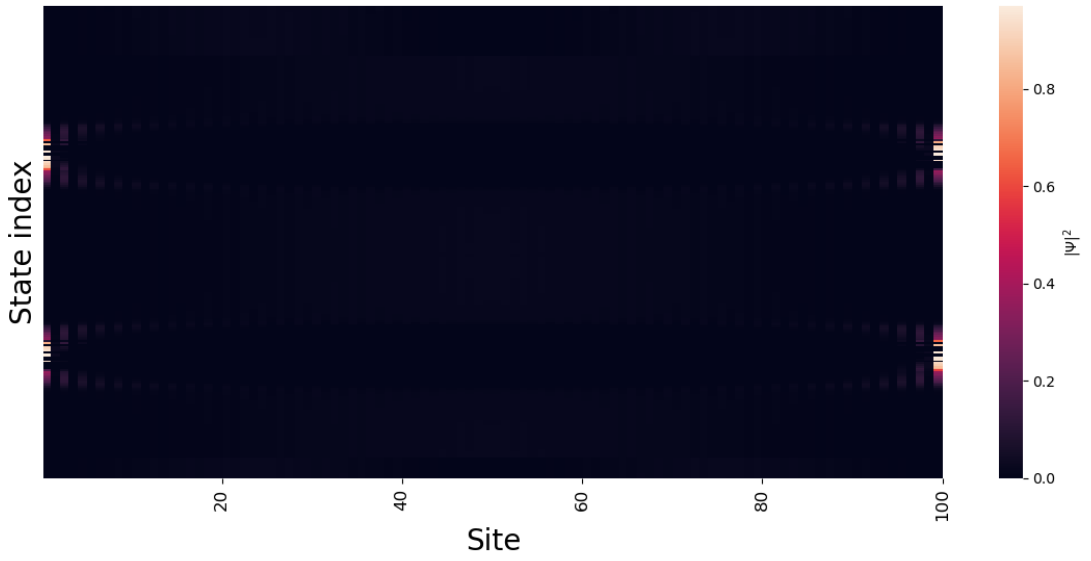

Figure 3.28: Zoomed version of the matrix of states with the weights as color, just a few states present localization and they correspond to the energies in the gap, i.e. the edge states.

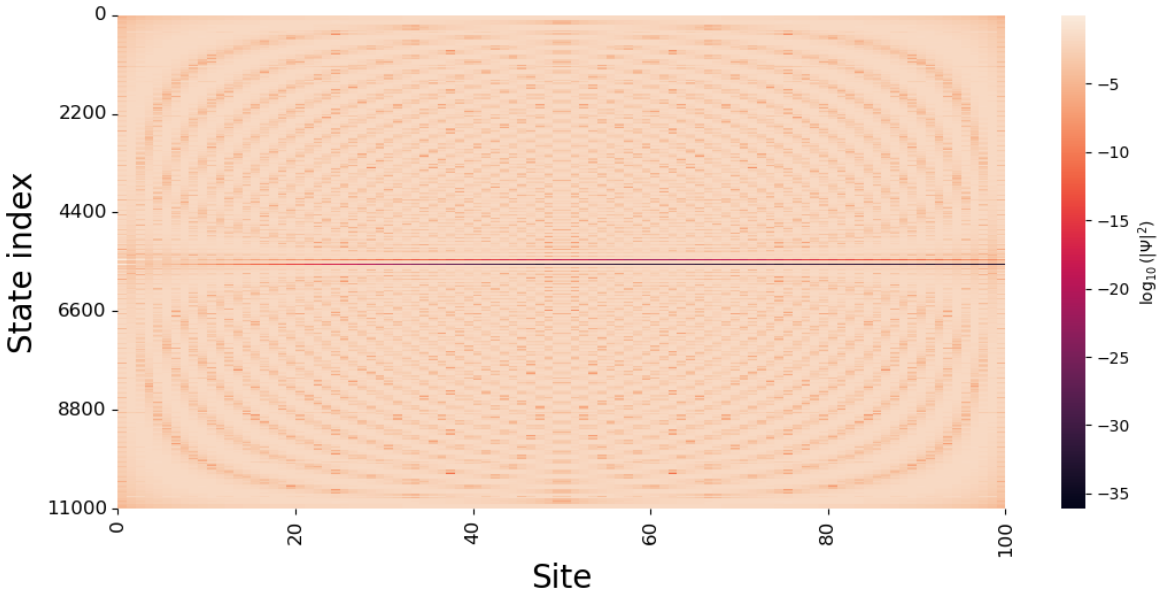

Figure 3.29: Matrix of states with the weights as color in logarithmic scale, just a few states present values near zero and they correspond to the energies in the gap, i.e. the edge states.

Even though we discarded the skin effect, its role as a contributing factor can still be investigated. As a future direction, we may consider implementing the skin effect through modifications to the circuit connections.

The beauty lies in how realistic components can introduce new effects and interactions. These can be captured within a tight-binding Hamiltonian, allowing us to model and understand these behaviors in hypothetical materials.

3.5. Dynamic skin effect

In the last discussion in section 3.4.4, we proposed making non-Hermitian considerations in the circuit. We checked for the non-Hermitian Skin effect, but the system did not present it. Since we proposed the idea, we have embarked on a study to implement non-Hermitian terms with electrical circuits.

We implement an analog circuit for the system presented in [4] of a non-Hermitian SSH model, like the one in [53]. The work of Haoshu Li and Shaolong Wan shows that wave packets in non-Hermitian systems can be accelerated or decelerated compared to their Hermitian counterparts, forming unconventional reflections to open boundaries. Using a non-Hermitian SSH model with asymmetric hoppings, we simulated the time-evolution of different initial states as depicted in Figure 3.30.

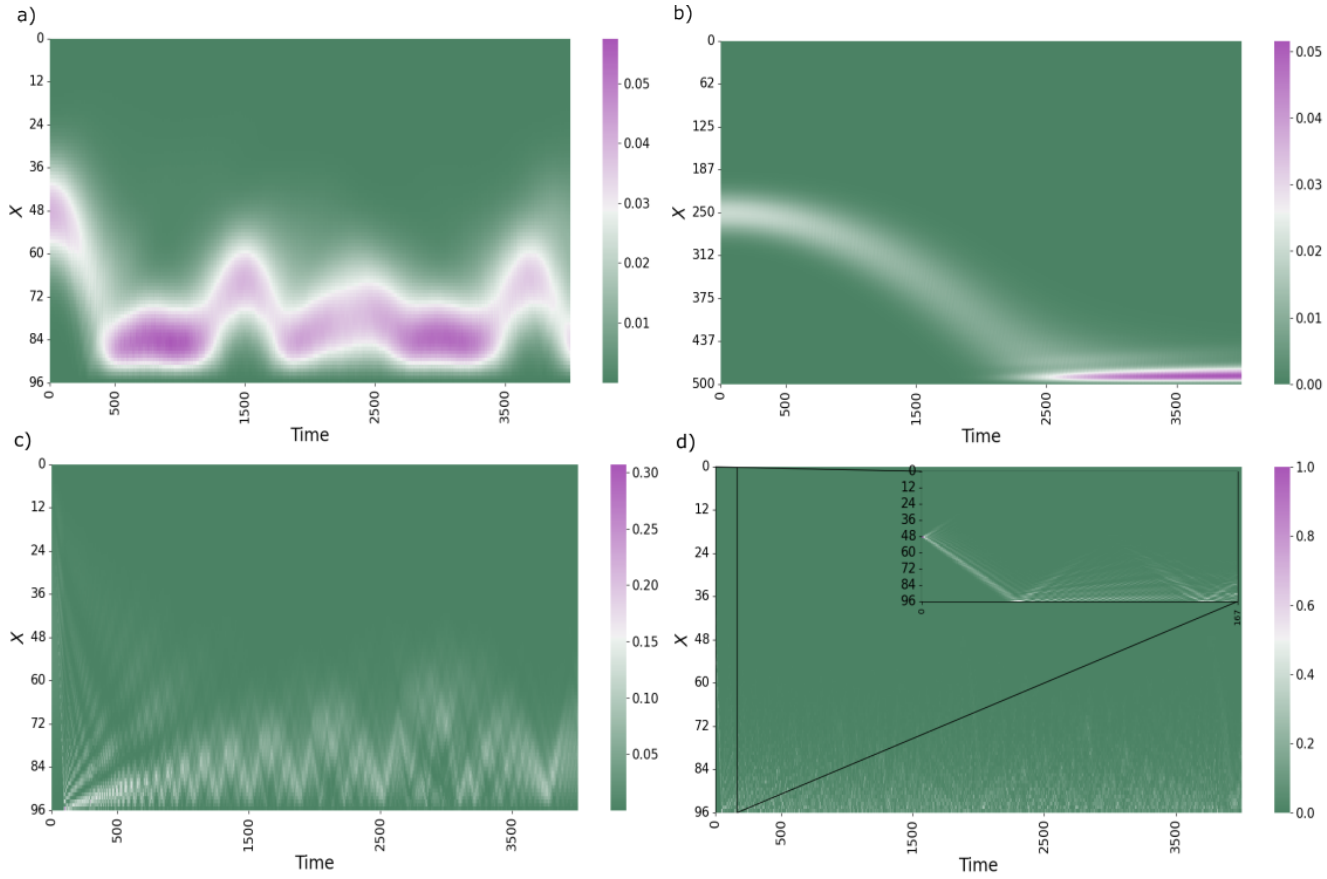

Figure 3.30: Time evolution of an initial wavepacket state with $k_0 = 0$ in a non-Hermitian SSH model [4] for different system sizes and initial conditions: **a)** 96 unit cells width, Gaussian initial condition with $x_0 = 48$ center position and $\sigma = 10$. **b)** 500 unit cells width, initial position of the center of the wavepacket $x_0 = 250$ with a standard deviation of $\sigma = 20$. **c)** 96 unit cell width, $x_0 = 48$ and $\sigma = 10$. **d)** 96 unit cells width and initial condition as excitation of one A-type node in $x_0 = 48$. The color bar represents the probability distribution as $|\psi(t,x)|^2 = |\langle xA|\psi(t)\rangle|^2 + |\langle xB|\psi(t)\rangle|^2$ and time in $\frac{1}{t}$ units with t the couplings.

We observe that for $k_0 = 0$, the packet's initial momentum, the state is accelerated to one of the edges. Since the non-Hermitian effects are sensitive to boundary conditions, we

simulate different sizes and initial conditions to demonstrate the general effect.

Now, translating this to an electrical circuit, we use as a base the SSH circuit and implement the asymmetric hoppings by an INIC configuration with an effective capacitance of C_3 based on the implementation of Helbig et al.[62], basically merging all the work shown in this thesis. A representation of the LTSpice implementation is shown in Figure 3.31

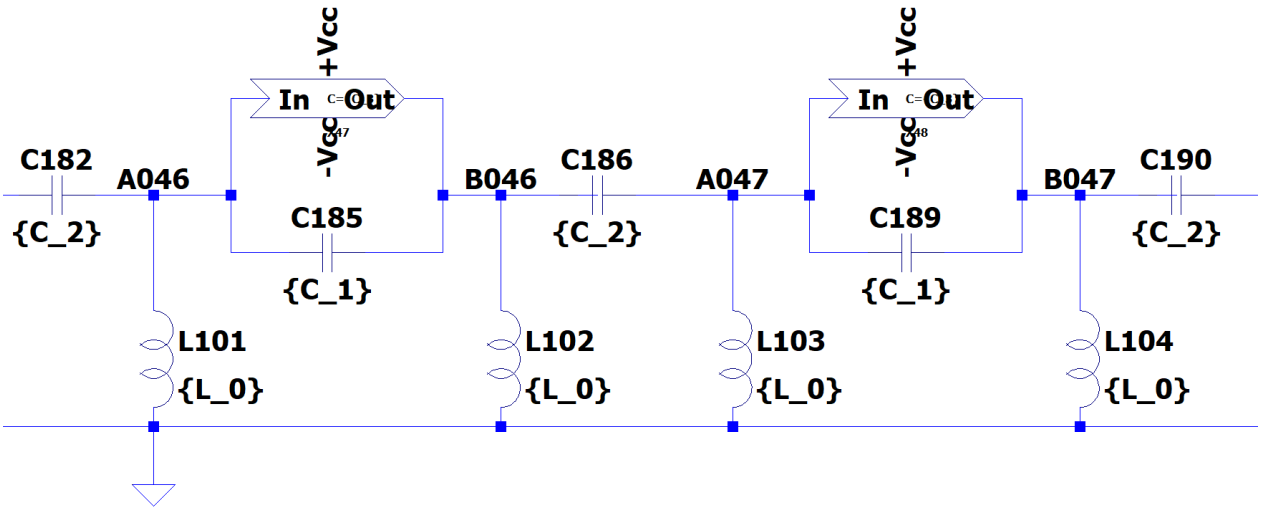

Figure 3.31: Zooming in on the bulk for the implementation of the non-Hermitian SSH model circuit, centered at cell 46. Nodes A046 and B046 exemplify the connections: Capacitors C_1 as connections of the same unit cell, capacitors C_2 as connections between cells (completing the Hermitian part of the SSH model) and INICs controlled by an absolute capacitance C_3 unbalancing the effective capacitance between nodes in the same cell as the asymmetric term. Each node is grounded with inductors L_0.

The total current at A and B is:

$$I_{Aj} = i\omega C_1(V_{Aj} - V_{Bj}) + i\omega C_2(V_{Aj} - V_{Bj-1}) + \frac{1}{i\omega L}(V_{Aj} - V_0) + i\omega C_3(V_{Aj} - V_{Bj}), \quad (3.18)$$

$$I_{Bj} = i\omega C_1(V_{Bj} - V_{Aj}) + i\omega C_2(V_{Bj} - V_{Aj+1}) + \frac{1}{i\omega L}(V_{Bj} - V_0) - i\omega C_3(V_{Bj} - V_{Aj}). \quad (3.19)$$

This yields to a set of equations for all the nodes that can be written down as:

$$\mathbf{I} = J_{SSH}\mathbf{V}. \quad (3.20)$$

Imposing periodic boundary conditions and Fourier transforming eq. 3.4 the momentum space representation of the grounded Laplacian is obtained

$$J_{NSSH}(k) = i\omega\left(C_1 + C_2 - \frac{1}{\omega^2 L}\right)\mathbb{I} - i\omega\Big[(C_1 + C_2\cos(k))\sigma_x + (C_2\sin(k) + i\omega C_3)\sigma_y + i\omega C_3\sigma_z\Big], \quad (3.21)$$

where $\{\sigma_i\}$ is the set of the Pauli matrices and $\mathbb{I}$ is the (2×2) identity matrix. As always, the identity term does not affect the eigenstates. We almost encapsulated the desired Hamiltonian but for a σ_z proportional term. We include the last term in our simulations, but its effect is negligible since C_3 is small compared to the other capacitors. Also, we can always add a

grounding capacitor $C_0 = 2C_3$ in sub-lattice A to cancel it out.

We make a circuit based on the scheme in Figure 3.31 of 96 unit cells with the following parameters: $C_1 = 6.36$uF, $C_2 = 3.183$uF, $C_3 = 0.63$uF, $L_0 = 10$u and $\omega = 2\pi f_0$ with $f_0 = 50$kHz and the same realistic Op-Amps as in section 3.3.4. With the systems constructed, we have to set up an excitation. How we excite the system affects the initial condition; a Gaussian pulse could be enough, but depending on the lifespan of the pulse it will impose an external forcing for too long. An example of this is depicted in Figure 3.32, where we see that the node of excitation functions as a voltage source point, creating an interference pattern and resonances.

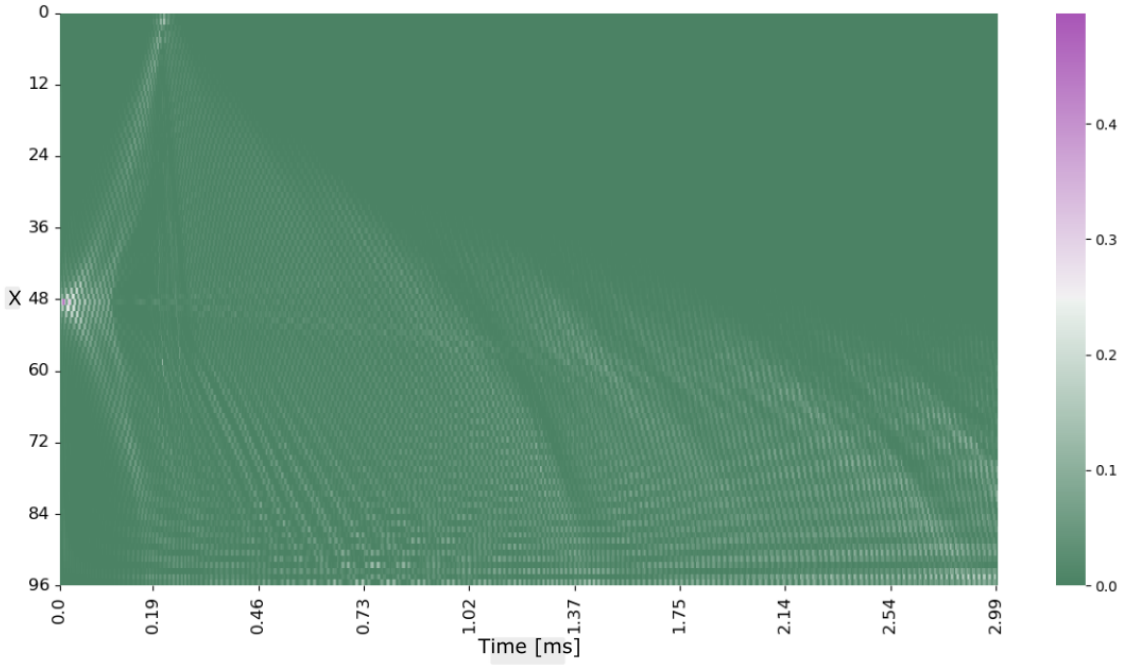

Figure 3.32: Voltage distribution over each cell for an excitation ($\tau = 1\sigma_t/2$) as a function of time t (in the x-axis), and the position of the cell x (in the y-axis). The colour bar represent $|V(t,x)|^2 = |\langle xA|\psi(t)\rangle|^2 + |\langle xB|\psi(t)\rangle|^2$.

We impose a Gaussian pulse with a narrow distribution, and we can witness the Dynamic skin effect's properties in Figure 3.33: elastic reflection to one of the boundaries and inelastic reflection to the other. The voltage is localized at one boundary, just as the probability distribution in 3.30d).

To check if the wavefront actually arrives earlier to one of the edges we visualize the voltages at the some cells living near each boundary as a function of time. Figure 3.34 shows that for the un-localized edge the voltage reaches a peak when the reflection happens. On the other hand, the voltages near the other boundary arrive earlier but not enough to ensure that the wave-packet centroid of the propagation reached it, this is due to the enhanced spreading of the wave packet in this direction. Despite of this, the voltages in this edge reach a maximum at a time marginally earlier than the peak of the other boundary, we conclude that a study of larger systems is required to probe the acceleration effect.

The voltage profile in Figure 3.35 corresponds to a shorter-lived excitation modulated with a temporal switch. The results do not improve as compared with 3.33. It misses some properties if the injections are too short. We attribute this to the presence of the ω factor in

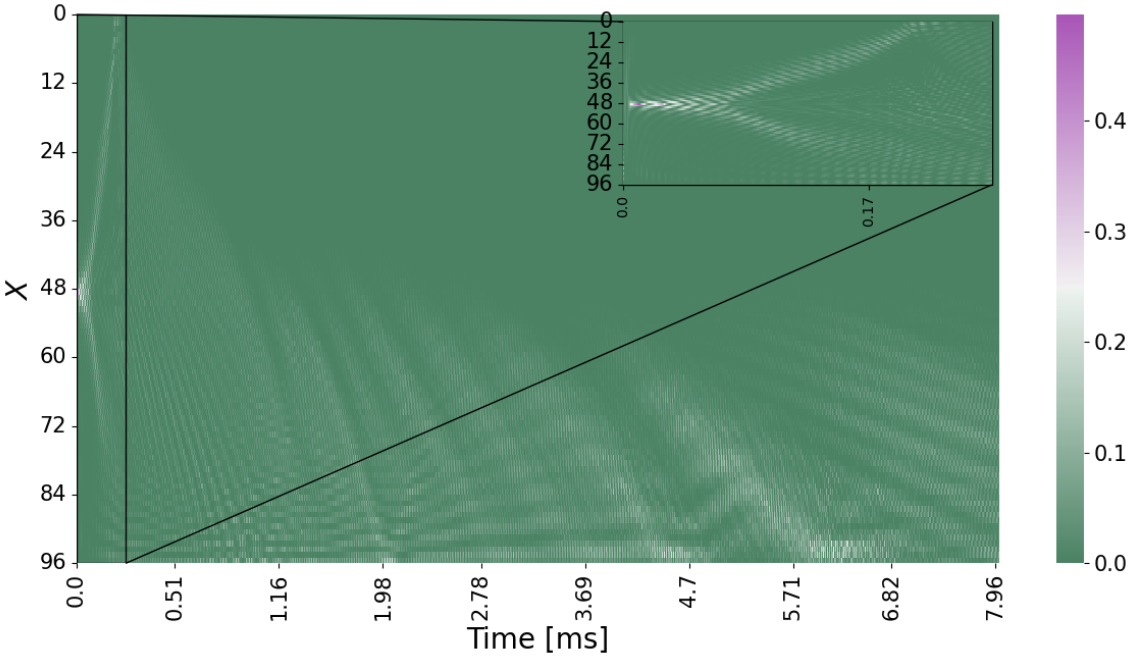

Figure 3.33: Voltage distribution over each cell for a short-lived Gaussian excitation ($\tau = 0.5\sigma_t/2$) as a function of time t (in the x-axis), and the position of the cell x (in the y-axis). The colour bar represent $|V(t,x)|^2 = |\langle xA|\psi(t)\rangle|^2 + |\langle xB|\psi(t)\rangle|^2$, normalized at each t.

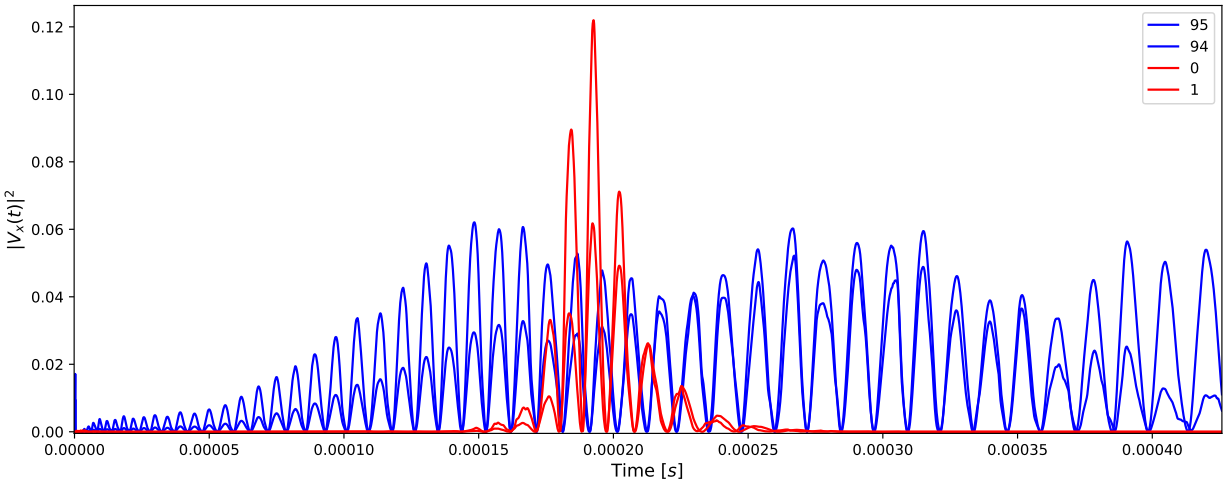

Figure 3.34: Voltages near each boundary as function of time, red is for the two first cells, at the elastic boundary (0 and 1 of our indexation), and blue is for the last two cells, at the inelastic boundary (94 and 95). The presence of narrow peaks indicates the elastic reflection and the localization arises from signals persistence over time.

the Laplacian; if the excitation is too short, it does not represent the system we are trying to replicate since it can get a complete oscillation to set up the frequency.

With this section, we again validate the simulation capabilities of electrical circuits for tight-binding Hamiltonians and extend its range to non-Hermitian phenomena.

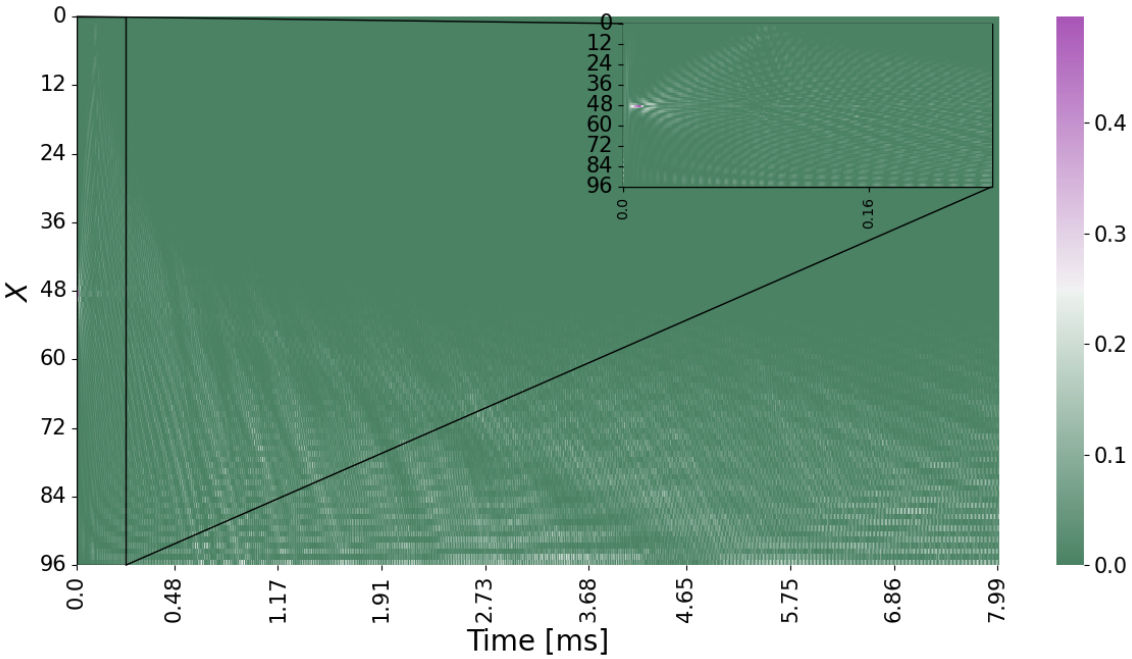

Figure 3.35: Voltage distribution over each cell for a short-lived Gaussian excitation ($\tau = 0.05\sigma_t/2$) as a function of time t (in the x-axis), and the position of the cell x (in the y-axis). The colour bar represent $|V(t,x)|^2 = |\langle xA|\psi(t)\rangle|^2 + |\langle xB|\psi(t)\rangle|^2$, normalized at each t.

Chapter 4

Conclusions

In this thesis, we investigated edge states using electrical circuits. Chapter 1 introduced the concepts and models for topological states and Tight-Binding Hamiltonians. Then, chapter 2 we discussed about topoelectrical circuits by considering the different steps involved in simulating a crystalline system. Chapter 3 focused on emulating known systems and reproducing results. We studied the SSH model, graphene, and the Haldane model to validate the circuits capabilities as simulators. This validation was achieved by obtaining the admittance band structure and studying the excitation dynamics in each model.

An additional key finding of this initial part is a new methodology for reconstructing the circuit Laplacian in real space through measurements. This allows us to compare the simulating circuit with the theoretical model. This methodology offers a valuable tool to visualize the effects of realistic components present in the circuit and provides a reliable way to check for any unintended characteristics or missed connections.

By exciting the Haldane model circuit with an external voltage source in a ribbon configuration we observed the presence of chiral states, successfully capturing the expected dynamics in its topological phase.

Having established the groundwork, Chapter 3 also addressed our other objective: proposing electrical circuits to simulate novel topological states or edge states that lack prior experimental realization. Specifically, we designed and analyzed an electrical circuit to simulate a modified Haldane model. We computed the band structure and Laplacian matrix of the circuit, achieving a high degree of agreement with the original Tight-Binding model. The antichiral states in this system were observed by measuring the voltage profile produced by injected voltages at its boundaries. This demonstrates the ability of electrical circuits to emulate not only known phenomena but also to facilitate the study of novel materials.

We further explored a less ideal scenario by considering realistic operational amplifiers (Op-Amps) and characterized their impact on the Haldane and modified Haldane models. Deviations from the ideal behavior were observed in the band structures of these models due to the replaced components. We confirmed the specific nature of these differences by comparing the measured Laplacians with the Hamiltonians. This demonstrates the potential of electrical circuits to elucidate unexpected phenomena and capturing the consequences of real-world effects in our models.

Motivated by the study of realistic scenarios, we extended our investigation to non-Hermitian phenomena using circuits. We designed and analyzed an electrical circuit to simulate a non-Hermitian SSH model with asymmetric hoppings, specifically searching for the presence of the Dynamic Skin Effect. By implementing the designed circuit and injecting

voltages, we observed the inelastic reflection of an initial state in one direction, leading to localization at that edge, and an elastic collision with the other boundary. These observations show the capabilities of electrical circuits in simulating non-Hermitian characteristics.

With this work we conclude that topoelectrical circuits are a useful tool for simulating Tight-Binding models and studying topological states or edge states. As highlighted in the introduction, these circuits also offer significant advantages by simplifying the concepts involved in studying topological phases due to the accessibility and operability of electronics, as we demonstrated with the implementations of the modified Haldane model and the non-Hermitian SSH model. Computation times could present an obstacle for studying larger systems, specially in the presence of higher voltages, but this can be overtaken with direct measurements in a real life electrical circuit in the laboratory. Further experimental realization could validate our simulations, this would help to capture the technical difficulties of this framework and provide new phenomena in a more realistic scenario.

Bibliography

[1] Luo, K., Yu, R., y Weng, H., "Topological Nodal States in Circuit Lattice", Research, vol. 2018, p. 6793752, 2018, doi:10.1155/2018/6793752.

[2] Colomés, E. y Franz, M., "Antichiral Edge States in a Modified Haldane Nanoribbon", Physical Review Letters, vol. 120, no. 8, p. 086603, 2018, doi:10.1103/PhysRevLett.120.086603.

[3] Liu, S., Shao, R., Ma, S., Zhang, L., You, O., Wu, H., Xiang, Y. J., Cui, T. J., y Zhang, S., "Non-Hermitian Skin Effect in a Non-Hermitian Electrical Circuit", Research, vol. 2021, p. 5608038, 2021, doi:10.34133/2021/5608038.

[4] Li, H. y Wan, S., "Dynamic skin effects in non-hermitian systems", Phys. Rev. B, vol. 106, p. L241112, 2022, doi:10.1103/PhysRevB.106.L241112.

[5] Zhang, F., Kane, C. L., y Mele, E. J., "Surface state magnetization and chiral edge states on topological insulators", vol. 110, no. 4, p. 046404, doi:10.1103/PhysRevLett.110.046404.

[6] Martinez Alvarez, V. M., Barrios Vargas, J. E., y Foa Torres, L. E. F., "Non-hermitian robust edge states in one dimension: Anomalous localization and eigenspace condensation at exceptional points", vol. 97, no. 12, p. 121401, doi:10.1103/PhysRevB.97.121401.

[7] Dueñas, M. y Eduardo, J., "Two studies on the interplay between topological phases, robust edge states and bosonic excitations"„ https://repositorio.uchile.cl/handle/2250/182460 (visitado el 2024-04-02).

[8] Chesta Lopez, J., Foa Torres, L. E. F., y Nunez, A. S., "Multiterminal conductance at the surface of a weyl semimetal", vol. 97, no. 12, p. 125419, doi:10.1103/PhysRevB.97.125419.

[9] Bao, J., Zou, D., Zhang, W., He, W., Sun, H., y Zhang, X., "Topoelectrical circuit octupole insulator with topologically protected corner states", vol. 100, no. 20, p. 201406, doi:10.1103/PhysRevB.100.201406.

[10] Haldane, F. D. M., "Model for a Quantum Hall Effect without Landau Levels: Condensed-Matter Realization of the Parity Anomaly", Physical Review Letters, vol. 61, no. 18, pp. 2015–2018, 1988, doi:10.1103/PhysRevLett.61.2015.

[11] Klitzing, K. v., Dorda, G., y Pepper, M., "New Method for High-Accuracy Determination of the Fine-Structure Constant Based on Quantized Hall Resistance", Physical Review Letters, vol. 45, no. 6, pp. 494–497, 1980, doi:10.1103/PhysRevLett.45.494.

[12] Jotzu, G., Messer, M., Desbuquois, R., Lebrat, M., Uehlinger, T., Greif, D., y Esslinger, T., "Experimental realization of the topological Haldane model with ultracold fermions", Nature, vol. 515, no. 7526, pp. 237–240, 2014, doi:10.1038/nature13915.

[13] Kane, C. L. y Mele, E. J., "Quantum Spin Hall Effect in Graphene", Physical Review Letters, vol. 95, no. 22, p. 226801, 2005, doi:10.1103/PhysRevLett.95.226801.

[14] König, M., Wiedmann, S., Brüne, C., Roth, A., Buhmann, H., Molenkamp, L. W., Qi, X.-L., y Zhang, S.-C., "Quantum Spin Hall Insulator State in HgTe Quantum Wells", Science, vol. 318, no. 5851, pp. 766–770, 2007, doi:10.1126/science.1148047.

[15] Atala, M., Aidelsburger, M., Barreiro, J. T., Abanin, D., Kitagawa, T., Demler, E., y Bloch, I., "Direct measurement of the Zak phase in topological Bloch bands", Nature Physics, vol. 9, no. 12, pp. 795–800, 2013, doi:10.1038/nphys2790.

[16] Fu, L., Kane, C. L., y Mele, E. J., "Topological Insulators in Three Dimensions", Physical Review Letters, vol. 98, no. 10, p. 106803, 2007, doi:10.1103/PhysRevLett.98.106803.

[17] Jia, S., Xu, S.-Y., y Hasan, M. Z., "Weyl semimetals, Fermi arcs and chiral anomalies", Nature Materials, vol. 15, no. 11, pp. 1140–1144, 2016, doi:10.1038/nmat4787.

[18] Lindner, N. H., Refael, G., y Galitski, V., "Floquet topological insulator in semiconductor quantum wells", Nature Physics, vol. 7, no. 6, pp. 490–495, 2011, doi:10.1038/nphys1926.

[19] Brandenbourger, M., Locsin, X., Lerner, E., y Coulais, C., "Non-reciprocal robotic metamaterials", Nature Communications, vol. 10, no. 1, p. 4608, 2019, doi:10.1038/s41467-019-12599-3.

[20] Xiao, L., Deng, T., Wang, K., Zhu, G., Wang, Z., Yi, W., y Xue, P., "Non-Hermitian bulk–boundary correspondence in quantum dynamics", Nature Physics, vol. 16, no. 7, pp. 761–766, 2020, doi:10.1038/s41567-020-0836-6.

[21] Caceres-Aravena, G., Torres, L. F., y Vicencio, R. A., "Topological and flat-band states induced by hybridized linear interactions in one-dimensional photonic lattices", Physical Review A, vol. 102, no. 2, p. 023505, 2020.

[22] Cáceres-Aravena, G., Real, B., Guzmán-Silva, D., Vildoso, P., Salinas, I., Amo, A., Ozawa, T., y Vicencio, R. A., "Edge-to-edge topological spectral transfer in diamond photonic lattices", APL Photonics, vol. 8, no. 8, 2023.

[23] Cage, M. E., Dziuba, R. F., y Field, B. F., "A test of the quantum hall effect as a resistance standard", IEEE Transactions on Instrumentation and Measurement, vol. IM-34, no. 2, pp. 301–303, 1985, doi:10.1109/TIM.1985.4315329.

[24] Von Klitzing, K., "Developments in the quantum hall effect", Philosophical Transactions of the Royal Society A: Mathematical, Physical and Engineering Sciences, vol. 363, no. 1834, pp. 2203–2219, 2005.

[25] Von Klitzing, K., "25 years of quantum hall effect (qhe) a personal view on the discovery, physics and applications of this quantum effect", en The Quantum Hall Effect: Poincaré Seminar 2004, pp. 1–21, Springer, 2005.

[26] Laughlin, R. B., "Quantized hall conductivity in two dimensions", Phys. Rev. B, vol. 23, pp. 5632–5633, 1981, doi:10.1103/PhysRevB.23.5632.

[27] Halperin, B. I., "Quantized hall conductance, current-carrying edge states, and the existence of extended states in a two-dimensional disordered potential", Physical review B, vol. 25, no. 4, p. 2185, 1982.

[28] Thouless, D. J., Kohmoto, M., Nightingale, M. P., y den Nijs, M., "Quantized Hall Conductance in a Two-Dimensional Periodic Potential", Physical Review Letters, vol. 49,

no. 6, pp. 405–408, 1982, doi:10.1103/PhysRevLett.49.405.

[29] Su, W. P., Schrieffer, J. R., y Heeger, A. J., "Solitons in Polyacetylene", Physical Review Letters, vol. 42, no. 25, pp. 1698–1701, 1979, doi:10.1103/PhysRevLett.42.1698.

[30] Guo, H.-M., "A brief review on one-dimensional topological insulators and superconductors", vol. 59, no. 3, p. 637401, doi:10.1007/s11433-015-5773-5.

[31] Zhu, B., "Lecture notes on Topological Insulators". https://phyx.readthedocs.io/en/latest/TI/Lecture%20notes/main.html. Accessed: 2024 February 15.

[32] Asbóth, J. K., Oroszlány, L., y Pályi, A., A Short Course on Topological Insulators. Springer International Publishing, 2016, doi:10.1007/978-3-319-25607-8.

[33] Lee, C., Wei, X., Kysar, J. W., y Hone, J., "Measurement of the elastic properties and intrinsic strength of monolayer graphene", vol. 321, no. 5887, pp. 385–388, doi:10.1126/science.1157996.

[34] Faugeras, C., Faugeras, B., Orlita, M., Potemski, M., Nair, R. R., y Geim, A. K., "Thermal conductivity of graphene in corbino membrane geometry", vol. 4, no. 4, pp. 1889–1892, doi:10.1021/nn9016229.

[35] Schwamb, T., Burg, B. R., Schirmer, N. C., y Poulikakos, D., "An electrical method for the measurement of the thermal and electrical conductivity of reduced graphene oxide nanostructures", vol. 20, no. 40, p. 405704, doi:10.1088/0957-4484/20/40/405704.

[36] Novoselov, K. S., Geim, A. K., Morozov, S. V., Jiang, D., Zhang, Y., Dubonos, S. V., Grigorieva, I. V., y Firsov, A. A., "Electric field effect in atomically thin carbon films", vol. 306, no. 5696, pp. 666–669, doi:10.1126/science.1102896.

[37] Novoselov, K. S., Geim, A. K., Morozov, S. V., Jiang, D., Katsnelson, M. I., Grigorieva, I. V., Dubonos, S. V., y Firsov, A. A., "Two-dimensional gas of massless dirac fermions in graphene", Nature, vol. 438, no. 7065, 2005, doi:10.1038/nature04233.

[38] Dresselhaus, M., Dresselhaus, G., Saito, R., y Jorio, A., "Raman spectroscopy of carbon nanotubes", Physics Reports, vol. 409, no. 2, pp. 47–99, 2005, doi:https://doi.org/10.1016/j.physrep.2004.10.006.

[39] Foa Torres, L. E. F., Roche, S., y Charlier, J. C., Introduction to Graphene-Based Nanomaterials: From Electronic Structure to Quantum Transport (second edition). Cambridge University Press, 2020, https://www.cambridge.org/us/academic/subjects/physics/condensed-matter-physics-nanoscience-and-mesoscopic-physics/introduction-graphene-based-nanomaterials-electronic-structure-quantum-transport-2nd-edition?format=HB\&isbn=9781108476997 (visitado el 2020-06-25).

[40] Rodriguez Mena, E., Nuevas manifestaciones de estados topológicos de la materia. PhD thesis, Universidad de Chile - Facultad de Ciencias Físicas y Matemáticas, 2021.

[41] Simon, S. H., The Oxford solid state basics. OUP Oxford, 2013.

[42] Denner, M. M., Lado, J. L., y Zilberberg, O., "Antichiral states in twisted graphene multilayers", Physical Review Research, vol. 2, no. 4, p. 043190, 2020, doi:10.1103/PhysRevResearch.2.043190.

[43] Medina Dueñas, J., Calvo, H. L., y Foa Torres, L. E., "Copropagating Edge States Produced by the Interaction between Electrons and Chiral Phonons in Two-Dimensional Materials", Physical Review Letters, vol. 128, no. 6, p. 066801, 2022, doi:10.1103/Phys

RevLett.128.066801.

[44] Mella, J. D., Calvo, H. L., y Foa Torres, L. E. F., "Entangled States Induced by Electron–Phonon Interaction in Two-Dimensional Materials", Nano Letters, vol. 23, no. 23, pp. 11013–11018, 2023, doi:10.1021/acs.nanolett.3c03316.

[45] Yamamoto, K., Nakagawa, M., Adachi, K., Takasan, K., Ueda, M., y Kawakami, N., "Theory of non-hermitian fermionic superfluidity with a complex-valued interaction", vol. 123, no. 12, p. 123601, doi:10.1103/PhysRevLett.123.123601.

[46] Kozii, V. y Fu, L., "Non-hermitian topological theory of finite-lifetime quasiparticles: Prediction of bulk fermi arc due to exceptional point"., doi:10.48550/arXiv.1708.05841.

[47] Zyuzin, A. A. y Zyuzin, A. Y., "Flat band in disorder-driven non-hermitian weyl semimetals", vol. 97, no. 4, p. 041203, doi:10.1103/PhysRevB.97.041203.

[48] Rüter, C. E., Makris, K. G., El-Ganainy, R., Christodoulides, D. N., Segev, M., y Kip, D., "Observation of parity–time symmetry in optics", vol. 6, no. 3, pp. 192–195, doi:10.1038/nphys1515.

[49] Ozawa, T., Price, H. M., Amo, A., Goldman, N., Hafezi, M., Lu, L., Rechtsman, M. C., Schuster, D., Simon, J., Zilberberg, O., y Carusotto, I., "Topological photonics", vol. 91, no. 1, p. 015006, doi:10.1103/RevModPhys.91.015006.

[50] Esaki, K., Sato, M., Hasebe, K., y Kohmoto, M., "Edge states and topological phases in non-hermitian systems", vol. 84, no. 20, p. 205128, doi:10.1103/PhysRevB.84.205128.

[51] Gong, Z., Ashida, Y., Kawabata, K., Takasan, K., Higashikawa, S., y Ueda, M., "Topological phases of non-hermitian systems", vol. 8, no. 3, p. 031079, doi:10.1103/PhysRevX.8.031079.

[52] Foa Torres, L. E. F., "Perspective on topological states of non-hermitian lattices", vol. 3, no. 1, p. 014002, doi:10.1088/2515-7639/ab4092.

[53] Yao, S. y Wang, Z., "Edge states and topological invariants of non-hermitian systems", vol. 121, no. 8, p. 086803, doi:10.1103/PhysRevLett.121.086803.

[54] Imhof, S., Berger, C., Bayer, F., Brehm, J., Molenkamp, L. W., Kiessling, T., Schindler, F., Lee, C. H., Greiter, M., Neupert, T., y Thomale, R., "Topolectrical-circuit realization of topological corner modes", Nature Physics, vol. 14, no. 9, pp. 925–929, 2018, doi:10.1038/s41567-018-0246-1.

[55] Olekhno, N. A., Kretov, E. I., Stepanenko, A. A., Ivanova, P. A., Yaroshenko, V. V., Puhtina, E. M., Filonov, D. S., Cappello, B., Matekovits, L., y Gorlach, M. A., "Topological edge states of interacting photon pairs emulated in a topolectrical circuit", Nature communications, vol. 11, no. 1, p. 1436, 2020.

[56] Hofmann, T., Helbig, T., Lee, C. H., Greiter, M., y Thomale, R., "Chiral Voltage Propagation and Calibration in a Topolectrical Chern Circuit", Physical Review Letters, vol. 122, no. 24, p. 247702, 2019, doi:10.1103/PhysRevLett.122.247702.

[57] Lee, C. H., Imhof, S., Berger, C., Bayer, F., Brehm, J., Molenkamp, L. W., Kiessling, T., y Thomale, R., "Topolectrical Circuits", Communications Physics, vol. 1, no. 1, p. 39, 2018, doi:10.1038/s42005-018-0035-2.

[58] Helbig, T., Hofmann, T., Lee, C. H., Thomale, R., Imhof, S., Molenkamp, L. W., y Kiessling, T., "Band structure engineering and reconstruction in electric circuit networks",

Physical Review B, vol. 99, no. 16, p. 161114, 2019, doi:10.1103/PhysRevB.99.161114.

[59] Dong, J., Juričić, V., y Roy, B., "Topolectric circuits: Theory and construction", Physical Review Research, vol. 3, no. 2, p. 023056, 2021, doi:10.1103/PhysRevResearch.3.023056.

[60] Ezawa, M., "Electric circuits for non-Hermitian Chern insulators", Physical Review B, vol. 100, no. 8, p. 081401, 2019, doi:10.1103/PhysRevB.100.081401.

[61] Zhang, X.-X. y Franz, M., "Non-Hermitian Exceptional Landau Quantization in Electric Circuits", Physical Review Letters, vol. 124, no. 4, p. 046401, 2020, doi:10.1103/PhysRevLett.124.046401.

[62] Helbig, T., Hofmann, T., Imhof, S., Abdelghany, M., Kiessling, T., Molenkamp, L. W., Lee, C. H., Szameit, A., Greiter, M., y Thomale, R., "Generalized bulk–boundary correspondence in non-Hermitian topolectrical circuits", Nature Physics, vol. 16, no. 7, pp. 747–750, 2020, doi:10.1038/s41567-020-0922-9.

[63] Lu, L., "Topology on a breadboard", Nature Physics, vol. 14, no. 9, pp. 875–877, 2018, doi:10.1038/s41567-018-0235-4.

[64] Jung, W., "SECTION 1-1 - Introduction", en Op Amp Applications Handbook (Jung, W., ed.), pp. 5–21, Burlington: Newnes, 2005, doi:https://doi.org/10.1016/B978-0750678447-5/50114-4.

[65] Čerňanová, V., Brenkuŝ, J., y Stopjakova, V., "Non–symmetric finite networks: The two–point resistance", Journal of Electrical Engineering, vol. 65, no. 5, pp. 283–288, 2014.

[66] Cserti, J., Széchenyi, G., y Dávid, G., "Uniform tiling with electrical resistors", Journal of Physics A: Mathematical and Theoretical, vol. 44, no. 21, p. 215201, 2011.

[67] Semenoff, G. W., "Condensed-matter simulation of a three-dimensional anomaly", Phys. Rev. Lett., vol. 53, pp. 2449–2452, 1984, doi:10.1103/PhysRevLett.53.2449.